THE UNIVERSITY *of* EDINBURGH

Mechanisms for Wintertime Fjord-Shelf Heat Exchange in Greenland and Svalbard

Neil J. Fraser

Department of Geosciences

The University of Edinburgh

Thesis Submitted for the Degree of Doctor of Philosophy

October 2017

Abstract

No region has felt the effects of global climate change more acutely than the cryosphere, which has changed at an unprecedented rate in the past two decades. The scientific consensus is that these changes are driven largely by increasing ocean heat content at high latitudes. In southeast Greenland, acceleration and retreat of the marine-terminating glaciers contributes significantly towards global sea level rise. Circulation in the fjords which accommodate these glaciers is thought to be driven both by freshwater input and by barrier wind-driven shelf exchange. Due to a scarcity of data, particularly from winter, the balance between these two mechanisms is not fully understood. In Svalbard, increasing water temperature has decimated sea ice cover in many of the fjords, and had substantial implications for the local ecosystem. While there is a relatively comprehensive literature on shelf exchange mechanisms in Svalbard fjords, questions remain over how the internal circulation interacts with exchange mechanisms. The region shares a similar underwater topography and oceanographic setting with southeast Greenland, with marine-terminating glaciers in close proximity to warm Atlantic waters, and results from Svalbard can hence be used to inform studies of high-latitude fjord-shelf exchange in a broader context.

A realistic numerical model was constructed with the aim of better understanding the interaction between Kangerdlugssuaq Fjord and the adjacent continental shelf, and quantifying heat exchange during winter. The model was initially run in an idealised configuration with winter climatological forcing fields, incorporating a parameterisation for melting at the terminus, and used to test the impact of barrier wind events. The Earth's rotation played a crucial role in the nature of the circulation and exchange in the fjord, with inflow on the right (looking up-fjord) and outflow on the left. While the heat delivered into the fjord-mouth was smaller than that observed in summer, the background internal circulation was found to efficiently distribute waters through the fjord without external forcing, and the heat delivered to the glacier terminus was comparable to summer values. Barrier winds were found to excite coastally-trapped internal waves which propagated into the fjord along the right-hand side. The process was capable of doubling the heat delivery. The process also enhanced the background circulation, likely via Stokes' Drift. The model was then adapted to simulate winter 2007-08 under historical forcing conditions. Time series

of glacial melt rate, as well as the heat flux through fjord cross-sections, were constructed and compared to the variability in wind forcing. Long periods of moderate wind stress were found to induce greatly enhanced heat flux towards the ice sheet, while short, strong gusts were found to have little influence, suggesting that the timescale over which the shelf wind field varies is a key parameter in dictating wintertime heat delivery from the ocean to the Greenland Ice Sheet.

An underwater glider was deployed to Isfjorden, a large fjord system in Svalbard, to measure the temperature, salinity and depth-averaged currents over the course of November 2014. Like in Kangerdlugssuaq, the circulation in Isfjorden was found to be heavily influenced by the Earth's rotation and by wind activity both locally and on the shelf. The combination of hydrography and high-resolution velocity data provided new insights, suggesting that the approach will be useful for studying high-latitude fjords in the future.

Lay Summary

The Greenland ice sheet is melting and contributing to sea level rise. This is thought to be caused by increasing ocean temperature. Near the edge of the ice sheet, the ice forms glaciers which typically flow into coastal inlets, or fjords. These are the only regions in which seawater is in direct contact with the ice sheet, and it is therefore necessary to understand what makes water flows in and out of these fjords in order to measure how much heat energy is transferred from the water to the ice. Icebergs, sea ice and bad weather make it difficult to take measurements of the water in these regions using research ships, particularly in winter. The focus of this thesis is to study the motion of water in fjords using alternative means.

One approach was to use computer simulations of the water both inside and directly outside a large fjord in southeast Greenland, to examine how the two regions interact and how much heat energy is delivered into the fjord. The first simulations were designed to mimic the average conditions during winter while testing the effect of changing the wind patterns outside the fjord, which has previously been identified as a trigger for warm water to flow into the fjord. A later simulation was designed to recreate the winter of 2007-08. It was found that water flowing into the fjord was generally confined to the right-hand side, looking into the fjord, and water flowing out on the left. This type of flow pattern is special because it is caused by the rotation of the Earth, which can only play a significant role when the fjord is sufficiently broad. Strong winds outside the fjord were found to drive warm water into the fjord, but whether or not this water stayed inside the fjord so as to affect the glacier was dependent on the duration of these winds.

A second approach was the use of underwater flying robots, which were trialled in a broad fjord in Svalbard. These instruments provided current measurements as well as standard temperature and salinity data. The Earth's rotation was again an important factor, and the flow patterns were similar to those found in Greenland. Also, the wind patterns both inside and outside the fjord were found to control the transport of water in and out of the fjord.

Declaration

I declare that this thesis has been composed solely by myself and that it has not been submitted, either in whole or in part, in any previous application for a degree. Except where otherwise acknowledged, the work presented is entirely my own.

Neil Fraser

2017

Acknowledgments

Firstly, I would like to thank my director of studies Mark Inall for his continued guidance and infectious enthusiasm in relation to the project. I always left those meetings full of ideas and eager to make progress. I also wish to thank my other supervisors, Finlo Cottier, Peter Nienow and Noel Gourmelen, for their advice and support.

The research was funded by a NERC studentship, project no. N0406, without which would I have been unable to conduct the research or write this thesis.

I am indebted to the many people who contributed data and/or technical support towards the project: Marcello Magaldi, Inga Koszalka and Tom Haine for getting me started with MITgcm and providing with model boundary fields; Julian Dowdeswell for the bathymetry data from the Kangerdlugssuaq Fjord interior; Tom Cowton for helping me implement subsurface freshwater input at the glacier terminus; Ben Harden for providing me with his composite wind fields; Erik Bruvik, Estelle Dumont and Karen Wilson for providing glider support; and Frank Nilsen, Ragnheid Skogseth, Elisa Lindgren and Torbjørn Taskjelle for their invaluable contributions towards the glider study in Svalbard.

Lastly, I would like to thank all my family and friends who, perhaps unknowingly, played a part in getting me though. In particular I would like to thank my partner Rosie for tolerating me throughout the occasionally turbulent postgraduate experience, all while simultaneously forging her own career as a nurse.

Contents

Chapter 1

Introduction

1.1 Motivation

Changes to the mass balance of the Greenland Ice Sheet (GrIS) over the past two decades have been most profound near the coastline (Rignot and Kanagaratnam, 2006; Shepherd et al., 2012; Morlighem et al., 2017), have contributed significantly to sea level rise (Nick et al., 2009; Khan et al., 2014), and have affected ocean salinity (Bamber et al., 2012). The major outlet glaciers of southeast (SE) Greenland have undergone rapid acceleration and retreat (Andresen et al., 2011; Bevan et al., 2012; Enderlin et al., 2014), coinciding with increasing ocean temperatures in the North Atlantic (Straneo and Heimbach, 2013; Holland et al., 2008), suggesting oceanic warming is a possible trigger (Hanna et al., 2009). Furthermore the most profound melting has been localised to regions supplied with warm water of subtropical origin (Seale et al., 2011). However, the mechanisms which transport warm water from the open ocean to fjord interior, and into direct contact with glaciers, are not fully understood. In summer, freshwater runoff from the GrIS drives an estuarine overturning circulation which draws in water at depth (Cowton et al., 2015; Carroll et al., 2016). Increasing evidence indicates that wind activity on the continental shelf region during winter also plays a crucial role in delivering warm water into these fjords by inducing a strong, externally forced circulation pattern (Straneo et al., 2010; Jackson et al., 2014; Sutherland et al., 2014b). Due to seasonal sea ice cover, as well as the remote, hazardous nature of the region, observations from within SE Greenland's fjords during winter are scarce, making it difficult to quantify the heat delivery during those months (Sutherland et al., 2014b).

A decrease in seasonal sea ice formation in Svalbard has coincided with these changes to the GrIS, and has also been linked to increased oceanic heating (Pavlov et al., 2013; Onarheim et al., 2014b; Muckenhuber et al., 2016). These changes extend to the interior

of west Spitsbergen's fjords, indicating that warm subtropical waters enter these regions. While there is considerable literature on cross-shelf and fjord-shelf exchange in this region (Cottier et al., 2005, 2007; Nilsen et al., 2008, 2016; Inall et al., 2015), further research is required to fully understand changes to hydrography and circulation within these fjords (Sundfjord et al., 2017) and, hence, quantify the oceanic contribution to decreasing sea ice cover.

1.2 Objectives

The key objectives of this thesis are:

- *Quantify the potential for fjord-shelf heat exchange in winter.*
- *Assess the impact of the Earth's rotation on exchange in broad fjords.*
- *Investigate new means of observation in major fjord systems.*

1.3 Thesis Structure

This thesis is divided into six chapters. Chapter 2 gives the context and motivation for the research by introducing the high-latitude fjord setting and identifying the gaps in our current understanding of these regions. Chapters 3 and 4 present the two numerical modelling studies of a major Greenlandic fjord which constitute the main focus of the thesis, and Chapter 5 is concerned with a glider-based observational study in a large Svalbard fjord. Chapters 3 and 5 correspond closely to journal publications while Chapter 4 is still being developed as is in the final stages of preparation for journal submission. Finally there is a joint discussion chapter, where the implications from each study are summarised and drawn together.

Chapter 2

Background

2.1 Introduction to High-Latitude Fjords

A fjord is typically a deep, steep sided, narrow coastal inlet, with a restricted connection to the continental shelf due to a sill at the mouth, and also a significant freshwater input due to a large catchment of local precipitation (Inall and Gillibrand, 2010). Fjords are glacially carved topographical features and thus exclusive to regions of mid-to-high latitudes (Cottier et al., 2010). In mid-latitudes the freshwater input takes the form of riverine inflow, however here we are concerned solely with the glaciated fjords of higher latitudes.

High-latitude fjords display a seasonal cycle in stratification due to the varying temperature and salinity, and, hence, density, of the water masses present at the fjord mouth as well as controls such as terrestrial freshwater input and surface solar radiation in summer as well as sea ice formation in winter (Mortensen et al., 2013). Stratification is at a maximum in summer, typically showing three distinct layers: fresh surface water overlaying warmer, saltier intermediate water, with cold, saline water – known as deep or isolated water - found in the bottom layer, below the sill depth. In autumn the surface water is cooled through heat loss into the atmosphere, therefore becoming denser and mixing with the intermediate water below. Further downward mixing occurs in winter as sea ice is formed, which gives rise to brine release and cooling at the surface, both of which generate dense waters which mix downward through the water column, and can culminate in the complete breakdown of stratification in shallower fjords. At low temperatures ($-2°\mathrm{C} < \Theta < 4°\mathrm{C}$), salinity has a controlling influence on density, meaning the release of brine is a principal driver of convection. In spring the surface layer is warmed due to solar and atmospheric warming, and freshened due to melt water runoff, resulting once again in a stratified water column. For a more in-depth explanation of the seasonal cycle see Cottier et al. (2010).

The influx of freshwater at the head of a fjord and the presence of ocean/shelf waters at the

mouth generates along-fjord salinity and temperature gradients. This can lead to pressure gradients which generate along-fjord circulation patterns. The classic picture is that of a process called estuarine circulation (Inall and Gillibrand, 2010), whereby runoff entrains ambient waters into the surface outflow, driving a compensatory inflow in the intermediate layer above the sill depth. Near the ice/water interface, convective overturning and melting gives rise to a region of vigorous mixing and large vertical velocities, such that stratification can break down completely. Warm waters are cooled and freshened through mixing with glacier melt water, supplying heat to the glacier front in the process so as to enhance further melting (Sciascia et al., 2013; Cowton et al., 2015).

The dense water lying below the sill depth is largely cut off from the adjacent shelf water, and is hence known as deep or isolated water (Nilsen et al., 2008; Inall and Gillibrand, 2010). Isolated water is generally not involved with fjordic circulation, and is left to stagnate. Isolated water can, however, be displaced during an event called deep water renewal. This can occur when denser water is advected over the sill and comes to flood the fjord bottom, replacing the isolated water (Inall and Gillibrand, 2010), or, in shallower fjords, due to seasonal brine-driven convection (Nilsen et al., 2008). These deep water renewal events are sporadic and difficult to predict, and have not been shown to play a major role in the mean circulation or heat delivery (Arneborg et al., 2004).

2.1.1 Drivers of Fjord Circulation

The circulation within high-latitude fjords is influenced by a number of external factors, namely wind stress, freshwater input, iceberg calving, sea ice formation/melting, tides, the Earth's rotation and shelf exchange. Each of these mechanisms is briefly described here.

2.1.1.1 Wind

Wind forcing plays a vital role in fjordic circulation, providing a surface stress that can dominate the dynamics of the upper layers. The typically steep, high sides of a fjord have the effect of steering the wind in an along-fjord direction (Nilsen et al., 2008). Wind stress increases mixing between freshwater input and the surface layer, leading to greater entrainment which in turn leads to a stronger estuarine circulation. A down-fjord (up-fjord) wind has the added effect of enhancing (retarding) estuarine circulation through acceleration (deceleration) of the flow of the upper-layer outflow. A strong up-fjord wind can stop or even reverse estuarine circulation in this way (Inall and Gillibrand, 2010). When the wind is oriented up-fjord a surface level gradient is formed as water is piled toward the head of the fjord. For down-fjord wind the converse is true, although to a lesser extent due to the sill and typically narrow fjord mouth creating only a partial barrier

(Inall and Gillibrand, 2010). Once the wind relaxes, gravity acts to reduce the surface gradient resulting in along-fjord, barotropic flow. In instances where wave period, T, satisfies $T = {}^{4L}/_{c}$ where L is the fjord length and c is the propagation speed, barotropic waves resonate at the fundamental frequency of oscillation giving rise to a standing wave known as a barotropic seiche (Parsmar and Stigebrandt, 1997). The piling of mass in the surface layer at one end of the fjord causes a depression in the pycnocline below, which can generate internal, or baroclinic, waves. (Inall and Gillibrand, 2010). Internal waves propagate much more slowly than their barotropic counterparts due to the density change across the pycnocline being much less than that across the water surface, leading to a lesser restoring force. Baroclinic seiching motions can occur when $T = {}^{4L}/_{c'}$, where c' is the internal wave propagation speed.

2.1.1.2 Freshwater

The supply of freshwater into a fjord is the basis for estuarine circulation, both in mid and high latitudes. In high-latitude fjords, freshwater is mostly input at glacier termini, via three distinct mechanisms (Straneo et al., 2011). Solar radiation and atmospheric warming cause melting on the ice surface. This gives rise to freshwater rivers running into the fjord at the surface, known as surface runoff. Due to crevassing caused by shears in glacier flow, fresh surface melt may also run down channels—known as moulins—to the glacier base, to then be introduced into the fjord at depth (Das et al., 2008). This is termed subglacial discharge, and gives rise to a plume of fresh, buoyant water at the ice/water interface, enhancing vertical mixing in this zone and contributing to the breakdown in stratification associated with estuarine circulation (Jenkins, 2011; Salcedo-Castro et al., 2011). Due to a dependence on solar radiation, both runoff and subglacial discharge are strongly seasonal phenomena. The third mechanism is for fjord water to melt the submerged portion of the glacier terminus directly, which also gives rise to freshwater at depth.

2.1.1.3 Icebergs

Calving at glacier termini results in the presence of icebergs within high-latitude fjords. Calving events cause severe disturbance to the adjacent fjord water (Burton et al., 2012), however direct observation of water properties near the calving front is challenging. It has been suggested that large calving events could provide sufficient energy to mix the entire water column (Sutherland and Straneo, 2012). In addition, the presence of icebergs throughout the fjord presents a spatially distributed source of freshwater, with further subsurface melting and subsequent vertical mixing away from the calving terminus (Azetsu-Scott and Tan, 1997).

2.1.1.4 Sea Ice

A seasonal covering of sea ice is a typical feature of high-latitude fjords. The formation of sea ice causes brine release into the surface layer, increasing its density and therefore encouraging convection and vertical mixing with the lower layers (Cottier et al., 2010). Melting sea ice freshens the surface waters, increasing stratification. A consequence of fast ice is the elimination of wind stress, rendering behaviour such as wind induced seiching and wind contribution to estuarine circulation largely seasonal. It has been shown that the formation of sea ice mélange can halt the calving of icebergs (Seale et al., 2011), retarding terminus retreat in winter months. Furthermore, sea ice in a fjord can have a buttressing effect on the glacier due to sidewall friction, contributing to seasonal variation in glacial flow speed (Joughin et al., 2008; Nick et al., 2009).

2.1.1.5 Tides

The effect of tides on fjords is that of a periodic oscillation of sea surface level at the fjord mouth. This gives rise to a temporal variation in cross sectional area of the mouth and hence in the potential exchange between fjord and shelf waters (Inall and Gillibrand, 2010). The difference in sea surface height between the fjord and the adjacent shelf results in a regular barotropic pressure gradient at the fjord mouth. In shallow regions with strong tides, tidal flows are high speed and will dominate velocity profiles near the fjord mouth. This exchange is of relatively high frequency $\left(2\,\mathrm{days}^{-1}\right)$, and so only when velocities are averaged over many tidal periods do baroclinic circulation patterns, such as estuarine circulation, become more readily apparent. In a stratified fjord, the oscillatory exchange at the sill excites internal waves of tidal frequency: a phenomenon known as an internal tide (e.g. Allen and Simpson, 2002). Internal tides encourage mixing between the layers within the fjord.

2.1.1.6 The Earth's Rotation

The effect of the Earth's rotation plays a significant role in the dynamics of larger fjords (e.g. Janzen et al., 2005; Johnson et al., 2011). The Coriolis effect exerts an apparent force on all objects with non-zero velocity relative to the Earth's surface. This force results in all flows in the Northern (Southern) Hemisphere being deflected to the right (left) with the magnitude proportional to velocity and increasing sinusoidally with latitude. On small scales, the Coriolis force has a negligible effect on dynamics when compared to the other physical drivers discussed above. However, on larger scales this effect plays a significant role in hydrodynamics. The internal Rossby radius of deformation, the length scale at which rotational effects become significant, is defined

$$L_R = \frac{c'}{f} \tag{2.1}$$

where $f = 2\Omega \sin \phi$ is the Coriolis parameter. Here ϕ denotes latitude and $\Omega = 7.2921 \times 10^{-5} \mathrm{rad\,s^{-1}}$ is the Earth's angular frequency. There is an implicit dependence on stratification, as c' increases with the strength of the pycnocline. Fjords broader than L_R are termed "broad" fjords: at these lengthscales, flows which initially move antiparallel to pressure gradients are deflected by the Coriolis force until the force from the pressure gradient and the Coriolis force are balanced. Once this balance occurs the flow is stable and is said to be geostrophic. Geostrophic flows travel tangent to isobars. Across-fjord pressure gradients hence generate along-fjord currents in broad fjords, and cross-fjord velocity variability is allowed. The typical behaviour in broad fjords at high northern latitudes is for inflow (outflow) to take place on the right-hand (left-hand) side of the mouth, looking into the fjord. This is not a dominant behaviour in narrower fjords, where the lack of cross fjord variability renders the system essentially two-dimensional. The Coriolis force alters the effect of the wind, deflecting surface velocities to the right (or left in the Southern Hemisphere) of wind stress vectors in a phenomenon called Ekman transport. Along-fjord winds in broad fjords can therefore generate across-fjord velocities together with upwelling and downwelling at the fjord side walls.

2.1.1.7 Shelf Exchange

A fjord will typically open not into the deep ocean but onto a broad, relatively shallow continental shelf. In deep-silled fjords, changes in the water column outside the fjord will generate baroclinic pressure gradients between fjord and shelf which drive exchange flows. These changes may be driven by along-shelf winds which, due to Ekman transport, cause either upwelling or downwelling at the coastal boundary. Along-shelf, geostrophic currents have been found to restrict fjord-shelf exchange, via a mechanism called geostrophic control (Klinck et al., 1981). As these currents cross the fjord entrance, the sloping isopycnals, characteristic of geostrophic flow, result in density gradients at the fjord mouth which restrict exchange and can isolate fjord from shelf.

2.2 Southeast Greenland

2.2.1 Topography

The southeast coast of Greenland, here defined to be the section between Scoresby Sund and Cape Farewell, is permeated with numerous fjord systems which generally accommodate one or more of the GrIS outlet glaciers. A broad (100-200 km) continental shelf borders

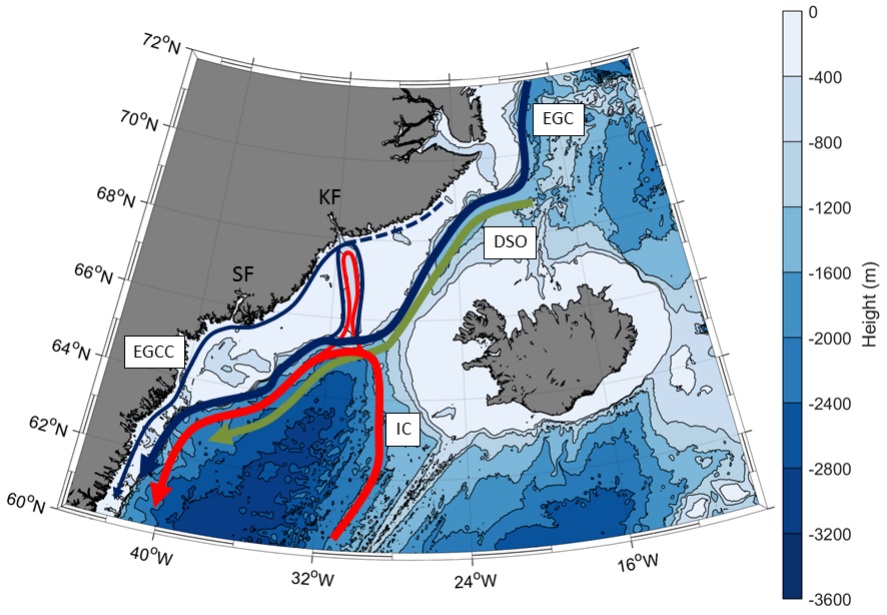

Figure 2.1: Bathymetry and circulation in SE Greenland. The EGC and EGCC are shown in blue, the IC in red and the DSO in green. The locations of KF and SF are shown.

the coastline, narrowing significantly towards the southern tip. Shelf waters are generally around 200-300 m deep, however the shelf is deeper in places due to cross-shelf canyons, glacially carved during previous ice ages. In the central and southwestern regions, the seabed descends steeply at the shelf edge where it meets the ∼3000 m deep Irminger Basin. The northeastern end of the shelf borders the southwestern region of the Greenland Sea, which is around 1200 m in depth. Between these two deep regions the shelf edge nears the shelf surrounding Iceland, and there exists a 600 m deep saddle point which acts as a partial barrier to flow through the Denmark Strait.

2.2.2 Kangerdlugssuaq Fjord

The most prominent tidewater glacier in SE Greenland is Kangerdlugssuaq Glacier (KG) (Enderlin et al., 2014) which, together with its similarly sized neighbour Helheim Glacier (HG), accounts for about 6% of GrIS drainage (Bevan et al., 2012). KG and HG flow into Kangerdlugssuaq Fjord (KF) and Sermilik Fjord (SF) respectively. As was the trend throughout Greenland, KG and HG both underwent steady retreat and acceleration between 1995 and 2010 (Bevan et al., 2012). In 2005, however, both glaciers simultaneously experienced sharp acceleration and retreat, which points towards a common forcing, and

has motivated oceanographic interest in the area (Howat et al., 2007; Hanna et al., 2009).

KF is up to 900 m deep, around 6 km wide and 75 km long from mouth to calving front (Inall et al., 2014), running at 20° west from north (Sutherland et al., 2014b) and displaying a U-shaped cross-section. At the mouth, where the fjord widens to around 20 km, there is a deep (480 m) sill. The Rossby radius within KF has been estimated at 7-9 km based on summertime observations (Inall et al., 2014; Sutherland et al., 2014b), placing KF as a narrow fjord.

From the mouth of KF, the deep (∼650 m), wide Kangerdlugssuaq Trough (KT) extends straight across the shelf to meet the Irminger Basin. KT is the key pathway between the warm, salty waters of the Irminger Basin and the entrance to KF (Koszalka et al., 2013; Inall et al., 2014; Gelderloos et al., 2017).

The tides in the region are relatively weak (Sutherland et al., 2014b), with sill depth around 2 orders of magnitude greater than mean tidal range, suggesting that tides are not a dominant agent of exchange. Icebergs, calved at the KG terminus, are present in KF year round (Sutherland et al., 2014a), and sea ice mélange forms seasonally.

2.2.3 Hydrography

The East Greenland Current (EGC) transports cold, freshwater south from the Arctic, along the East Greenland shelf edge and on the shelf itself. Within the EGC, distinct water masses have been identified. Polar Surface Water (PSW) is a relatively light water mass with potential temperature $\Theta < 0°C$ and potential density $\sigma_\theta < 27.70$. A variant of PSW called warm Polar Surface Water (PSWw) has also been observed, which has been modified both through mixing with Arctic sea ice melt water and through atmospheric heating, making it warmer and fresher, and hence lighter, than PSW (Inall et al., 2014). In general, PSWw displays $\Theta > 0°C$, but can exhibit a wide salinity and temperature range depending on the extent of modification. The densest of the Arctic origin water masses detected off the East Greenland coast, Polar Intermediate Water (PIW), is characterised by $\sigma_\theta > 27.70$ and $\Theta < 0°C$ (Sutherland and Pickart, 2008). PIW, PSW and PSWw are collectively known as Polar Water (PW) and typically make up the upper 100-200m of the water column (Sutherland and Straneo, 2012).

Alongside the EGC runs the East Greenland Coastal Current (EGCC) (Bacon, 2002; Harden et al., 2014). The current displays similar Θ/S_A properties to the EGC but resides landward of it, on top of the shelf, bounded by the coastline. The structure of the EGCC, both upstream and downstream of the KF entrance, is shown in Sutherland and Pickart (2008). The highly seasonal nature of the EGCC indicates that is fed by glacial runoff and sea ice melt (Sutherland and Pickart, 2008). However, as the EGCC is not detected upstream of KT (Sutherland and Pickart, 2008), it is possible that the EGCC is established

by the redirection of a branch of the EGC steered topographically by KT, and/or that the freshening influence of KG initiates the current. It has been detected as far south as Cape Farewell, although its presence in winter is uncertain, due to lack of year-round data (Bacon et al., 2014).

The Irminger Current (IC) is a branch of the North Atlantic Current which circulates anticlockwise around the Irminger Basin and along the SE Greenland shelf break. The IC transports warm, saline sub-tropical water or Atlantic Water (AW) southward along the edge of the SE Greenland shelf, at greater depth than that of the EGC. AW is characterised by $4.5 < \Theta < 6.5$°C and $35 < S_A < 35.3$ g/kg (Sutherland and Pickart, 2008). The EGC and IC merge into a composite flow south of the Denmark Strait, which meanders and sheds eddies as it traverses the shelf, leading to a highly variable SE boundary to the GrIS (Magaldi et al., 2011). Intermediate Water (IW, $1 < \Theta < 4.5$°C, $34.6 < S_A < 35$ g/kg) is used to described waters with an AW influence but which have been cooled and freshened due to mixing with local waters. This variant of subtropical-influenced water has been observed to constitute the intermediate layer within KF (Inall et al., 2014).

Modelling studies of the wider SE Greenland shelf region (Magaldi et al., 2011; Koszalka et al., 2013; Gelderloos et al., 2017) show KT to be a key pathway for AW towards the mouth of KF. A topographically steered circulation pattern resides in KT, which advects a branch of IC/EGC water landward from the shelf break. Gelderloos et al. (2017) find a seasonality to this behaviour, with the transport of IC-origin water to the mouth of KF doubling in winter.

The deepest water mass present in the Irminger Basin is Denmark Strait Overflow Water (DSOW). These dense ($\sigma_\theta \geq 27.8$) waters are released over the Denmark Strait sill in pulses, called "boluses", which cascade down to the deep waters of the Irminger Basin every 2-5 days (Koszalka et al., 2013; Cenedese and Adduce, 2010). DSOW has been simulated circulating in KT (Koszalka et al., 2013) and has been observed in the KF interior (Inall et al., 2014).

Glacial Melt Water (GMW, $\sigma_\theta < 24$) has been observed within SE Greenland fjords, including KF (Inall et al., 2014). GMW originates from one of the three sources noted earlier; namely runoff, subglacial discharge and melt water from the ice/water interface.

2.2.4 Mechanisms for Exchange

A distinguishing characteristic of the two largest glacial fjords of SE Greenland, KF and SF, is their deep entrances which allow information about the stratification structure on the shelf to be easily communicated to the fjord interior. Typically, a layer of PW—some combination of PSWw, PSW and PIW—overlays a layer of AW influenced IW. The two

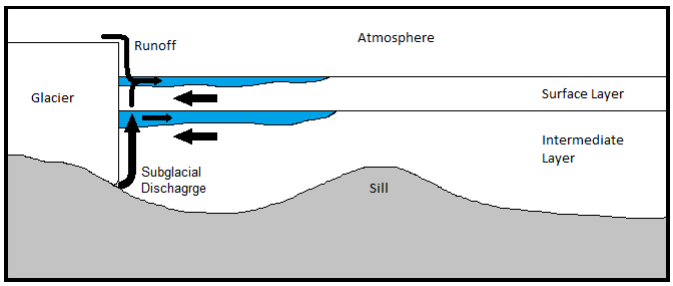

Figure 2.2: Illustration of a four-layer, freshwater-driven circulation scheme.

central circulation schemes described in the literature, four-layer circulation and intermediary circulation, both rely intrinsically upon this ambient stratification.

2.2.4.1 Freshwater-driven Circulation

In order for the temperature of the ocean to impact glacial stability requires circulation patterns which advect water from the shelf to the fjord interior and subsequently to the head of the fjord, the typical location of glacier termini. The best established mechanism for this is freshwater-driven estuarine circulation, which has been widely observed as an agent of exchange in high-latitude fjords (Motyka et al., 2003; Jenkins, 2011; Mortensen et al., 2011; O'Leary and Christoffersen, 2013; Motyka et al., 2013). This mechanism contains a positive feedback whereby increased melting drives further convection at the glacier terminus, enhancing the along-fjord overturning circulation and ultimately drawing more warm, shelf-origin water into the fjord (Xu et al., 2012).

Recent observations from the large fjords of SE Greenland (Straneo et al., 2011; Sutherland and Straneo, 2012; Inall et al., 2014) indicate that freshwater is supplied chiefly by subglacial discharge as opposed to surface runoff. Much of the freshwater is therefore injected deeper than the PW/IW interface. Turbulent mixing associated with buoyant plume dynamics causes the GMW plume to entrain ambient waters, increasing its density. A portion of the plume finds neutral buoyancy at the interface between the PW and IW layers, where it spreads horizontally. The result is a four-layer circulation regime, akin to two estuarine circulation cells stacked vertically, whereby GMW flows out both at the surface and at the pycnocline (Straneo et al., 2011; Sole et al., 2012; Inall et al., 2014; Cowton et al., 2016). These outflows entrain both PW (from above and below) and IW (from above) and drive compensatory inflows of both these layers.

Classically, estuarine circulation describes fjords with no external stratification, i.e. those allowing entry to only one shelf water mass due to shallow sill depth (Straneo et al., 2011). Due to the deep sills at both KF and SF, both the PW and IW layers on the shelf have free communication with the fjord interior. This is a requirement for the complex, multi-cell

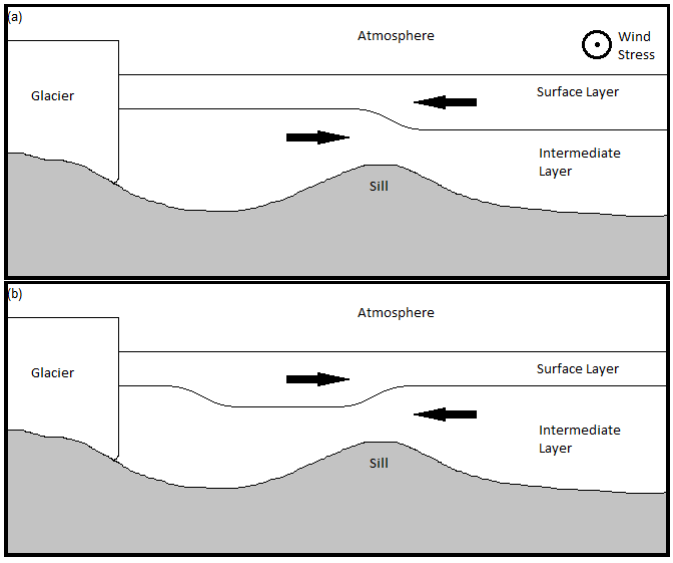

Figure 2.3: Illustration of intermediary circulation. Panel (a) shows the behaviour during a barrier wind event while (b) shows the behaviour after the wind relaxes. Note that in (b) the signal due to initial downwelling has not yet necessarily propagated to the head of the fjord.

overturning circulation scheme observed there. Both the upper and lower layer inflows could potentially contribute to melting at the terminus, and Inall et al. (2014) assert that PSWw has a significant capacity to melt glacial ice. This is corroborated by Christoffersen et al. (2011) who assert that although PSWw is not observed in KF every year, there is a strong correlation between years of high glacial melt, and the years in which PSWw was present.

2.2.4.2 Shelf-driven Circulation

The deep-sills at the mouths of the two major fjords in SE Greenland, KF and SF, give rise to the potential for changes in the height of the pycnocline on the shelf to propagate into the fjord, generating baroclinic exchange flows between the fjord and the adjacent coastal waters. This mechanism, termed "intermediary circulation", has been observed to generate rapid flows in SF (Straneo et al., 2010; Jackson et al., 2014) and has also been proposed as a dominant driver of exchange in KF (Christoffersen et al., 2011; Sutherland et al., 2014b). Numerous controls may drive intermediary circulation, although one primary control is the effect of along-shelf barrier winds on the surface layer of shelf water (Straneo et al., 2010; Christoffersen et al., 2011).

Barrier winds are strong ($> 20\mathrm{m\,s^{-1}}$), northeasterly wind events which occur on the SE Greenland shelf approximately once per week during the winter, typically lasting 2-3 days

(Harden et al., 2011). Barrier winds are strongest around the Denmark Strait where they occur mainly in two distinct locations: Denmark Strait North (DSN), which is near the entrance to KF, and Denmark Strait South (DSS), adjacent to the SF entrance. By driving onshore velocities in the Ekman layer, barrier winds cause downwelling at the coast. This causes a depression in the AW/PW interface, driving an inflow in the surface layer and an outflow at depth as the fjord water aims to achieve equilibrium with the adjacent coastal waters (Straneo et al., 2010). This signal propagates up-fjord as an internal wave. Once the along-shore wind relaxes, shelf conditions revert back to their original state and the reverse circulation takes place in the fjord in order to match the shelf. Current and hydrography observations in SF from winter 2009-10 (Jackson et al., 2014) show a vertically sheared, two layer flow which alternates on a timescale of around 3-4 days, consistent with timescale for synoptic weather patterns (Sutherland et al., 2014b). Wintertime observations from KF are limited to a single mooring location in the mid-fjord, with a depth range limited to $\sim$ 200-300 m (Jackson et al., 2014), leading to a large uncertainty in the dominant circulation scheme in KF during those months.

2.2.4.3 Relative Importance

Sutherland et al. (2014b) estimated the estuarine exchange, Q_e, in KF and SF by using three different parameterisations and taking the mean. The three parametrisations used were: (1) the Knudsen relation, which describes two-layer estuarine flow and is constrained by volume and salt conservation (Knudsen, 1900); (2) an approach based around hydraulic control, previously used for fjord which are narrow, or shallow, at the entrance (Stommel, H. and Farmer, 1953); (3) an estimate which employs theory for partially-mixed estuaries (MacCready and Geyer, 2010). This procedure yields the values $Q_e = 4.7 \times 10^3 \mathrm{m^3 s^{-1}}$ and $Q_e = 3.3 \times 10^3 \mathrm{m^3 s^{-1}}$ in KF and SF respectively. They also developed an order of magnitude estimate for the exchange due to intermediary circulation, Q_i, based on the dimensions of KF and SF and the observed stratification. Values of $Q_i = 6.6 \times 10^4 \mathrm{m^3 s^{-1}}$ and $Q_i = 8.5 \times 10^4 \mathrm{m^3 s^{-1}}$ are calculated for KF and SF respectively, implying flow speeds of $\sim 10 \mathrm{cm\,s^{-1}}$. Although there is an uncertainty in the estimates used, the domination of Q_i over Q_e by over an order of magnitude is a strong indicator that intermediary circulation is the predominant hydrodynamic driver. Sutherland et al. (2014b) note that even in summer, when Q_e is enhanced due to melt while Q_i is reduced due to weaker coastal winds, intermediary circulation is still likely to dominate. This is in contrast to, for example, Le Conte Glacier in Alaska , which terminates in a smaller, shallow-silled fjord in which $Q_i/Q_e \approx 1$ (Sutherland et al., 2014b). Hence, there is reason to believe that the ratio Q_i/Q_e is heavily dependent on sill depth, as well as being highly seasonal.

A modelling study of KF by Cowton et al. (2016) suggests that intermediary circulation is

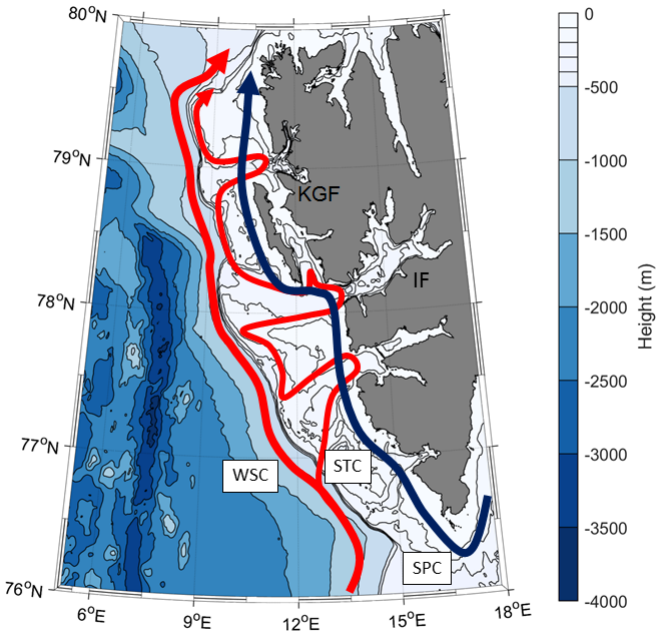

Figure 2.4: Bathymetry and circulation in west Spitsbergen. The WSC and STC are shown in red and the SPC is shown in blue. The locations of Isfjorden and Kongsfjorden (denoted IF and KGF on map) are shown.

highly effective at drawing shelf water into the fjord mouth. However, due to the alternating nature of this circulation scheme, they find it to be ineffective at delivering these waters into the upper reaches of the fjord where they can influence glacial stability. They find that the steady overturning circulation driven by freshwater input, although less energetic, is more effective at melting ice, delivering a continuous supply of heat to the glacier terminus.

2.3 West Spitsbergen

2.3.1 Topography

Like the southeast coast of Greenland, the west coast of Spitsbergen, the largest island in the Svalbard archipelago, is home to many glacial fjords. The 200 m deep continental shelf stretches around 40-60 km west of the coastline, and is intersected by a series of cross-shelf canyons which generally lead to the mouths of large fjord systems. At the shelf break, the seabed drops to a basin depth of around 2000-2500 m.

2.3.2 Isfjorden

Isfjorden is the largest fjord on the west coast of Spitsbergen. It is around 10 km wide at the entrance, broadening to around 20 km inside, and is connected at the mouth to a large cross-shelf trough system (Isfjordrenna). Isfjorden forms the trunk of a large, complex fjord system, with Nordfjorden branching off to the north, itself leading to Dicksonfjorden and Ekmanfjorden, and extending into Sassenfjorden, which leads to Tempelfjorden and Billefjorden to the west, such that the entire system is around 100 km long with an area of 2490 km^2 (Muckenhuber et al., 2016). Two smaller fjords, Grønfjorden and Adventfjorden, are situated along the southern shore. Around 200 m deep, though with quite variable bottom topography, Isfjorden has no sill at the entrance forming a topographic barrier to exchange and instead deepens to over 400 m there. Cottier et al. (2010) put the Rossby radius in the range $3.5 < L_R < 6$ km for Svalbard fjords, firmly categorising Isfjorden as a broad fjord. As the fjord width exceeds L_R even at the fjord mouth, we anticipate exchange flows with cross-fjord velocity variability.

Sea ice coverage around Svalbard has undergone a substantial reduction in recent decades (Pavlov et al., 2013; Tverberg et al., 2014; Onarheim et al., 2014b), a change which has been linked to an increased presence of AW. In Isfjorden, annual maximum fast ice coverage decreased from 57.5% during 2000-2005 to 23.2% during 2006-2014 (Muckenhuber et al., 2016). Svalbard's glaciers have undergone acceleration and retreat since 2000, which has also been linked to fjord water temperature (Luckman et al., 2015; Schellenberger et al., 2015), and Atlantification of Svalbards fjords has had a significant impact on the local ecosystem (Willis et al., 2008; Berge et al., 2015). Isfjorden has limited tidewater glacier cover in comparison to the major fjords of SE Greenland or other heavily glaciated fjords in Svalbard (Nilsen et al., 2016), with most of the glacial activity confined to the north side (Nilsen et al., 2008).

2.3.3 Hydrography

Oceanic heat is delivered to Svalbard from the Atlantic Ocean via the West Spitsbergen Current (WSC), which transports Atlantic Water (AW, $\Theta > 3°\mathrm{C}$, $35.1 < S_A < 35.4$ g/kg) northwards along the shelf break. A branch of the WSC is guided onto the shelf where it follows the topographic contours of cross-shelf troughs (Cottier et al., 2005; Nilsen et al., 2008, 2016). This current, named the Spitsbergen Trough Current (STC), is able to draw AW into the mouths of west Spitsbergen's fjords, and is particularly well connected to Isfjordrenna (Nilsen et al., 2016). The Spitsbergen Polar Current (SPC) runs parallel to the WSC on the shelf, carrying Arctic Water (ArW, $\Theta < 1°\mathrm{C}$, $34.5 < S_A < 35$ g/kg) from east of Spitsbergen. ArW is formed due to sea ice melting and brine rejection in Storfjorden

and the Barents Sea (Skogseth et al., 2004) and is lighter than AW, though still relatively saline. The along-shelf current and hydrography structure is seen in the observed sections from the Isfjorden entrance, normal to the coastline, in Nilsen et al. (2008).

2.3.4 Mechanisms for Exchange

The coastal SPC runs across fjord entrances, and acts to isolate the fjords of west Spitsbergen from the influence of AW via a mechanism called geostrophic control. Prevailing winds are from the south (Nilsen et al., 2016), and act to pile up ArW at the coastline, driving barotropic transport of the SPC and generating a cross-shelf tilt (downwards towards the coast) in the isopycnals. When winds relax, or switch to northerlies, the isopycnals level out, and the associated overturning circulation advects AW in the lower layer coastward (Cottier et al., 2007). Northerly winds also act to weaken the barotropic pressure gradient driving the SPC and hence weaken geostrophic control at the fjord mouth. If the fjord water is less dense than shelf-water, this process opens the fjords to AW exchange in the deep layer (Cottier et al., 2005).

Nilsen et al. (2016) recently identified an alternative mechanism for enhanced AW transport onto the shelf. Enhanced southerly winds on the shelf act to strengthen the westward barotropic pressure gradient by increasing sea surface tilt. This strengthens both the SPC and WSC; however, due to coastward migration of the maximal sea surface gradient, the WSC is forced to follow shallower bathymetric contours. This increases the supply of AW into the STC at the shelf break, and also encourages the STC to flow further onto the shelf. Nilsen et al. (2016) find, using a barotropic ocean model, that greater southerly wind stress increased the extent to which the barotropic circulation in Isfjordrenna penetrates the Isfjorden mouth region.

In a study of Kongsfjorden, a neighbour of Isfjorden situated further north, Inall et al. (2015) identified coastal-trapped waves (CTWs) as a significant driver of fjord shelf exchange. A class of internal wave, CTWs are of subinertial frequency and in geostrophic balance between the Coriolis force and the pressure gradient associated with water piled up against a topographic boundary. They were observed to propagate into the fjord along the southern bank, with laterally decaying amplitudes moving into the fjord. Similar to the intermediary circulation described in SE Greenland, the internal wave activity was accompanied by opposing currents above and below the pycnocline, with sign alternating temporally. The CTWs were generated, again like those in SE Greenland, by weather systems on the shelf. The critical distinction between the two phenomena is fjord width with respect to L_R which, due to latitudinal dependence, is greater in SE Greenland than in Svalbard.

Discussion of estuarine circulation is largely absent from the literature on Svalbard fjord-

shelf exchange. This is likely due to the relatively small freshwater catchment areas compared to the major fjords of SE Greenland. Inall et al. (2015) estimates that estuarine exchange is weak there in comparison to tidal and intermediary circulation, while Sundfjord et al. (2017) find that estuarine circulation is of limited significance away from glacier termini.

2.4 Current Understanding and Knowledge Gaps

2.4.1 Southeast Greenland

The acquisition of oceanographic data from KF and SF is one of the main obstacles in understanding the hydrodynamic circulation in those fjords. Over the last two decades, when changes in Greenland's outlet glaciers have been the most dramatic, there have been increased efforts to gather such data. Sea ice cover, along with adverse weather conditions, has limited cruise campaigns to the summer months, and questions remain over the extent to which seasonal changes influence the circulation within KF. The scarcity of wintertime observations from the interior of both SF and, especially, KF may have introduced a bias towards freshwater input, which peaks in summer, as the dominant driver of fjord-shelf exchange. The only existing wintertime measurements from KF are from a single mooring deployment (Jackson et al., 2014), where a time series of temperature and salinity was acquired at a single location over a relatively narrow depth range. The recent modelling study of KF by Cowton et al. (2016) made significant progress in quantifying both intermediary and freshwater-driven circulation under summertime conditions; however, the tendency for barrier winds to occur during the winter months suggests that the picture is still incomplete. The rapid intermediary exchange flows observed at SF (Straneo et al., 2010; Jackson et al., 2014), together with the simulated two-fold increased in IC water transport to the KF mouth during the winter months (Gelderloos et al., 2017), reinforces the necessity to better understand wintertime circulation and exchange at KF.

It is not clear the extent to which the Earth's rotation influences the circulation within KF. Both intermediary and four-layer circulation are interpreted as simple vertical overturning schemes, with no cross-fjord velocity variability. Straneo et al. (2011) and Sciascia et al. (2013) describe SF as a strictly two-dimensional system, arguing that the fjord is not sufficiently broad to be influenced by rotation. Our understanding of the SF circulation has, however, evolved in recent years, with Sutherland et al. (2014a) observing frequent recirculation using icebergs as drifters, and concluding that cross-fjord velocity gradients are significant. Inall et al. (2014) observed significant cross-fjord variability in KF during September 2010, indicating that KF is a broad fjord. The model by Cowton et al. (2016) found some cross-fjord variability in the KF mouth, but the fjord interior was dominated by

two-dimensional overturning schemes. The study was carried out using laterally uniform forcing fields at the fjord mouth, and may have failed to capture the effect of the three-dimensional, geostrophically balanced circulation around the head of KT. If would be instructive to conduct an integrated KF/KT system study in order to discern where, if at all, the three-dimensional circulation in KT transitions to a two-dimensional overturning circulation in KF. If KF were truly a broad fjord, there would exist the potential for a geostrophically balanced, uninterrupted pathway from the shelf break to the KG terminus, which would present a new mechanism for oceanic heat delivery towards the GrIS.

Deployment of numerous moorings, arranged in both along- and across-fjord arrays, would be enlightening, allowing along-fjord overturning circulation schemes to be classified and quantified while capturing any rotational effects. Future winter mooring deployments would also be able to give context to the existing records, and a repeatedly occupied station would enable understanding of interannual changes. There is, however, a significant risk associated with deploying multiple moorings in the presence of large icebergs. An alternative technique which could alleviate the need for wintertime cruise campaigns is the use of autonomous vehicles in high-latitude fjords. Dowdeswell (2004) deployed an autonomous underwater vehicle (AUV) to the mouth of KF (the data is shown in Inall et al. (2014)). However, KF presented a challenging environment for the AUV and several technical problems arose during the campaign which prevented it gathering data from further inside the fjord. Glider technology has advanced in subsequent years (Schofield et al., 2007; Wood and Stephen, 2009), and presents some advantages over AUVs with the potential for longer mission durations, shore-based piloting and deployment and recovery away from the region of interest. The use of gliders under Arctic sea ice is an emerging technique (Lee and Thompson, 2017) with many obstacles to overcome, however they have not been used to study the interior of fjords. The deployment of a glider to KT and the KF mouth during winter could potentially yield insightful data on the nature of the exchange there. However, deployment to the KF interior will remain impracticable unless techniques for flying gliders in regions of significant sea ice and iceberg cover become better established.

2.4.2 West Spitsbergen

Understanding what drives the increased oceanic heat delivery towards west Spitsbergen's fjords is an important aspect of understanding the recent, drastic changes to the Arctic climate (Førland et al., 2011). Studies of cross-shelf exchange at Isfjordrenna, and connectivity between the shelf and the fjord mouth, have improved our understanding of the three-dimensional exchange regimes in broad fjords (Nilsen et al., 2008, 2016). In order to fully understand the changes in sea ice cover and marine biology within Isfjorden, it is necessary to extend this research into the fjord interior, so as to describe the response

of the fjord interior to exchange events and quantify the efficacy of Isfjorden's internal circulation at distributing incoming AW throughout the fjord.

Due to largely open waters and relative ease of access, west Spitsbergen fjords present a perfect "laboratory" for studying fjord-shelf exchange processes in general. The situation there displays many obvious similarities to that in SE Greenland, with cross-shelf transport of AW facilitated by topographically steered branches of shelf edge currents, as well as coastal currents carrying Arctic origin waters across fjord mouths. Along-shelf wind stress has been advanced as the dominant control on exchange at both locations.

2.5 Approach

Motivated by the knowledge gaps identified in the previous section, a numerical model comprising the combined KT/KF system was selected as a means of progress. In particular, the model was aimed specifically at studying KF during winter. Both shelf-driven and fjord-driven exchange are included in the model, and the model boundaries are placed away from the KF entrance so as to minimise boundary effects on exchange. This approach was also chosen to provide a full three-dimensional description of the circulation, thus quantifying the importance of rotation.

A secondary objective of this thesis was to explore the use of glider technology for studying fjord-shelf exchange. In conjunction with the modelling study outlined previously, a glider was also deployed to the Irminger Sea in September 2015, with the ambition of surveying KT and the KF mouth region. However, strong ($\sim 1\,\mathrm{m\,s^{-1}}$) slope currents prevented access via the south end of KT, and the instrument was later lost in bad weather while heading for recovery. The use of gliders in Svalbard fjords presented less of an obstacle, and a glider mission to Isfjorden was devised for November 2014 in order to address the issues outlined previously for the region. Due to the temporal and spatial coverage, as well as depth-averaged current information afforded by gliders, this study was designed to advance the current understanding of the internal circulation and hydrography structure in Isfjorden and broad fjords in general. The deployment also allowed the practice of flying gliders in restricted fjordic regions to be introduced without the added risk posed by icebergs and sea ice. The similarities between Isfjorden and KF, in terms of fjord-shelf exchange, mean that such a study is well placed to inform future Greenland work.

Chapter 3

Influence of Barrier Wind Forcing on Heat Delivery Towards the Greenland Ice Sheet

Adapted from *Fraser, N. J. and Inall, M. E. (2018), Journal of Geophysical Research: Oceans.*

3.1 Introduction

3.1.1 Background

The glaciated fjords which permeate the Greenland coastline act as gateways for heat delivery from the ocean to the Greenland Ice Sheet (GrIS) (Rignot and Kanagaratnam, 2006; Hanna et al., 2009; Straneo et al., 2010; Inall et al., 2014). Due to significant freshwater input, these regions are typically cooler and less saline than waters on the continental shelf. A fjord's ability to deliver heat to the GrIS, or freshwater to the open ocean, is dependent on the fluid dynamics of the fjord interior. The circulation is governed in general by a variety of forcing mechanisms, which vary in importance both seasonally and between fjords due to differences in local setting. The dominant drivers of circulation in a Greenland fjord are freshwater input, wind stress, tides, sea ice formation/melting and shelf exchange (Cottier et al., 2010). Freshwater enters the fjord via iceberg calving, direct melting at the glacier-ocean interface, surface runoff, and subglacial discharge (Cottier et al., 2010). In broad fjords (with respect to the internal Rossby radius of deformation, L_R) we expect the Coriolis effect to significantly influence the dynamics, giving rise to an across-fjord aspect to the circulation which would otherwise be negligible (Inall and Gillibrand, 2010).

Over the last two decades, the GrIS has undergone mass loss at an unprecedented rate, accounting for $\sim 16\%$ of global sea level rise during this period (Khan et al., 2014). Thinning of the ice sheet has been most pronounced near the coast, with many major outlet glaciers observed to accelerate and retreat over this period (Rignot and Kanagaratnam, 2006; Nick et al., 2009; Bevan et al., 2012). These changes to the GrIS coincide with an increase in water temperature around southern Greenland, indicating that they are triggered by oceanic heating (Hanna et al., 2009; Straneo and Heimbach, 2013). On the east coast, during 2000-2005, interannual changes in glacial dynamics are observed and equatorward of 69°N (Seale et al., 2011), which corresponds to a region of strong latitudinal gradient in ocean temperature, further evidence of ice-ocean interaction as the principal driver of GrIS reduction.

3.1.2 Objective

The objective of this paper is to better understand the wintertime dynamics of a large Greenlandic fjord and, by extension, large glaciated fjords in general. The study is focussed on the interaction between fjord and shelf driven by along-shelf winds, and the additional effects in broad fjord systems due to the Earth's rotation. We tackled this problem by designing a realistic numerical hydrodynamic model of the fjord and adjacent shelf region, allowing the heat delivery towards the glacier front to be quantified directly under a variety of wind forcing scenarios. The paper is structured as follows: the remainder of section 1 describes the oceanographic setting and outlines gaps in the current understanding, providing the rationale for conducting winter-specific modelling experiments. Section 2 details the model grid, bathymetry, initial conditions and forcing fields, before explaining the experimental configuration. In section 3 the model output is presented, revealing a mean flow field strongly influenced by the Earth's rotation in all model experiments. Wind forcing is shown to be linked with internal wave activity, which is seen to greatly impact along-fjord volume and heat exchange. Also, due to increased advection and vertical mixing, the water column structure in the fjord mouth is altered following wind forcing, with implications for subsequent exchange. In section 4 we interpret the dynamical response to wind forcing as coastal trapped wave activity, and discuss the the implications for heat delivery towards the GrIS during winter in the context of the existing literature on high-latitude fjord-shelf exchange. Our key outcomes are summarised in section 5.

3.1.3 Setting

Kangerdlugssuaq Glacier (KG) in southeast (SE) Greenland is the second largest outlet glacier of the GrIS by discharge (Enderlin et al., 2014), and drains around 4\% of the GrIS

by area (Bevan et al., 2012). KG drains into Kangerdlugssuaq Fjord (KF, Figure 2.1), which is around 75 km in length, 6 km wide and 900 m deep, and oriented at approximately 340° from north (Inall et al., 2014; Sutherland et al., 2014b; Cowton et al., 2016). The entrance of KF opens onto a relatively broad region of the SE Greenland continental shelf. A deep trough (Kangerdlugssuaq Trough, KT hereafter) crosses the shelf here, running southward from the KF entrance to intersect the shelf break at the northern boundary of the Irminger Basin. KT has a maximum depth of around 650 m, while the typical shelf depth is around 300 m. It is separated from KF by a relatively deep sill of around 480 m. In 2004-05, KG experienced profound acceleration and retreat, before subsequently reverting to a stable state (Bevan et al., 2012). This sudden change has been linked to increased water temperatures around SE Greenland at that time (Hanna et al., 2009). In order to understand these changes in glacial dynamics, both in KG and throughout Greenland, it is therefore necessary to quantify the up-fjord heat flux associated with the various drivers of fjordic circulation.

The SE Greenland shelf generally displays seasonal variation in water column structure. Polar Surface Water (PSW), a relatively cold, light water mass ($\Theta < 0°C$, $\sigma_\theta < 27.70$) (Sutherland and Pickart, 2008), occupies the upper layer. It is transported into the region via the East Greenland Current (EGC), a geostrophically balanced slope current carrying water southward from the Arctic Ocean along the east Greenland continental shelf break (Figure 2.1). A portion of the PSW may be warmed by the atmosphere and freshened by ice melt during transport, giving rise to the seasonal variant Warm Polar Surface Water (PSWw, $\Theta > 0°C$, $\sigma_\theta < 27.70$) (Inall et al., 2014). The EGC also carries the colder, deeper lying Polar Intermediate Water (PIW, $\Theta < 0°C$, $\sigma_\theta > 27.70$) from the Arctic Ocean (Sutherland and Pickart, 2008). These three Arctic origin water masses, PSW, PSWw and PIW, are collectively termed Polar Water (PW), and generally occupy the upper 75-300 m of the water column (Bacon et al., 2014). On the shelf is the East Greenland Coastal Current (EGCC), a second source of PW into the region (Bacon, 2002). This high speed, coastally steered surface current is thought to be highly seasonal (Bacon et al., 2014) due to the influence of freshwater from the eastern GrIS and increased wind forcing in winter. The EGCC is not observed upstream of the KF entrance and is thought to be fed, at least in part, by a branch of the EGC which is directed landwards by KT before continuing southward along the coast (Sutherland and Pickart, 2008). The freshening influence of the KF system may also play a part in the establishment of the EGCC at the head of KT. Below PW lies Atlantic Water (AW, $\Theta \sim 4.5 - 6.5°C$, $S_A \sim 34.9 - 35.2$, Sutherland and Pickart (2008)), which is advected into the region via the Irminger Current (IC), a branch of the North Atlantic Current which circulates cyclonically around the boundary of the Irminger Basin after entering the basin west of the Reykjanes Ridge. The IC is the primary oceanic source of heat into the region. South of the Denmark Strait, the IC and

EGC merge into a composite flow, denoted the IC/EGC front hereafter, consisting of PW overlaying AW and following the shelf break. The IC/EGC front is prone to meandering and eddy shedding (Magaldi et al., 2011), giving rise to variability in the water mass structure on shelf and, crucially, allowing AW to flow westward of the shelf break, such that water mass exchange between the Irminger Basin and the shelf is episodic in nature. In a SE Greenland regional model by Gelderloos et al. (2017), a branch of the IC is seen to circulate into KT at the shelf break while, in summer, a second branch is found to go north through the Denmark Strait and across the shelf towards KT, thus advecting AW towards the mouth of the KF. The densest water mass in the region is Denmark Strait Overflow Water (DSOW, $\Theta < 0°C$, $34.9 < S_A < 35.2$, $\sigma_\theta \geq 27.8$). DSOW is released into the region in periodic boluses, which pass through the Denmark Strait and cascade down into Irminger Basin with a frequency of around 2-5 days (Koszalka et al., 2013). Modelling results suggest the DSOW can circulate in KT (Koszalka et al., 2013) and cross onto the shelf (Magaldi et al., 2011), and has been observed inside KF below sill depth (Inall et al., 2014).

Along-fjord temperature and salinity gradients are introduced by freshwater input at the terminus of KG and at 13 smaller outlet glaciers surrounding the fjord (Inall et al., 2014; Cowton et al., 2016). Inall et al. (2014) observe glacial melt water (GMW, $\sigma_\theta < 24.0$) in KF interior in September, alongside the aforementioned oceanic water masses. Although there is a dearth of observations from close to glacier termini, both modelling and theoretical studies (Jenkins, 2011; Xu et al., 2012; Sciascia et al., 2013; Cowton et al., 2015) suggest that stratification breaks down at the glacier terminus due to the buoyant plume dynamics associated with subglacial discharge and melting. In the classical picture of estuarine circulation, surface runoff at the glacier terminus drives an overturning cell which draws shelf water into the fjord via deep layer inflow. In the deep-silled fjords of SE Greenland, freshwater injected at depth forms a buoyant plume, and the entrainment of ambient fjord water can lead to a portion of this plume finding neutral buoyancy at the PW/AW interface rather than at the surface (Inall et al., 2014; Carroll et al., 2016; Cowton et al., 2016). Summer observations of KF confirm this, with outflow of GMW observed both at the surface and the pycnocline, and compensatory inflow in both the PW layer and the AW layer (Inall et al., 2014).

3.1.4 Exchange During Winter

An additional mechanism for the advection of heat into deep-silled fjords, termed intermediary circulation, has been recently identified in Sermilik Fjord (SF) (Straneo et al., 2010; Jackson et al., 2014), a similarly sized neighbour to KF. Exchange flows are triggered by along-coast barrier wind events, which drive strong baroclinic exchange flows as a result

of downwelling on the shelf. As the pycnocline on the shelf is initially depressed by the action of northerly coastal wind, inflow first occurs in the upper layer, with outflow in the lower, as the circulation within the fjord acts to match the stratification to that on the shelf. Once the wind relaxes, the pycnocline on the shelf upwells to a neutral position and the reverse process occurs, resulting in inflow in the warm lower layer. The mechanism was first described by Klinck et al. (1981) and has been observed to generate rapid exchange flows between SF and the adjacent shelf (Straneo et al., 2010), and estimates of the volume transport associated with intermediary circulation are an order of magnitude greater than that from freshwater-driven circulation, both in SF and KF (Sutherland et al., 2014b). While these estimates place intermediary circulation as the most significant driver of exchange in the major SE Greenland fjords, uncertainties remain over the time-averaged contribution towards heat transport.

Barrier winds are strong, northeasterly winds occurring on the SE Greenland shelf, generally confined to the winter months (when freshwater runoff and subglacial discharge are minimal), occurring on average once per week during December-February (Harden et al., 2011). Wintertime hydrographic observations of the KF interior are limited to a single mooring location from winter 2009-10 (Jackson et al., 2014), leading to large uncertainties in the extent to which intermediary circulation contributes towards melting at the KG terminus. Regional modelling results suggest that heat supply towards the KF entrance is greater in winter than in summer (Gelderloos et al., 2017).

There have been a number of recent numerical modelling studies aimed specifically at assessing the relative importance of wind-driven and freshwater-driven exchange, which typically employ idealised topography in order to maximize generality (Cowton et al., 2015; Carroll et al., 2016, 2017; Spall et al., 2017). There is, however, no firm consensus on the significance of heat delivery from the ocean to the GrIS during winter.

A realistic numerical modelling study of KF by Cowton et al. (2016), which simulated the effect of barrier winds on KF by altering the stratification at the fjord mouth, found that while intermediary circulation is effective at bringing shelf-resident water into the fjord interior, this water does not penetrate into the upper reaches of the fjord so as to influence glacial stability. Whilst the result is highly illuminating, the horizontally uniform boundary fields fail to account for any cross-fjord variability in the fjord mouth. The circulation at the northern end of KT is influenced by rotational effects (Koszalka et al., 2013), and the nature of the interaction between barrier wind induced downwelling and the dynamics in the fjord mouth remains poorly understood.

The large outlet fjords of SE Greenland have previously been presumed narrow in comparison to L_R (Christoffersen et al., 2011; Sciascia et al., 2013), estimated by Sutherland et al. (2014b) to be $\sim$9 km, such that cross-fjord variability may be neglected. Recent

results from KF and SF, however, demonstrate cross-fjord variability in the hydrography and circulation of these fjords (Inall et al., 2014; Sutherland et al., 2014a). This gives rise to the potential for the geostrophically balanced circulation in KT extending to the KF interior, acting as an uninterrupted pathway transporting heat between the continental shelf and KG.

3.2 Methods

A high-resolution modelling study was carried out in which the interaction of KF with the adjacent shelf seas were simulated under typical winter conditions. The model was forced using mean winter wind fields as a control case, and this was compared to simulations forced using wind fields designed to emulate typical barrier wind events. Glacial melt was simulated using a sub-gridscale parametrisation, thus providing a heat sink and freshwater source at the ice-ocean interface. Sea ice was parametrised through alteration of the wind fields. This work used the ARCHER UK National Supercomputing Service (http://www.archer.ac.uk).

3.2.1 The MITgcm

Model simulations were run using The Massachusetts Institute of Technology general circulation model (MITgcm) (Marshall et al., 1997), a highly versatile fluid dynamics simulator designed to operate on a wide range of scales in both the atmosphere and the ocean. It is built around solving the incompressible Boussinesq equations using the finite-volume method on a curvilinear coordinate system. These equations are in general non-hydrostatic, however the model may be configured to utilise the hydrostatic approximation, eliminating any vertical momentum within the fluid and simplifying the numerical integration. The grid spacing may be varied, or "telescoped", throughout the model domain, both in the horizontal and the vertical, and partial depth, or "shaved", cells help to deal with steep or complex bottom topography. A more comprehensive explanation of the inner workings of the MITgcm is given in Adcroft et al. (2004).

Model simulations were run using The Massachusetts Institute of Technology general circulation model (MITgcm) (Marshall et al., 1997), a highly versatile fluid dynamics simulator designed to operate on a wide range of scales in both the atmosphere and the ocean. It is built around solving the incompressible Boussinesq equations using the finite-volume method on a curvilinear coordinate system. These equations are in general non-hydrostatic, however the model may be configured to utilise the hydrostatic approximation, eliminating any vertical momentum within the fluid and simplifying the numerical integration. The grid spacing may be varied, or "telescoped", throughout the model domain, both in the

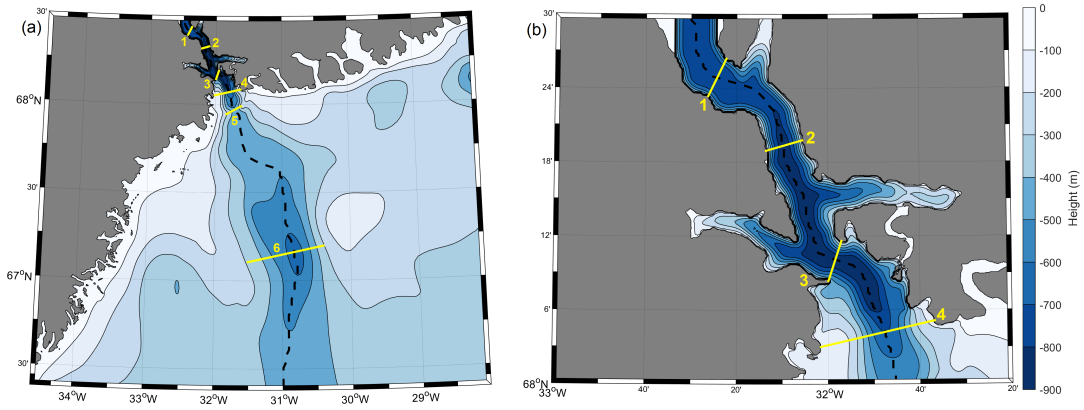

Figure 3.1: (a) shows the main model bathymetry, while (b) shows a zoom of the fjord interior. Cross-fjord sections are shown and numbered in yellow, the thalweg section is shown in dashed black. Section 1 is considered the "upper-fjord", Sections 2 and 3 are termed "mid-fjord", Sections 4 and 5 and termed "fjord mouth", while Section 6 crosses KT.

horizontal and the vertical, and partial depth, or "shaved", cells help to deal with steep or complex bottom topography. A more comprehensive explanation of the inner workings of the MITgcm is given in Adcroft et al. (2004).

3.2.2 Grid

The model grid is of size 240 × 240 × 100 cells ($lon \times lat \times z$). A telescopic grid was employed so that the relatively small-scale dynamics in and around KF could be captured in necessarily high resolution, while minimising the number of computationally expensive grid cells allocated to the wider shelf sea region. The maximum resolution of approximately 360 m×360 m is used throughout KF in the northern part of the domain. Moving east or west (south) of this region, the zonal (meridional) grid spacing increases linearly until the domain boundary, such that the southwestern and southeasternmost cells are the largest, with a resolution of approximately 4 km×4 km. The domain spans 66.38−68.5°N, 34.59−28.05°W and 1000 m depth, with a constant vertical resolution of 10 m.

3.2.3 Bathymetry

Raw bathymetry data for the shelf region came from the International Bathymetric Chart of the Arctic Ocean (IBCAO), and had a resolution of 30 arcseconds (the width of KT is around 1°). Although sufficiently detailed in the open ocean, this data set failed to properly capture the full depth and complex geometry of the KF interior. Swath bathymetry data gathered on the cruise JR106b to KF (Dowdeswell, 2004) were used in this region. The

data were interpolated onto the model's horizontal grid in the KF region, with the IBCAO data used everywhere else. The swath data did not cover the northernmost portion of KF, so a region of idealised bathymetry was created whereby a U-shaped cross-section was replicated for eight cells along the fjord, adjacent to the domain's northern boundary. The cells along the northern boundary itself were then mapped to zero in order to represent an idealised, vertical glacier front. The model bathymetry is shown in Figure 3.1.

3.2.4 Initial and Boundary Conditions

Open boundary conditions (OBCs) were generated using a larger domain MITgcm model. Barrier winds are thought to strongly influence stratification throughout the shelf sea region (Jackson et al., 2014) and are by no means localised around the KF/KT system (Harden et al., 2011). Barrier wind forcing on the model domain used here should not, therefore, be restricted to wind stress at the surface but also include changes in the OBCs. In order to tackle this, a larger domain was designed which was subject to the same atmospheric forcing as the main model so that, using a one-way nesting, output could be used to generate dynamic OBCs for the main model. The OBCs hence reflected changes in the water column symptomatic of the large scale atmospheric forcing. Tidal signal was not included in OBC forcing since tides in the region are weak ($\sim 1\text{cm}\,\text{s}^{-1}$, (Inall et al., 2014)). Free-slip conditions were assigned to all material side boundaries, with no-slip conditions used at the seabed. This choice is made due to the aspect ratio of the grid cells: side friction will have only a small effect on a 360 m diameter parcel of water, whereas bottom friction will play a much more significant role in the dynamics of a 10 m high column of water.

The larger domain is of size $144 \times 96 \times 130$ cells ($lon \times lat \times z$). Telescoping was used so that the region of interest, centered around KT, has a resolution of 4.5 km$\times$7.5 km while, moving away from this region, the cell size increases linearly towards the boundary. This relatively coarse grid is not sufficient to capture KF, but is able to capture the shelf dynamics in sufficient detail to provide boundary fields for the main model. The horizontal grid covers $59.56 - 70.39°$N and $44.4 - 8.16°$W, and is designed such that the main model domain lies entirely within the high resolution region. It is 4000 m deep, with the vertical resolution varying from 10 m in the surface layer to 100 m for the bottom 2000 m. Bathymetry data came from GEBCO and initial temperature and salinity fields came from Polar Science Center Hydrographic Climatology (PHC3.0; updated from Steele et al. (2001)) monthly climatology data. From these data, December, January, February (DJF) winter mean temperature and salinity fields were generated. Initial velocities were zero everywhere, as was the free surface height anomaly, η. The initial conditions were held constant at the boundary in all large domain simulations. A sponge layer was used to relax points near

the boundary towards these values, with a thickness of four cells and relaxation times $\tau_{inner} = 10$ days and $\tau_{outer} = 1$ day at the innermost and outermost sponge-layer cells respectively. Although sponge-layer velocities were relaxed towards zero, the prescribed density structure was such that a realistic large-scale thermohaline circulation was allowed to develop and communicate with the model interior. A volume flux balancing routine was used to ensure that the net flow across all boundaries summed to zero, with free-slip conditions used at all material boundaries. Atmospheric forcing fields (wind stress and net heat flux) were relaxed linearly to zero at the boundaries over a 4 cell wide zone. The larger domain was not designed to facilitate melting or runoff as there are no fjords or glaciers included, and was therefore unable to capture the freshening influence of KG or any other of SE Greenland's tidewater glaciers. Snapshots of Θ, S_A, u and v from day 50 onward were mapped to the main model grid, including KF interior, to provide initial and boundary conditions. This was done to ensure that the conditions on the shelf had settled into a balanced, dynamically consistent circulation pattern, with the IC and EGC well established, along with a geostrophically balanced circulation pattern established in KT. The initial water column inside the fjord closely matched that on the shelf, even below sill depth, due to the nearest-neighbour extrapolation method used.

3.2.5 Freshwater Input

Freshwater-driven circulation is an observed feature of KF (Inall et al., 2014), and of arctic fjords in general (Mortensen et al., 2011). This circulation is strongest in summer, when the fjord has a continual supply of freshwater due to glacier surface melt. Even during the winter months, however, glacier/iceberg melt water will drive some estuarine flow regime so long as sufficiently warm water is drawn into contact with the glacier front. It is therefore possible that when intermediary circulation is strongest, some freshwater-driven circulation is still active in the fjord. The interaction between these two circulation schemes is complex and likely non-linear. It is therefore advantageous to incorporate a realistic freshwater parametrisation into our numerical representation of the system, even though our study is focussed primarily on shelf-driven circulation. The MITgcm "iceplume" package (Cowton et al., 2015) was developed to overcome the problem of sub-gridscale plume dynamics at the ice-ocean interface in high-latitude numerical models. The package allows selected coastal grid locations to be considered ice and will modify the conditions in the adjacent fluid cells so as to replicate the influence of a buoyant plume, as described by Jenkins (2011) although half-conical in shape. Subglacial discharge may be prescribed by the user, while melting is calculated as a function of adjacent water temperature and pressure (Jenkins, 2011). This scheme circumvents the need to resolve plume dynamics numerically, such that the model may be run in hydrostatic mode. In the model presented here, plume parametrisation cells

were placed along the northern boundary to the fjord, representing the KG glacier front. The model does not include freshwater input from any of the smaller output glaciers of the KF system, nor does it account for the contribution due to melting of icebergs which, for deep-keeled icebergs, can be as significant as melting at the glacier terminus (Inall et al., 2014; Enderlin and Hamilton, 2014; Enderlin et al., 2016).

3.2.6 Atmospheric Forcing

Harden et al. (2011) identify two distinct locations where barrier wind events most commonly occur, Denmark Strait North (DSN; 67.7°N, 25.3°W) and Denmark Strait South (DSS; 64.9°N, 35.9°W). In order to characterise these events, they generated 96-hour composite wind fields which represent a typical event at each location during DJF. These composite wind fields were used as forcing fields for the model presented here. Upon examining both fields, only DSN fields were selected for model input as they produced higher peak wind speeds over KT (Figure 8 of Harden et al. (2011)). The 10 m wind velocity vectors were converted into wind stress vectors, $\underline{\tau}$, using the formulation of the drag coefficient by Large and Pond (1981). The initial and final 12 hours of the DSN wind event field was altered so that the wind smoothly ramped up from mean DJF wind conditions, and relaxed likewise. Mean DJF wind conditions were held constant at all times before and after wind events.

We obtained monthly mean fields for net shortwave and longwave radiation as well as sensible and latent heat flux from ERA-Interim reanalysis (Dee et al., 2011). From these fields, the 1979-2016 DJF climatology for total air-sea flux was generated. This forcing field was held constant in all model runs.

3.2.7 Sea Ice

The Kangerdlugssuaq region is subject to seasonal ice cover. Barrier winds are a predominantly winter phenomenon, and sea ice greatly influences the interaction between the wind and the ocean (Wadhams, 2000; Rabinovich et al., 2007; Martin et al., 2014). MITgcm contains a package in which ice can grow and melt at the free surface, and flow subject to drag forces from both the ocean and the atmosphere. The package requires, as both initial and boundary conditions, sea ice thickness, snow thickness, sea ice coverage and velocity and is designed to work alongside prescribed precipitation. This was deemed excessive for the study presented here, which is not designed to study sea ice dynamics. The MITgcm sea ice package was therefore eschewed in favour of a simpler approach, whereby sea ice is represented only through its effect on wind forcing.

Monthly mean sea ice coverage data were obtained from the National Snow and Ice Data

Centre (NSIDC), ranging 1979-2014. From these fields, the DJF winter climatology fields for SE Greenland were generated using only data from 1989-2008, the time interval from which the composite wind stress fields were taken. These data were then interpolated onto both the large model grid and the main model grid. The wind stress fields were then modified to reflect the presence of sea ice. The effect of sea ice on wind stress is tensorial: the magnitude of momentum transfer is altered due to the differing drag coefficients of ice and water, while the direction changes due to an additional Ekman-like effect from the layer of ice. In other words, we expect both a dilation and rotation of wind stress fields. In a modelling study of sea ice in the Arctic Ocean, Martin et al. (2014) find that the momentum transfer between air and ocean, τ_{ao}, initially increases with sea ice concentration, c, peaking around $c = 0.8$ before dropping off rapidly. They describe this behaviour using the simple model:

$$\tau_{ao}(c) = 0.05c - 0.07e^{-20(1-c)} + 0.035 \tag{3.1}$$

In the fjordic regions of SE Greenland, we presume that the momentum transfer is effectively zero where sea ice concentration $c = 1$. This is because, unlike in the Arctic Ocean, $c = 1$ here indicates fast ice, which imposes a rigid lid. To account for this, Equation 3.1 was altered such that $\tau_{ao}(1) = 0$. This may be achieved by changing the coefficient of the exponential term from 0.07 to 0.085. The following expression is therefore used:

$$\tau_{ao}(c) = 0.05c - 0.085e^{-20(1-c)} + 0.035 \tag{3.2}$$

This matches the original closely, differing only when the exponential term begins to dominate at large c. It was further assumed that the maximum deflection to the right,ϕ_{max}, would coincide with maximum ice cover, whereas no direction change is expected in open water. We used a linear sliding scale between these two extremes to prescribe the rotation as a function of c. All wind stress fields were therefore altered to account for sea ice cover using the formula $\underline{\tau}' = \underline{\underline{\Gamma}}(c) . \underline{\tau}$ with

$$\underline{\underline{\Gamma}}(c) = \frac{\tau_{ao}(c)}{\tau_{ao}(0)} \begin{pmatrix} \cos(c\phi_{max}) & \sin(c\phi_{max}) \\ -\sin(c\phi_{max}) & \cos(c\phi_{max}) \end{pmatrix} \tag{3.3}$$

Where $\tau_{ao}(c)$ is the expression given in Equation 3.2, normalised here by the open water value, $\tau_{ao}(0)$, to produce a dimensionless coefficient capturing the dilation effect. The 2×2 matrix captures the rotation. The value $\phi_{max} = 25°$ was used as the maximum angle of deflection, taken from Wadhams (2000). This value was taken from observations in the open ocean, and subsequent research (Rabinovich et al., 2007), has indicated that in coastal regions the value may be lower. The maximum angle of deflection, ϕ_{max}, is never

Day	Run-0	Run-1	Run-2
0-4	Prevailing wind	Barrier wind event	Barrier wind event
5-10	Prevailing wind	Prevailing wind	Prevailing wind
11-14	Prevailing wind	Prevailing wind	Barrier wind event
15-25	Prevailing wind	Prevailing wind	Prevailing wind

Table 3.1: Experimental configuration with regards to wind forcing.

achieved in practice as this occurs when $c = 1$ and therefore when $\underline{\tau}' = 0$. Inside the fjord, $c = 1$ at all times and in all simulations, so that direct wind forcing on the KF interior is eliminated and the effects of the barrier winds are felt only through changes on the shelf. Air-sea heat flux data from ERA-Interim accounts for local ice cover, so no modification of those fields was required.

3.2.8 Sub-Gridscale Mixing

The κ-Profile Parameterization (KPP, Large et al. (1994)) is a sub-gridscale vertical mixing paramertisation available as a package for MITgcm, and was implemented in all simulations presented in this paper. KPP is comprised of several mixing schemes, each representing a distinct mechanism for mixing. It treats mixing in the surface boundary layer and mixing in the ocean interior as separate problems with the boundary layer depth calculated at each grid location as a function of the bulk Richardson number. Boundary layer mixing is dependent on surface forcing fields while, in the ocean interior, shear-driven mixing is calculated as a function of the local Richardson number, with both the vertical mixing coefficient and its derivative constrained by continuity at the interface.

In the horizontal, Leith biharmonic viscosity was utilised (Leith, 1996). This regime is proportional to the relative vorticity gradient and dependent on local grid resolution, with scaling according to (Griffies and Hallberg, 2000).

3.2.9 Experimental Design

A crucial problem in designing the experiments was cultivating conditions within the fjord representative of wintertime, due to the paucity of observations from non-summer months. Prior to experimental runs, the model was subjected to a 100-day spin-up period with mean wind DJF forcing held constant. Subglacial discharge of $100\mathrm{m}^3\,\mathrm{s}^{-1}$ (an order of magnitude smaller than estimates by Sole et al. (2012) and Cowton et al. (2016) for peak summer runoff into the entire KG basin) was simulated at the fjord's northern boundary for 60 days, long enough establish quasi-stable buoyancy-driven overturning and realistic along-fjord temperature gradients. The fjord was then left to adjust for the remaining 40

days in the absence of subglacial discharge. From this state, the model was then further integrated in three distinct configurations. In the control case (Run-0), the prevailing DJF wind conditions were held constant throughout. This was compared to two alternative setups, designed to reflect (a) a single DSN wind event (Run-1) and (b) two wind events in succession (Run-2). In this way we were able to isolate the effect of a single barrier wind event, and also to gauge the cumulative effect of successive winds events. Both Run-1 and Run-2 were subject to a 4-day wind event beginning at the start of the integration, while in Run-2 a second wind event was imposed at 10 days. All three runs ended after 25 days. The model runs are detailed in Table 3.1.

3.3 Results and Analysis

3.3.1 Initial State

Figure 3.2a shows the sea surface temperature field after the 100-day spin-up period, which was used as the starting point for all subsequent experimental runs, nested within the high-resolution portion of the larger domain. The IC can be seen circulating around the head of the Irminger Basin, with a branch circulating north into the Denmark Strait. The eastern edge of KT appears to represent a boundary in surface water temperature, with warmer water residing to the west and a particularly strong temperature front between KT and the area of shallower topography to the east. The supply of heat along KT towards the KF mouth region is not spatially uniform, with pulses of anomalously warm water ($\Theta > 2.5°C$) interspersed with cooler regions ($\Theta \simeq 2°C$). Surface temperature and salinity generally decreases approaching the coast indicating that the model has captured the EGCC, as was confirmed by taking velocity sections normal to the coastline (not shown).

Temperature and salinity sections along the thalweg of the combined KF/KT system (Figure 3.2b and c) reveal a stark difference in stratification structure between fjord and shelf. In KT, the upper 150 m is well mixed. The warmest waters are found at around 300 m, though stratification is relatively weak in both temperature and salinity. In contrast, the upper 200 m of the water column inside KF is characterised by a sharp vertical salinity gradient and a negative vertical temperature gradient. This warm layer is thickest and warmest in the fjord mouth. As a result of the imposed subglacial discharge and any melting at the KG terminus during the spin-up period, the fjord interior has become strongly salt-stratified in the surface layer, with the pycnocline shallower and sharper than in KT. Cold, dense waters are found isolated below sill depth, both in KF and in the deeper, central region of KT. There is no clear evidence of the four-layer overturning circulation scheme observed by Inall et al. (2014), indicating that, after switching off subglacial discharge, melting alone was unable to sustain such a vertical hydrography structure. The

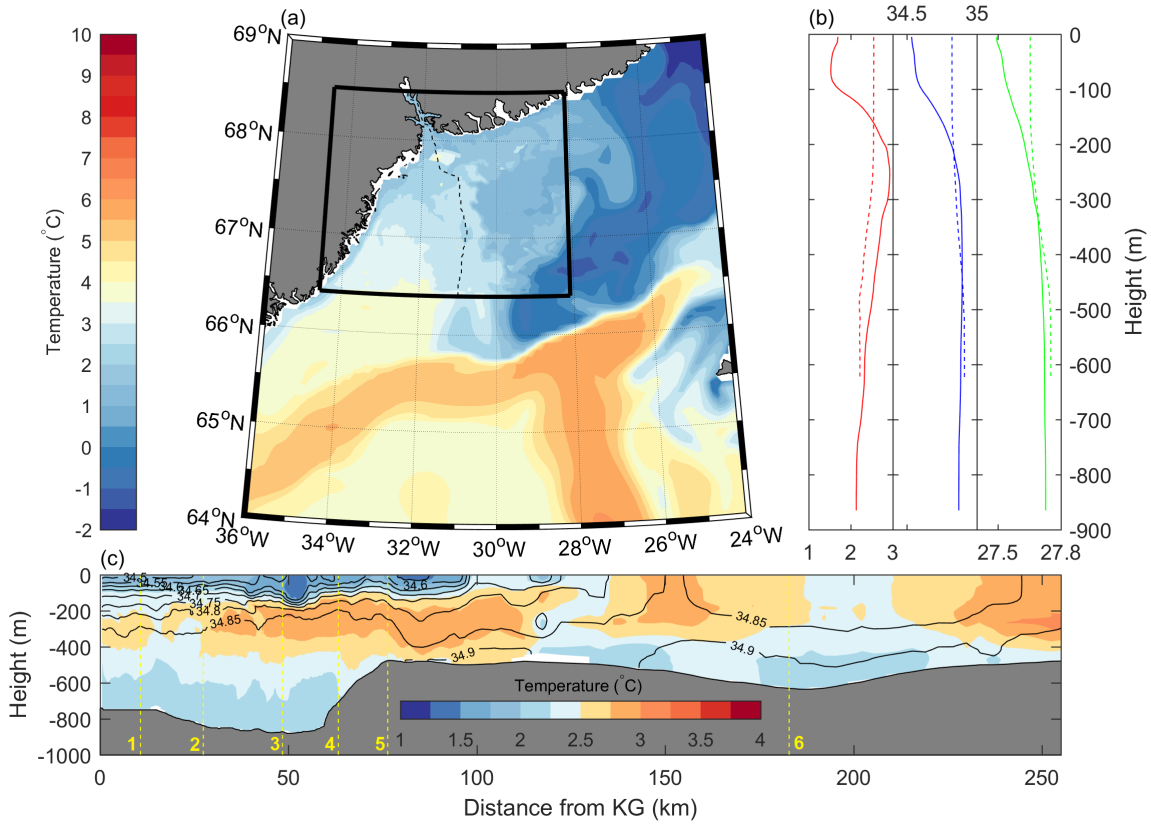

Figure 3.2: State of model after the 100-day spin-up period. Sea surface conservative temperature from the main model, nested within the larger model, is shown in (a), with the thalweg marked by a dashed black line. In (b), vertical profiles in conservative temperature, absolute salinity and σ_θ from the deepest point in KF (Section 3, solid lines) are compared to corresponding profiles taken from the deepest point in KT (Section 6, dashed lines). Conservative temperature and absolute salinity section taken along the thalweg shown in (c), with the locations of the standard cross-sections 1-6 shown in dashed yellow. Note the different temperature scale from that used in (a).

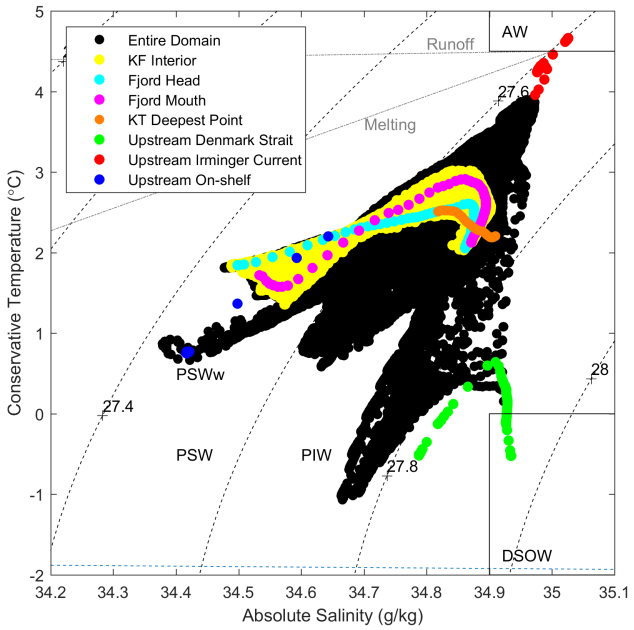

Figure 3.3: State of model after the 100-day spin-up period in T-S space. The data from the fjord interior, as well as two profiles taken in the near the fjord entrance and near the glacier terminus, are highlighted. To indicate the properties of the source waters to the region, single profiles were also taken from the larger domain from the Irminger Current west of Iceland, the Denmark Strait saddle point, and the shelf north of KT.

temperature structure in the mid-fjord is comparable with that observed by Jackson et al. (2014) during winter 2009, where the temperature maximum was often located at 200-300 m. The small depth range observed by Jackson et al. (2014), along with the high variability in thermocline height recorded within that range, make it difficult to validate the model using this data set, but the general structure is consistent.

Viewing the model's water properties in T-S space (Figure 3.3) sheds further light on the hydrographic structure of the model domain. We include profiles, taken from the larger model, in the Denmark Strait, the Irminger Current and on the shelf northeast of the main domain, which we take to represent the source waters to the main model. This helps illustrate how the relative influence of each of these three source waters, the heaviest (DSOW), warmest (AW) and freshest (PW) inflowing waters respectively, dictates the conditions at a given location. In the upper layer of the fjord interior the freshening effect of the plume parametrisation at the head of the fjord is clearly seen, matching the gradient of the mixing line between AW and GMW. This may be considered another water mass source, albeit supplied via glacial modification rather than advection, since the freshest waters towards the head of the fjord lie outside the convex hull of the three source water

Section no.	Run-0	Run-1	Run-2
1	0.03	0.07	0.07
2	0.03	0.06	0.07
3	0.06	0.10	0.11
4	0.14	0.25	0.30
5	0.10	0.17	0.19
6	1.10	1.10	1.23

Table 3.2: Mean exchange (Sv) through each section for each model run.

masses (red, blue and green on Figure 3.3). The along-fjord temperature gradient in the warm layer is highlighted by selecting profiles from the fjord mouth and near the KG terminus. The presence of PW is also greater in the mouth, where we see a straight mixing line running from the temperature maximum towards the PW source, than near KG, where all the water in the upper layer falls between the temperature maximum and the freshest waters on the surface. The surface water in the mouth is slightly warmer than the PW directly below it due to upwards heat transport by the plume dynamics encapsulated in the iceplume package, and subsequent estuarine outflow. Surface waters in KT have similar properties to intermediate depth waters inside KF. PSWw, as found in KF by Inall et al. (2014); Sutherland et al. (2014b), is cooler and less abundant in our model due to the prescribed winter conditions, and without injected freshwater the model does not generate surface waters as fresh and light as those observed in summer. We also note that deepest waters in KT are marginally heavier than those inside the fjord, indicating that a deep water renewal event could occur were deep layer (below sill depth) exchange permitted.

3.3.2 Mean Flow

The normal component of the mean flow (time-averaged over the full 25-day run) through six cross-sections (Figure 3.1) for Run-0 is shown in Figure 3.4. The circulation displays horizontal variability in all sections with inflow (outflow) on the right (left), a behaviour only permissible in broad fjords. We calculated L_R to be ~ 3 km in the mid-fjord (Section 2), firmly placing KF as a broad fjord under the stratification conditions in the model. In KT (Section 6) the outflow is strongly barotropic while the inflow intensifies with depth such that strong currents of up to $20\text{cm}\,\text{s}^{-1}$ sit against the eastern flank. In the mouth of KF (Sections 4 and 5) the lower layer circulation structure matches that of KT, with an inflowing current core residing against the eastern boundary below 200 m. In the KF interior (Sections 1, 2 and 3) we see a strong cross-fjord velocity shear throughout most of the water column, with inflow on the right, with the surface dominated by outflow in the upper- and mid-fjord (Sections 1 and 2).

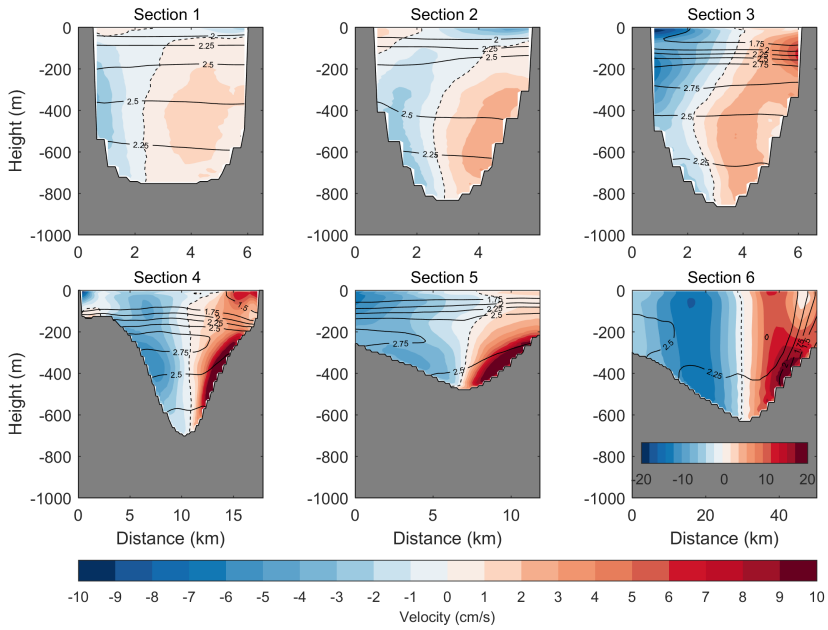

Figure 3.4: Normal component of mean flow through each section for Run-0. Section 6 has a separate velocity scale as current speeds were higher there. Isotherms are denoted by solid black contours.

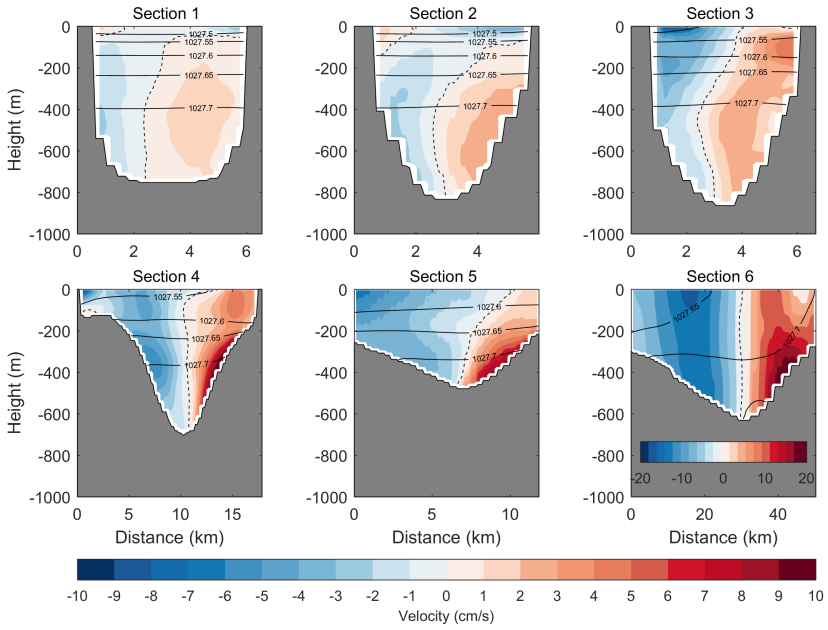

Figure 3.5: Normal component of mean geostrophic flow through each section for Run-0. Velocity profiles were calculated using the thermal wind equation and referenced using sea surface slope. Section 6 has a separate velocity scale as current speeds were higher there. Isopycnals are denoted by solid black contours.

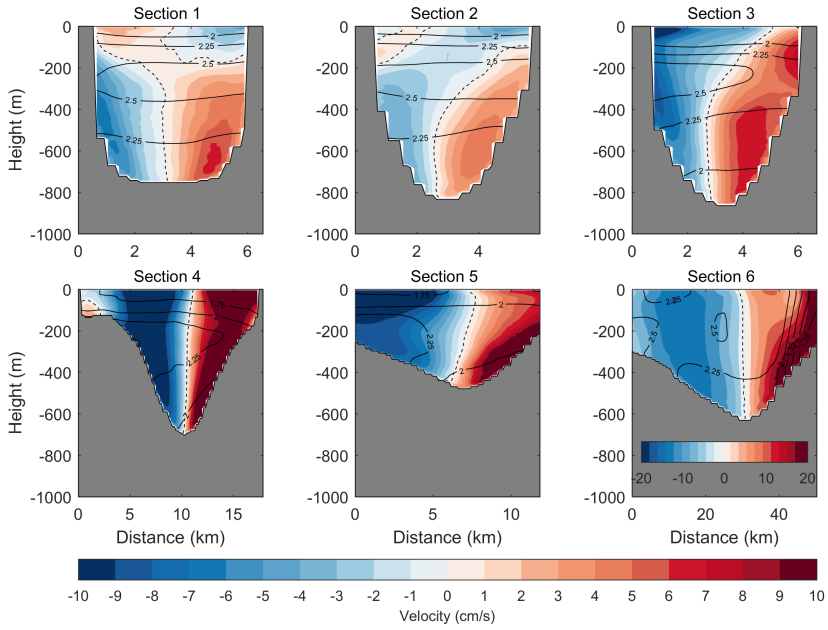

Figure 3.6: Normal component of mean flow through each section for Run-2. Section 6 has a separate velocity scale as current speeds were higher there. Isotherms are denoted by solid black contours.

Corresponding geostrophic velocities for Run-0 are shown in Figure 3.5. The vertical shear structure was obtained for each density profile pair via the thermal wind relation and each velocity profile was then referenced using sea surface slope. These fields show excellent agreement, in circulation strength and structure, with those obtained from dynamical output variables, indicating that the circulation in both KT and KF is typically in geostrophic balance (as is later confirmed via direct evaluation of the momentum terms). The sloping isopycnals in the mouth (Sections 4 and 5) and, in particular, KT (Section 6), indicate that the outflow is driven by a barotropic pressure gradient, and the lower layer inflow by thermal wind.

In Run-2, which was subject to two barrier wind events, the mean circulation was more intense than from Run-0, and with near identical structure (Figure 3.6). The corresponding geostrophic velocities (not shown) are once again in excellent agreement with model section-normal velocities. The Run-1 mean flow (not shown) has similar structure again, and sits between Run-0 and Run-2 in intensity. The action of barrier winds therefore appears to strengthen pre-existing background circulation both in KF and KT. This effect is later shown to by caused by Stokes' drift (Stokes, 1847).

We quantified the exchange through each section by considering the volume flux due to the

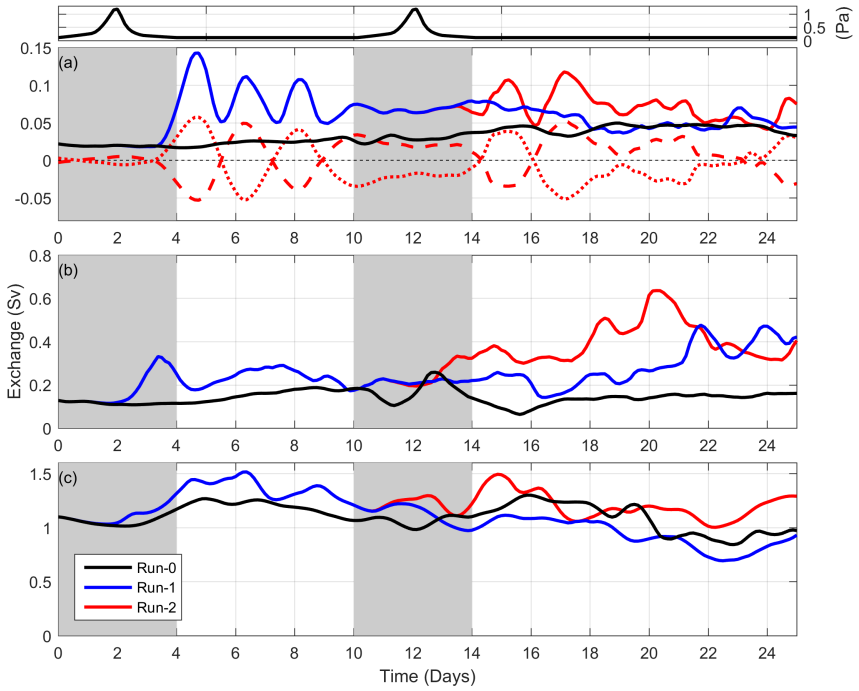

Figure 3.7: Timeseries of exchange through (a) Section 2, (b) Section 4 and (c) Section 6. The grayed-out regions denote the periods during which barrier wind forcing was switched on.

inflow only, which is valid so long as there is no net volume transport. This definition is therefore imprecise in Sections 5 and 6, which are not closed, however it does provide values for the northward transport through KT, the predominant pathway for IC water into the mouth of KF. Exchange was found to increase with barrier wind forcing. For example, the mean exchange through the fjord mouth (Section 4) was 0.14 Sv, 0.25 Sv and 0.30 Sv in Run-0, Run-1 and Run-2 respectively. The mean exchange values for all sections are listed in Table 3.2.

3.3.3 Temporal Variability

Figure 3.7 shows timeseries of the exchange through KT (Section 6), the fjord mouth (Section 4) and the mid-fjord (Section 2) from each of the three simulations. The exchange through KT is relatively steady, at around 1 Sv. Barrier winds are seen to enhance the exchange there but changes are not highly significant compared to the synoptic variability in the control run. The initial barrier wind event in Run-1 caused an approximate trebling of the exchange through the fjord mouth, ramping up and down over around 2 days, before increasing again to around twice the background value. The Run-1 signal reverted back to closely match the Run-0 signal after around 10 days. In the mid-fjord (Figure 3.7a) the

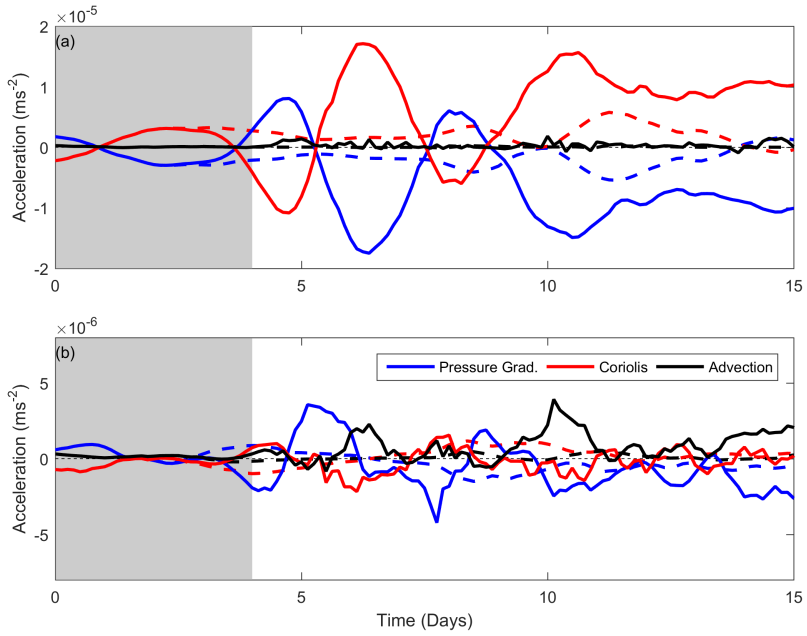

Figure 3.8: Time series of (a) across-fjord and (b) along-fjord components of the pressure gradient, Coriolis and advection terms of the momentum equation taken at the mean inflowing core on Section 2. Dashed lines indicate Run-0 while solid lines indicate Run-1. Note the differing y-axis scaling between the two plots. The grayed-out region denotes the period during which barrier wind forcing was switched on.

signal due to the same barrier wind event was manifested as a sinusoidal signal, with three pronounced peaks reaching around four times the background value before dying away. By splitting the signal into northward transport both above and below 250 m, it is evident that the peaks in exchange correspond to times when upper-layer velocities opposed those in the lower layer, a pattern which alternated in time. After the oscillations finished, the Run-1 exchange signal remained around double the background signal until around day 18, consistent with the intensification of the mean flow with increasing barrier wind activity. The second wind event in Run-2 had a similar initial effect on exchange in both locations, driving a spike in exchange through the mouth followed by a sustained enhanced exchange, while driving an oscillating exchange pattern in the mid-fjord. However, at later times in Run-1 and, to a greater extent, Run-2, the exchange through the fjord entrance (Section 4) was found to greatly exceed the background (Run-0) value (caused, as we later discuss in more detail, by dense shelf waters spilling over the sill and cascading down into the fjord bottom). The oscillating signal reemereged in the mid-fjord (Section 2) in Run-2, but was neither as pronounced or sustained as following the signal due to the initial wind event.

We looked to better understand the oscillating nature of the exchange in the mid-fjord

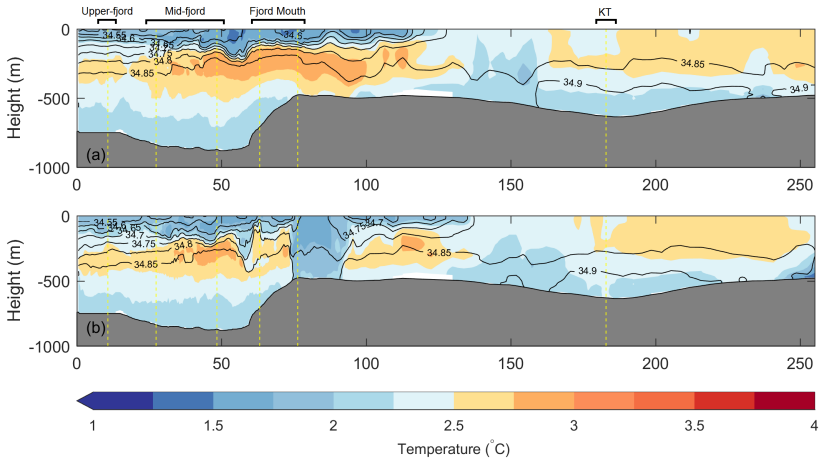

Figure 3.9: Conservative temperature and absolute salinity along the thalweg section in (a) Run-0 and (b) Run-1 taken after 12 days of simulation.

via direct evaluation of the terms in the momentum equations. Figure 3.8 shows time series of the pressure gradient, Coriolis force and advective terms from the core of the mean inflow in the mid-fjord (Section 2) for both Run-0 and Run-1. The viscous term was omitted as it was smaller by more than two orders of magnitude. In Run-0, the lateral pressure gradient (3.8a) demonstrates stochastic variability, fluctuating around the mean value and sometimes changing sign, and is consistently balanced by the Coriolis force, further confirmation that the modelled circulation within KF was geostrophically balanced. The wind event in Run-1 excited a large oscillation in the pressure gradient with period 3.5 days, twice that of the exchange signal. Again, the Coriolis term always opposed to the pressure gradient, even under sign reversal, indicating that this low-frequency oscillation was slow enough that geostrophic balance was maintained. We see a tendency for growth of the lateral pressure gradient (and Coriolis force) superimposed onto the oscillating signal, such that the system does not revert to the Run-0 case after the wind-induced oscillation dies away. This increase is consistent with the stronger mean circulatory flow found in model runs subject to wind forcing. The advective term is small in comparison throughout. We also see an oscillation emerge in the along-fjord pressure gradient after wind forcing (Figure 3.8b) which is around one-quarter the amplitude of the lateral oscillation and a quarter-period out of phase, such that the two components together describe an elliptical trajectory. The along-fjord Coriolis term is also small, as lateral velocities are generally small, and there is less clear symmetry with the pressure gradient term. Advection is of comparable magnitude to the other two terms in the along-fjord component and, from around day 7 onward, appears to be driven by the pressure gradient. This suggests that geostrophically balanced wave motions act to enhance along-fjord advection.

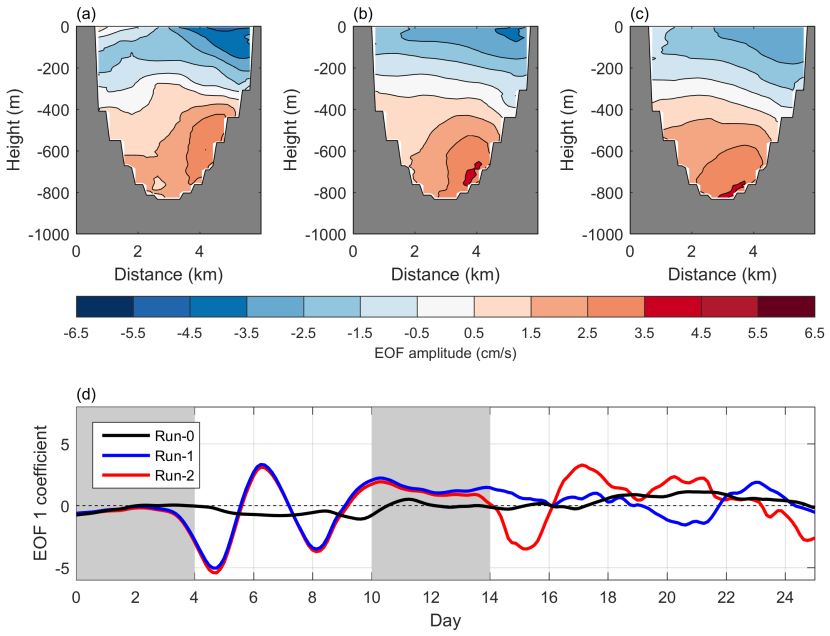

Figure 3.10: EOF-1 at KF Section 2 from (a) Run-0, (b) Run-1 and (c) Run-2, which accounts for 35%, 52% and 59% of the variability respectively. In (d), the coefficient of each is plotted over time, and the grayed-out regions denote the periods during which barrier wind forcing was switched on.

The oscillation of the pressure gradient corresponded with a wave in the halocline (here we used the 34.7 g/kg isohaline as a proxy) with an amplitude of around 70 m at the eastern boundary (30 m at the western boundary) in the mid-fjord (Section 3), dissipating to 40 m at the eastern boundary of the upper-fjord (Section 1). The first peak took 10 hours to propagate from Section 4 to Section 3 (15 km), 15 hrs from Section 3 to Section 2 (21 km), and 15 hrs from Section 2 to Section 1 (17 km) giving propagation speeds of approximately $42\text{cm}\,\text{s}^{-1}$, $39\text{cm}\,\text{s}^{-1}$ and $32\text{cm}\,\text{s}^{-1}$ respectively. Figure 3.9 shows the state of the thalweg section in Run-1 compared to Run-0 after 9 days of simulation. While internal waves are visible in the isohalines in both plots, wave amplitudes are greater in Run-1. Strikingly, in the aftermath of barrier wind forcing, cold, dense waters are found immediately outside KF, forming a sharp temperature and salinity front between the fjord mouth and the fjord interior.

We computed the most significant empirical orthogonal functions (EOFs) of the Section 2 velocity field for each model run (Figure 3.10a-c). EOF-1 accounts for 35%, 52% and 59% of the variance in Run-0, Run-1 and Run-2 respectively. In all cases EOF-1 is dominated by vertical shear with the upper layer velocity opposing that in the lower layer, and appears to reflect the first normal mode (or baroclinic mode) of oscillation. However, some cross-fjord

structure is present in EOF-1, with greater variability against the eastern side than against the western side (where internal wave amplitudes are greater).

We found a strong link between barrier wind forcing and the temporal patterns in the EOF-1 coefficient. Figure 3.10d shows time series of the EOF-1 coefficients for each run. The different model output fields project onto slightly different eigenbases, however the three EOF states appear similar enough that we proceed under the assumption that they are all broadly representative of a first normal mode. When information of the barrier wind event, which took place on the shelf over the first 4 days and peaked on day 2, propagates into the mid-fjord region it sets up an oscillation in the EOF-1 coefficient. Consistent with Figure 3.7a and the response in SF described by Straneo et al. (2010), we initially see inflow in the upper layer and outflow at depth, before the behaviour reverses. Reconstructed EOF-1 velocities peak around 25 $\mathrm{cm\,s^{-1}}$ in the upper layer. The system then oscillates with period 3.5 days, corresponding to the waves in the pycnocline, with extrema in EOF-1 coefficient corresponding to maxima in exchange (Figures 3.7 and 3.10). On day 13 we see the influence of the second barrier wind event on Run-2, manifested once again as an oscillation in the EOF-1 coefficient, this time with marginally lesser amplitude. In each case the excitation dies away around 8-10 days after the initial divergence from the control run, 10-12 days after peak wind stress on the shelf.

As EOFs are purely statistical in nature and have no inherent connection to physical processes, we follow the common approach (e.g. Sutherland and Straneo (2012)) of directly comparing basis EOFs to normal modes, which are calculated from linear profiles in N, the buoyancy frequency. For this comparison to be meaningful requires that the horizontal variability in the EOFs is small in comparison to the vertical variability. While EOF-1 meets this criterion, higher EOFs have a more complex structure with significant spatial variability both vertically and horizontally (Figure 3.11b-d). By horizontally collapsing the velocity field at Section 2 in Run-2 onto a single, time-dependent profile, we proceeded to calculate one-dimensional EOFs and compared them to the time-average of the first two normal modes calculated from the corresponding density profiles. The first EOF profile is consistent with the first normal mode in that we have velocities in the upper layer opposed to those in the lower layer, with a zero crossing at around 300 m depth (Figure 3.11e). This gives confidence that EOF-1 is dynamically meaningful and representative of first-order baroclinic oscillations in KF.

The propagation speed of a first-order internal wave based on the initial density structure at Section 2 is 40 $\mathrm{cm\,s^{-1}}$, highly consistent with the estimates based on time lags between cross-sections. At later times this value does decrease slightly as the stratification is weakened via shear-driven vertical mixing. We note that dynamic modes calculated here are not necessarily fully correct for the type of wave we see since the dynamic mode theory used

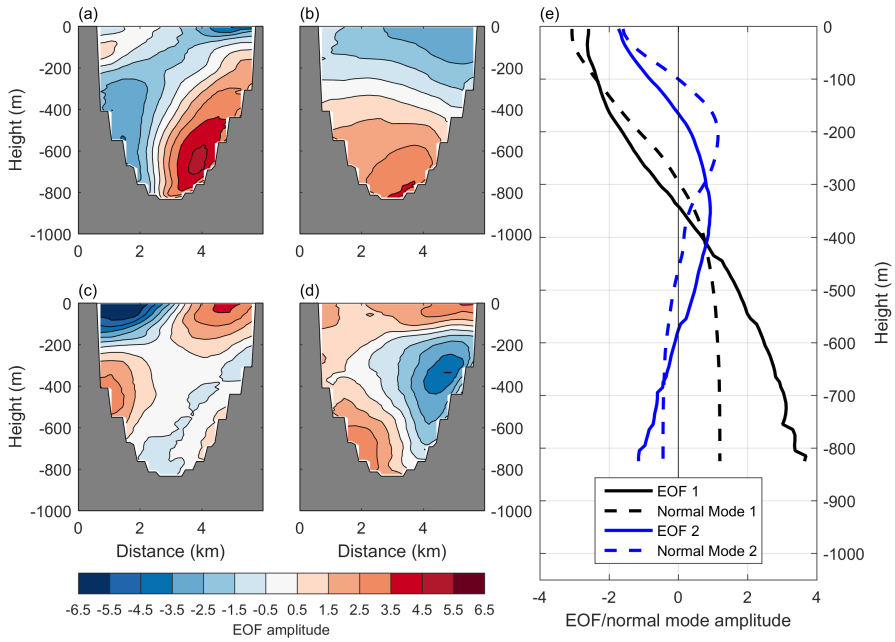

Figure 3.11: (a-d) shows EOF-(0-3) where (EOF-0 is the mean flow) as Section 2 in Run-2, accounting for 59%, 16% and 8% of the variability respectively. (e) shows a comparison between the first two one-dimensional EOFs and the first two normal baroclinic modes, calculated from horizontally collapsed cross-sections in velocity and density.

Section no.	Run-0	Run-1
1	0.0012	0.0018
2	0.008	0.018
3	0.014	0.028
4	0.001	-0.027
5	-0.556	-0.404
6	0.464	1.836

Table 3.3: Mean heat flux (TW) towards KG through each section over the first 12 days of simulation in Run-0 and Run-1.

assumes an infinite flat bottom. Nonetheless, they offer useful insight and, as will be seen in the discussion, have the equivalent dispersion relation to the internal waves observed.

3.3.4 Heat Delivery

The temperature contours in Figure 3.4 show that in Run-0 the warm layer at the head of KF (Section 1 and 2) was generally slightly thicker on the eastern side. This side of the fjord corresponds with the inflowing mean velocities, indicating a positive net heat flux through fjordic sections due to the background circulation. However, at the mouth of KF and in KT (Sections 4, 5 and 6) the outflow is warmer than the inflow, driving a net cooling of the waters outside the KF mouth. We see a similar pattern in Run-2 (Figure 3.6).

Heat flux calculations through closed sections of KF (Section 1-4) were carried out on the native model grid, eliminating interpolation error. They were chosen to be equivalent to those shown in Figure 3.1, but oriented east-west rather than normal to the thalweg. Heat flux through Sections 5 and 6 were calculated using the thalweg-normal sections shown in Figure 3.1. The value of these sections is limited as they are not closed. However, they do give an insight into the heat delivery along KT, which is considered the primary pathway for heat exchange between KF and the open ocean.

In Run-0, the northward heat transport through KT (Section 6) is highly variable on a timescale of around 10 days, with a mean heat flux of 0.47 TW, and maximum and minimum values of 3.1 and -1.3 TW respectively. This is consistent with the results of Koszalka et al. (2013), who find that exchange between ocean and shelf in this region is episodic in nature. Negative mean values were obtained in the fjord mouth area, with -0.27 and -0.01 TW at Sections 5 and 4. The negative Section 4 result is somewhat misleading, however, as the time-integrated value is highly dependent on the integral limits. An increased presence of cold water in the last 2 days of simulation diminished the value greatly, and the mean flux discounting this period was 0.01 TW. The peak value through Section 4 was 0.22 TW. We obtained positive time-averaged heat fluxes in the fjord interior, with $\sim$0.01 TW through Sections 2 and 3 and 0.002 TW through Section 1, indicating that

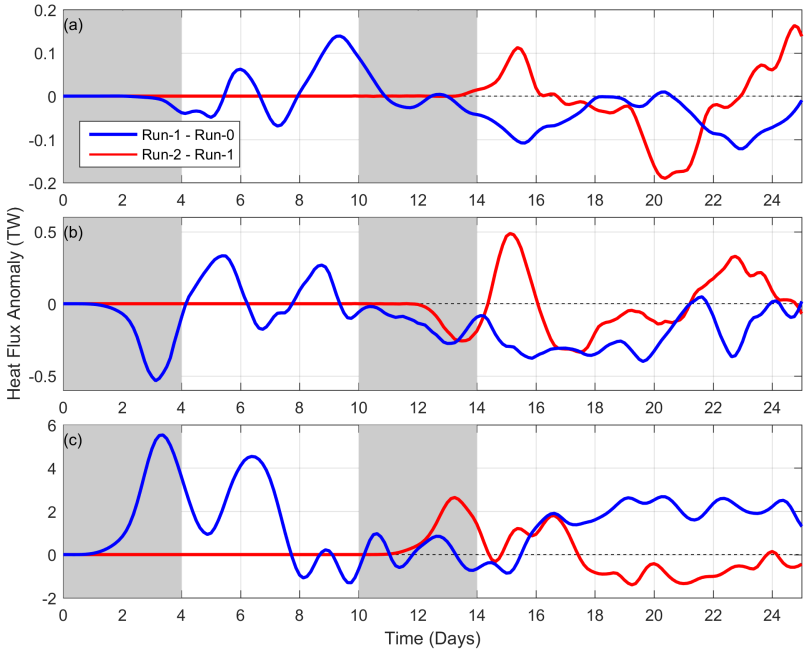

Figure 3.12: Heat flux anomaly towards KG due to each barrier wind event on (a) Section 2, (b) Section 4 and (c) Section 6. The grayed-out regions denote the periods during which barrier wind forcing was switched on.

Section no.	Run-0	Run-1	Run-2
1	0.002	-0.000	-0.002
2	0.022	-0.006	-0.029
3	0.037	-0.050	-0.095
4	0.042	-0.166	-0.217
5	0.132	-0.347	-0.433
6	0.613	1.595	1.784

Table 3.4: Mean heat flux (TW) towards KG through each section during day 10-22 of simulation in Run-0, Run-1 and Run-2.

some heat is delivered towards the KG terminus in the absence of any freshwater input or barrier wind forcing. This was again subject to variability and reversals of sign, with values ranging from -0.06 to 0.10 TW in the mid-fjord (Section 2).

Figure 3.12 shows the heat flux anomaly towards KG in KT (Section 6), the fjord mouth (Section 4) and the mid-fjord (Section 2) attributable to barrier wind forcing. The anomaly due to the first (second) wind event was calculated by subtracting the Run-0 (Run-1) value from the Run-1 (Run-2) value. Barrier wind forcing boosted the northward heat delivery through KT, with two large spikes, each representative of an additional $\sim$5 TW, occurring immediately after the first wind event and two smaller spikes ($\sim$2 TW) after the second. In KF and the fjord mouth (Figure 3.12) we see the expected behaviour after the first wind event, whereby the barrier wind event induced an initially negative heat flux anomaly due to the shoreward velocities in the upper layer. This was followed by an oscillating signal featuring two distinct peaks. Once the oscillatory signal dies, the Run-1 heat flux displays a sustained negative signal at the fjord mouth (Section 4). The mean heat flux towards KG through each section in the first 12 days of Run-0 and Run-1 is shown in Table 3.3. We chose to integrate up to 12 days to ensure that we captured the entire duration of the dynamical response to wind forcing: after this time, the oscillating EOF-1 signal in Run-1 had been damped-out and closely matched that in Run-0 (Figure 3.10d). In cross-sections of the fjord interior (Sections 1-3) the mean value is found to be 47% (0.0006 TW), 132% (0.010 TW) and 97% (0.014 TW) greater than in the control run respectively.

Figure 3.12 also shows the heat flux anomaly attributable to the second barrier wind event in Run-2. In the fjord mouth (Section 4), the initial behaviour is similar to that induced by the first wind event. However, this oscillation dies after a single positive peak, as opposed to the two peaks from the first case. In the mid-fjord (Section 2), the anomaly is positive initially, unlike the anomaly due to the first wind event, reaching 0.1 TW before later dropping to -0.2 TW, with no clear oscillating pattern. The heat flux though Section 4 was found to be positive in the control run (Table 3.4). This signal is negative in Run-1 and Run-2, as seen in Figure 3.12b. This is explained by Figure 3.13 which shows the

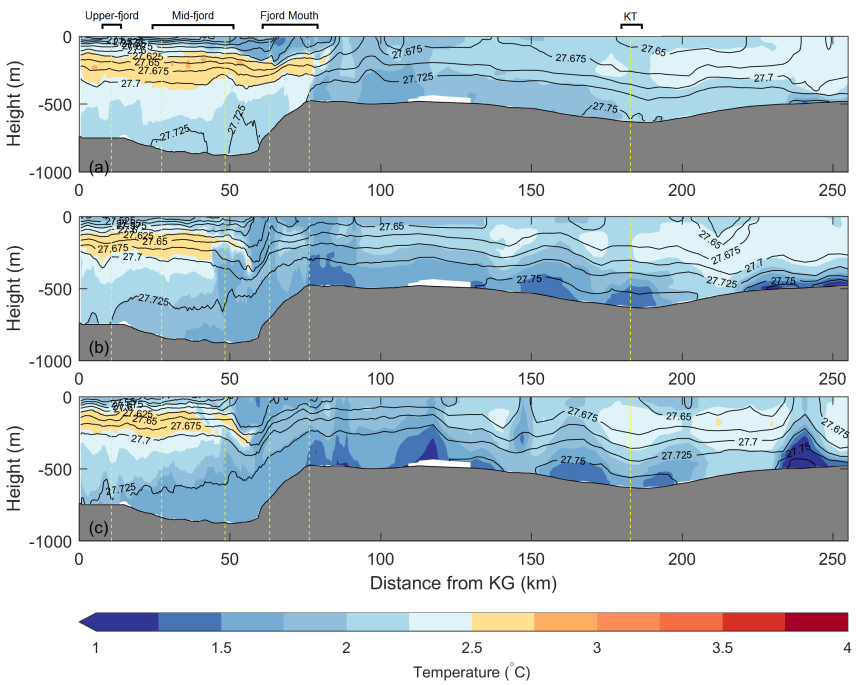

Figure 3.13: Conservative temperature and σ_0 along the thalweg section in (a) Run-0, (b) Run-1 and (c) Run-2 taken after 22 days of simulation.

along-fjord temperature and σ_0 distribution in all simulations after 22 days, 12 days after the onset of the second wind event. The extent of warm water in the fjord mouth, as well as the thickness of the warm layer inside KF, have been greatly diminished by barrier wind forcing. The density contours above the sill have risen up such that the cross-sectional area for dense water ($\sigma_0 > 27.725$) exchange has increased. Cold, dense waters have became abundant in KT in all three model runs, however in Run-2 and, to a lesser extent, Run-1, these waters were able to cross the sill and cascade down into the bottom of KF. The mean heat flux through all sections in Run-2, Run-1 and Run-0 between day 10 and day 22 is shown in Table 3.4. The values in KF and the fjord mouth were greatly diminished in Run-2 compared to Run-1, indicating that a second wind event triggered a greater influx of cold, dense waters to KF. Furthermore, the values were systematically lower in Run-1 than Run-0 during this period, even though the two runs were subject to identical wind stress during this time. This means that the capacity for fjord-shelf exchange remains altered as a consequence of previous wind events long after any dynamical response has dissipated.

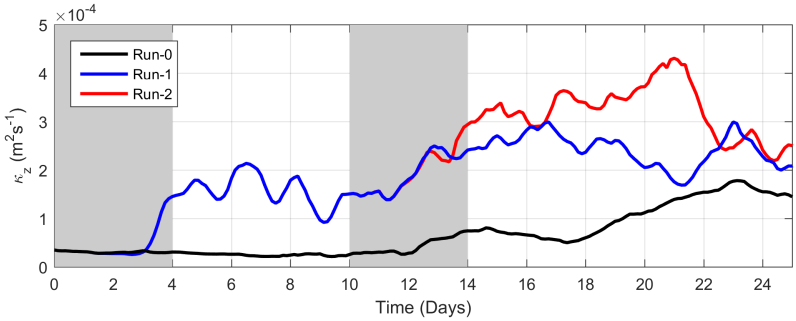

Figure 3.14: Spatially averaged vertical mixing coefficient, κ_z, from the pycnocline in the KF mouth region from the KPP package output for the three simulations. We defined the pycnocline as ($34.7 < S_A < 34.8$), and isolated shear driven mixing between layers by omitting the top and bottom 100 m to eliminate bottom drag and wind shear.

3.3.5 Vertical Mixing

We can better understand the enduring effects of barrier wind forcing on the stratification structure in KF by studying the vertical mixing output from the KPP package. Figure 3.14 shows the spatial mean of the vertical mixing coefficient, κ_z, in the fjord mouth, taken from cells in the halocline ($34.7 < S_A < 34.8$), and which were over 100 m from both the surface and the seabed. The signal is therefore representative of Richardson number dependent, shear driven mixing between layers without the direct effects of the wind or bottom friction. In Run-1, we see an increase in κ_z during the initial barrier wind event in the first 4 days, initially displaying an oscillatory signal similar to that seen in the mid-fjord exchange plot (Figure 3.7a). Enhanced vertical mixing, with respect to Run-0, continues until the end of the simulation, peaking around day 17. In Run-2 we again see the κ_z signal increase again immediately following the second wind event, although any oscillating signal is not as pronounced, peaking on day 21. In Run-1 and Run-2, the strong mixing towards the end of the simulation is likely driven not by internal waves but by dense waters cascading over the sill and spreading along the fjord bottom as a gravity current (as seen in Figure 3.13).

3.4 Discussion

3.4.1 Background Circulation

That the mean flow through each section of the fjord interior displays horizontal shear, with inflow on the right and outflow on the left, is symptomatic a fjord broader than L_R and with dynamics hence influenced by the earth's rotation. Furthermore, the good agreement between the mean flow field and the mean geostrophic flow in the KF interior (Figures 3.4

and 3.5), together with symmetry between the Coriolis and pressure gradient terms in the momentum equation (Figure 3.8), shows that the circulation in this region is typically in geostrophic balance. While previous studies of KF have generally focussed on overturning circulation driven by either freshwater input or shelf exchange (Jackson et al., 2014; Sutherland et al., 2014b; Cowton et al., 2016), the cross-fjord variability in our model is the most striking feature of the mean flow and, in terms of exchange, is more significant than any vertically sheared regime. The study by Cowton et al. (2016), which focussed solely on the fjord interior, did not report significant cross-fjord velocity variability in their modelling study of KF. This suggests that such circulation may be generated as an extension of the geostrophic circulation around the head of KT. The mean flow through Section 5 in Run-0 (Figure 3.4) shows that this connectivity between the KT and KF circulation is strongest in the lower layer. Our model suggests that the fjord mouth is a complex, dynamically three-dimensional region, the circulation and hydrography of which have order-one consequences on the dynamics of the interior. By prescribing horizontally uniform boundary forcing at the fjord mouth, Cowton et al. (2016) may therefore have failed to capture this interaction. As the internal Rossby radius increases with the local stratification, it is also possible that the winter conditions in our model allowed for rotational effects to become significant, while the highly stratified summer conditions used by Cowton et al. (2016) did not. The geostrophically balanced circulation scheme observed in the model requires no external driver, such as wind or freshwater, and will continue to deliver heat up-fjord so long as a positive temperature gradient between the head of the fjord and the entrance is sustained.

Our value of $\sim$0.01 TW through the fjord mouth is two orders of magnitude smaller than the 1 TW value measured there during summer 2009 (Sutherland et al., 2014b), and even our peak value of 0.22 TW was significantly smaller. As we move into the fjord, however, the agreement between our model and the existing literature grows stronger. We obtained a value of 0.01 TW in the mid-fjord, compared with values of 0.19 TW (Sutherland et al., 2014b) and 0.26 TW (Inall et al., 2014) from observation, while the time-averaged heat flux value of 0.0018 TW through Section 1 in Run-0 is in excellent agreement with the value of 0.003 TW given by Sutherland et al. (2014b) for the same location. The fact that synoptic heat flux measurements from summer systematically exceeded our maximum modelled values indicates that the capacity for large heat delivery from the shelf to KF is significantly reduced in winter. However, the good agreement near the fjord head indicates that, in winter, heat is delivered from the mid-fjord to the glacier terminus more efficiently than in summer. We postulate that while the multi-layer circulation seen in summer (Inall et al., 2014; Sutherland et al., 2014b) is efficient at drawing warm shelf waters into the fjord, the heat content in the inflowing layers is depleted due to entrainment via shear driven mixing with the colder outflows both above and below. In contrast, in the horizontally

sheared circulation generated by our model, the inflowing and outflowing current cores reside against opposite sides of the fjord, minimizing the opportunity for entrainment.

3.4.2 Conditions at the Mouth

The fjord mouth was colder after barrier wind forcing and the stratification was weaker (Figure 3.13), better matching the stratification on the shelf than in the fjord interior. It is important to understand the response on the shelf in order to give context to the results from the KF interior.

In Run-2 we found the time-mean inflow on the eastern side of KT and the fjord mouth (Sections 5 and 6) to be strongly barotropic (Figure 3.6) whereas in the control run the inflow intensified towards the bottom, indicating a significant baroclinic contribution (Figure 3.4). This is exactly analogous to findings from West Spitsbergen, where increased barrier wind stress enhanced the AW-influenced barotropic, cross-shelf trough currents (Nilsen et al., 2016). Furthermore these currents were found to follow shallower contours on shelf, as the barotropic pressure gradient has shifted coastward, and the extent to which they penetrated the fjord mouth was hence increased. This is reflected in Figure 3.13, where shelf waters are seen to circulate inside the fjord mouth in Run-1 and Run-2, while in Run-0 the fjordic water properties of KF remain well established in the fjord mouth and extend well beyond.

The time-averaged flow in KT was strengthened with wind forcing (Figure 3.6), and an abundance of cold, dense water was transported along KT and across the fjord mouth. This had the effect of temporarily isolating the waters in KF from those on the shelf and, later, cooling the head of KT (Figure 3.9).

We also found that barrier winds greatly enhance vertical mixing due to increased vertical shear. This effect was strongest in the fjord mouth, where the internal wave field was most energetic. With prescribed subglacial discharge set to zero, melting alone was insufficient to reestablish the stratification so far from the KG terminus after intense mixing. Iceberg melt is a process missing from the model which would help reestablish buoyancy away from the terminus.

The changing conditions at the fjord mouth had profound effects on interactions between fjord and shelf. This is evidenced by the contrasting responses between the three model runs to the presence of dense waters outside the fjord mouth in the latter days of the experiment. Although the transport of cold, dense waters along KT was increased by barrier wind forcing, the region underwent net cooling in all runs. In Run-0, where the stratification inside KF was largely unchanged as no barrier winds were induced, the fjord is resilient to changes on the adjacent shelf and the warm layer remains well established in the mouth (Figure 3.13). The horizontal and vertical extent of this layer is seen to be

reduced after the barrier wind events in Run-1 and Run-2, and the interface between fjord-like stratification and the shelf-like stratification is located further inside KF. This makes the fjord susceptible to deep water renewal, and towards the end of the model run dense shelf waters are seen to circulate north of the sill and flood the fjord bottom. This result suggests an additional mechanism for fjord-shelf exchange, through which barrier wind events intermittently replenish the waters below sill depth. It is likely that in summer, with non-zero subglacial discharge acting to increase stratification within KF, the system would have reverted more quickly back to the control case after barrier wind forcing.

3.4.3 Coastal Trapped Waves

In the absence of both subglacial discharge and runoff, KF was dynamically a two layer system, as reflected by the first baroclinic mode accounting for over half of the variability in velocity in Run-1 and Run-2. This is in contrast to observations from KF in summer where subglacial discharge creates a multi-layer stratification introducing higher order dynamical modes which dominate the variability (Sutherland et al., 2014b). In our model, the dynamical response to barrier wind forcing was broadly consistent with that proposed by Straneo et al. (2010) for SF, in that subinertial waves in the pycnocline drive opposing currents in the upper and lower layers. However, the nature of the intermediary circulation is not fully consistent with previous descriptions based on KF or SF.

We find a subinertial, geostrophically balanced internal wave propagating up-fjord, intensified towards the eastern fjord wall. The pressure gradient term was found to follow an ellipse, with the major axis parallel to the fjord wall. This behaviour is symptomatic of coastal trapped wave (CTW) activity. CTWs are a class of mixed gravity/rotational internal wave of subinertial frequency where the Coriolis force is balanced against a coastal boundary, decaying laterally on an e-folding lengthscale of one Rossby radius (Allen, 1975). The Burger Number, $Bu = ({}^{NH}/_{fL})^2$ where ${}^{H}/_{L}$ is the topographic slope and f is the Coriolis parameter, represents the relative effect of stratification compared to potential vorticity conservation over sloping terrain. The high values obtained in KF ($40 < Bu < 160$, with values increasing moving up-fjord) indicates that stratification dominates over slope effects here, such that the CTWs can be closely approximated as internal Kelvin waves bounded by a vertical wall. This is further evidenced by the close match between the observed phase speed and phase speed predicted by dynamical mode analysis, as Kelvin waves are nondispersive and therefore have a constant phase speed over the wavenumber spectrum. From the wave speed and period we calculated the wavelength of the model-generated CTWs to by $\sim$120 km, greater than the fjord length.

The asymmetry afforded by broad fjords prevents the resonant seiching motions described in SF (Sutherland and Straneo, 2012), as up-fjord and down-fjord CTWs have maximum

amplitudes on opposite sides of the fjord. Due to energy dissipation, the up-fjord wave dominates the variability in comparison to any potential reflected down-fjord wave motion (Figure 3.10), and it is not clear that the signal can propagate around the head of the fjord to produce an outgoing wave. CTWs in fjords may therefore be considered a special class of intermediary circulation where rotational effects give rise to additional physics.

CTWs have previously been observed in West Spitsbergen (Inall et al., 2015), where they were also found to drive large intermediary exchange flows between fjord and shelf. Furthermore, the cross-fjord geostrophic velocity section from KF in Figure 6 of Inall et al. (2014) showed lower layer velocity opposing that in the upper layer, and current intensification towards the coast. This was previously considered a snapshot of a balanced flow, potentially steady over a longer timescale than that of CTWs, which were not examined as a candidate explanation for the observed geostrophic flow structure. In light of the results found here, we reinterpret this signal as more likely a manifestation of CTW activity. Furthermore, Figure 8d of Sutherland et al. (2014b) shows a geostrophic velocity field which is consistent with CTW propagation, calculated based on observations of KF in summer 2009. Model output animations by Carroll et al. (2017) (supporting information) shows CTW behaviour in a broad fjord with idealised topography.

3.4.4 Stokes' Drift

The strengthening of the geostrophically balanced background currents seen in Run-1 and Run-2 may be attributable to Stokes' drift (Stokes, 1847), a process whereby the fluid through which a wave propagates is accelerated in the direction of propagation. CTWs are known to produce this effect (Wunsch, 1973; Weber and Ghaffari, 2014), and this behaviour has been suggested as a residual flow driver in Arctic fjords in West Spitsbergen (Inall et al., 2015). From Equation 11 of Inall et al. (2015) we find a Stokes' drift of $O(1\mathrm{cm\,s^{-1}})$ at Section 2, which is consistent with the mean flow enhancement from the model (Figures 3.4 and 3.6). In Sections 3,4 and 5, the flow is most notably enhanced both above and below the pycnocline, which is broadly consistent with the theoretical vertical structure (Wunsch, 1973; Weber and Ghaffari, 2014). This is hence a candidate mechanism for the observed enhancement of background flow with barrier wind forcing. Unlike intermediary circulation mediated by CTWs, where the time-averaged exchange cancels, Stokes' drift will drive a net enhancement of the background flow. It is reliant on the lateral asymmetry of CTWs and, hence, exclusive to broad fjords. This phenomenon, together with the strengthened barotropic trough current, may help to explain why the exchange in Run-1 remained enhanced after the internal wave activity had ceased. We speculate that the large capacity for CTWs to advect shelf waters into the fjord interior via intermediary circulation may be significant in initiating a two-part process whereby

these waters are then distributed to upper-fjord by the enhanced geostrophic circulation of the fjord interior.

3.4.5 Volume and Heat Exchange

CTW activity was seen to dominate the KF dynamics in the days following a barrier wind event on the shelf and gave rise to enhanced exchange through all sections. In particular, the mean exchange through all sections of the KF mouth and interior (Section 1-5) was approximately doubled in Run-2, which was subject to two wind events in 25 days, compared to Run-0, which was subject to none. Barrier wind events occur with frequency around one per week during the winter months, more frequently than in Run-2, suggesting that KF has the capacity for significant wintertime exchange.

Due to the large variability in heat flux values, the time-integrated values for heat delivered were highly dependent on integral limits. The experiments are therefore not well suited for generating accurate estimates of the wintertime heat flux towards KF. We do, however, gain an insight into a mechanism which likely dominates the wintertime dynamics. Given a positive temperature gradient moving from fjord to shelf, we anticipate the enhanced exchange due to intermediary circulation will increase the heat content of the fjord interior. However, the supply of IC water to the mouth of KF via KT is not steady, with Run-0 heat flux through KF (Section 6) varying on a timescale of over a week. The conditions required at the fjord mouth for large positive heat flux were hence not always in place during wind events. The single barrier wind event in Run-1 was found to enhance the time-integrated heat delivery towards KG through all closed sections of the fjord (Table 3.3). However, the temperature outside the fjord mouth decreased during the simulation, so that the enhanced exchange following the second wind event in Run-2 resulted in negative heat flux towards KG. The temperature of the Irminger Basin and SE Greenland shelf has been anomalously high in the last two decades (Khan et al., 2014), while the PHC3.0 climatology data used to initialise the model reflect the conditions in the latter half of the 20th century. It is therefore quite possible that the use of hydrographic conditions reflecting a more modern shelf sea state would have resulted in larger temperature gradients between fjord and shelf and would hence have yielded larger heat flux values.

When looking to quantify the capacity for barrier winds to drive up-fjord heat flux, we therefore chose to focus on the aftermath of the wind event in Run-1. While the percentage increase was large, the time-averaged heat flux through the mid-fjord following the initial barrier wind event was, at $\sim$0.02 TW, still an order of magnitude smaller than the literature values recorded in summertime observations (Sutherland and Straneo, 2012; Inall et al., 2014) or summertime simulations (Cowton et al., 2015). Near KG (Section 1) the percentage increase was smallest, however the value of 0.0018 TW approximately

matches the value of 0.003 TW measured there by Sutherland et al. (2014b) in summer 2009. This reaffirms that, although heat delivery through the mouth and mid-fjord is significantly smaller in winter than in summer, the heat energy brought into direct contact with KG may be comparable. The doubling of this value in the 12 days after the first barrier wind event would likely have consequences for glacier stability, given the frequency of these events during DJF.

3.4.6 Wider Implications

While increased AW content of West Spitsbergen fjords has been linked to changing along-shelf wind patterns in during the last two decades (Nilsen et al., 2016), the number of barrier wind events per winter season has remained stable over this period (Harden et al., 2011). This indicates that, while barrier winds would have driven exchange between the fjord and the shelf during the period while ocean temperatures increased, they did not trigger the sudden glacier acceleration and retreat observed across SE Greenland in the mid-2000s.

It is likely that CTWs are a major mechanism for exchange in broad fjords in general. The summertime observations of CTWs in SE Greenland (Inall et al., 2014) and West Spitsbergen (Inall et al., 2015) indicate that they are not a winter-specific phenomenon, while the results of Carroll et al. (2017) indicate that they can be generated by sill-tide interactions. While the strong, along-shelf winds characteristic of SE Greenland in winter are a trigger for CTW driven exchange, this is not a necessary condition and we thus anticipate this behaviour in broad fjords elsewhere. For example, Petermann Fjord in northwest Greenland Isfjorden in West Spitsenbergen, and SF all have a rotational influence (Johnson et al., 2011; Nilsen et al., 2016; Sutherland et al., 2014a), and have all been acutely affected by ocean warming. CTWs present a candidate mechanism for the effective transport of heat into these regions.

3.4.7 Evaluation

Though velocity sections from summer also display strong cross-fjord variability (Inall et al., 2014), it is not clear the extent to which these geostrophically balanced currents represent the year-round mean flow. Freshwater input was restricted to ocean-driven melt at the glacier terminus, and hence we do not see the strong buoyancy-driven circulation or complex stratification structure observed in summer field campaigns (Inall et al., 2014; Sutherland et al., 2014b). As winter observations in KF are very limited it is difficult to validate the model, leading to uncertainties in how accurately it recreates typical wintertime conditions. Additional mooring data from the KF interior, particularly during barrier wind

times, would be hugely beneficial for this purpose and for designing future modelling studies of wintertime exchange.

The model presented here was designed to be as simple as possible while capturing the leading-order processes. We therefore omitted some features which could be of significance. For example, icebergs have been identified as a major contributor to the GrIS freshwater flux (Enderlin et al., 2016; Moon et al., 2017), brine release due to sea ice formation during winter is known to exert influence on the stratification within high-latitude fjords (Cottier et al., 2010), and the tides have been found to generate exchange and vertical mixing at the sill in many fjords (Inall and Gillibrand, 2010); all processes we were unable to quantify here.

With processes on the shelf (which dictate conditions at the fjord mouth) varying on timescales of over a week, the 25-day simulations were too short to expose KF to a comprehensive range of external conditions during barrier wind forcing. Furthermore, the climatology data used to initialised the model may not be representative of the modern state of the SE Greenland shelf. The wind fields used to force the model featured a typical barrier wind event focussed on the region of shelf east of KT (Harden et al., 2011). It is likely that a barrier wind event focussed over KT itself would drive a stronger exchange. We are therefore not in a position to claim full knowledge of the processes governing wintertime exchange. A modelling study running for an entire winter season, exposing the system to a range of wind forcing scenarios and capturing the evolution of the fjord-shelf interaction over a range of timescales, would allow us to better evaluate the mean wintertime heat exchange.

3.5 Summary

We have reported here on a numerical model of Kangerdlugssuaq Fjord (KF) and the adjacent shelf to study the physics of fjord-shelf exchange under typical wintertime conditions. We have identified an additional mechanism for along-fjord circulation, whereby geostrophically balanced background currents advect water along the fjord. This was the dominant feature of the mean circulation, and was of the same order as intermediary circulation with regards to heat delivery through the upper-fjord.

Barrier wind forcing had a profound effect on the dynamics in the $\sim$8 days following peak wind stress, provoking a highly energetic intermediary circulation. We find, in accordance with wintertime observations of KF by Jackson et al. (2014), that the barrier wind signal propagates rapidly ($\sim 40\,\mathrm{cm\,s^{-1}}$) from the shelf to the upper-fjord. This was, however, a different flavour of intermediary circulation to that previously discussed for SE Greenland fjords: the barrier wind signal propagated up-fjord as coastal trapped waves (CTWs),

bounded by the eastern side-wall. Under this regime, which likely features in broad fjords in generaly, the incoming and outgoing CTWs are spatially distinct, prohibiting resonant seiching motions and enhancing the geostrophic background circulation, potentially via Stokes' drift.

CTWs were found to be highly effective at increasing heat transport through the fjord mouth and mid-fjord. The values were small in comparison with observations taken during the summer, and had high variability. The average heat flux through the inner part of the fjord was, however, closely comparable with summertime observations, and approximately doubled in the period during which CTWs were active. Hence, barrier winds are likely a significant factor in oceanic heat delivery towards the GrIS at KF and other broad fjords. Although it is unlikely that barrier wind activity was the trigger for the rapid changes to KG in the past two decades, our results suggest that heat delivery through the upper-fjord can be as significant in winter as in summer.

The stratification inside the fjord was found to be different in nature to that of the adjacent shelf, and we identified a transition zone in the fjord mouth 80-100 km from the model's glacier terminus. This adds a subtlety to the notion of waves in the pycnocline propagating from shelf to fjord, as the pycnocline on the shelf does not necessarily coincide in depth, strength or nature with that in the melt water-freshened KF. As well as driving CTW activity, barrier wind events were found to weaken the stratification within the fjord mouth resulting in a northward shift in the interface between the two stratification types. This was due to a combination of enhanced vertical mixing in the fjord mouth and strengthening of barotropic shelf currents in KT. Shelf waters were subsequently able to circulate more easily in the fjord mouth after barrier wind forcing, and cold, dense shelf waters were able to cascade over the sill into the bottom of KF in the final days of Run-1 and Run-2. In contrast, in the control run the fjord-like stratification remained well established in the fjord mouth and above the sill, isolating the dense waters in the fjord from those on shelf.

We operated under the assumption that runoff and subglacial discharge are negligible in winter, however this is hard to verify due to the dearth of wintertime observations. Regardless, we found that subglacial discharge is not required in order for the background circulation to deliver heat towards KG.

Chapter 4

Wintertime Fjord-Shelf Interaction in Kangerdlugssuaq Fjord, Southeast Greenland

4.1 Introduction

Recent reduction in the Greenland Ice Sheet (GrIS) mass balance has been most profound near the edge, indicative of ocean triggered melting (Rignot and Kanagaratnam, 2006; Nick et al., 2009). Coastal water temperature has increased contemporaneously (Straneo and Heimbach, 2013; Khan et al., 2014), however direct contact between the ocean and the GrIS is limited to glacier termini which are typically located within Greenland's fjords. A deep understanding of the exchange flows between these fjords and the continental shelf is therefore critical for quantifying the ocean's impact on the GrIS.

One of the most acutely affected glaciers in the previous two decades is Kangerdlugssuaq Glacier (KG), which terminates in Kangerdlugssuaq Fjord (KF), and is one of the major outlet glaciers of southeast Greenland. KG destabilised in 2005, when the rate of discharge suddenly doubled (Bevan et al., 2012), and has been slowing gradually since (Khan et al., 2014). KF is around 80 km long and 6 km wide with a maximum depth of around 900 m and a sill depth of around 480 m. At the mouth, where it widens to around 20 km, the fjord meets the north end of Kangerdlugssuaq Trough (KT), a 650 m deep cross shelf channel (Figure 2.1). KT is a known pathway for ocean waters from the Irminger Sea (Gelderloos et al., 2017), and intersects the shelf break at its southern end. Here, Atlantic Water (AW, $\Theta \sim 4.5 - 6.5°\mathrm{C}$, $S_A \sim 34.9 - 35.2$) flows from east to west in a branch of the North Atlantic Current known as the Irminger Current (IC). A second, seasonal pathway for IC water towards KF is north through the Denmark Strait and across the

shelf, leading to a warmer AW layer in winter than in summer (Gelderloos et al., 2017). South of the Denmark Strait, the IC is joined by the East Greenland Current (EGC), which transports Polar Water (PW, $\Theta < 0°C$, $\sigma_\theta < 27.70$) from the Arctic Ocean. Alongside the EGC, the East Greenland Coastal Current (EGCC) transports PW southwards close to the coastline. Dense bottom water, termed Denmark Strait Overflow Water (DSOW, $\Theta < 0°C$, $34.9 < S_A < 35.2$, $\sigma_\theta \geq 27.8$), also enters the region here, released over the Denmark Strait sill in periodic boluses (Koszalka et al., 2013).

Due to seasonal sea ice cover, observations of KF hydrography and circulation are biased towards the summer months, when freshwater runoff is strongest, and there is hence a larger literature on the buoyancy-driven circulation in Greenland fjords (Sciascia et al., 2013; Cowton et al., 2015; Carroll et al., 2016). In winter, when runoff is at a minimum, other factors likely play a primary role in driving circulation. Results from Sermilik Fjord (SF) (Straneo et al., 2010; Jackson et al., 2014; Sutherland et al., 2014b), a similarly sized neighbour to KF, indicate that intermediary circulation, a rapid baroclinic exchange regime triggered by along-shelf (with shore to the right) barrier winds, is a significant driver of fjord-shelf exchange. Enhanced wind stress drives coastward velocities in the Ekman layer resulting in downwelling of the pycnocline, followed by subsequent upwelling once the wind relaxes. Baroclinic exchange flows are generated as the displacement of the pycnocline propagates in-fjord as a subinertial internal wave (Chapter 3). As barrier wind events occur predominantly in the winter months (Harden et al., 2011), the capacity for this mechanism to draw warm ocean waters into contact with glacier termini remains uncertain. Modelling studies of KF (Cowton et al., 2016) have found that, while intermediary circulation provokes an energetic response, heat delivery to the upper fjord is not significant in comparison with values recorded during summer field campaigns (Inall et al., 2014; Sutherland et al., 2014b).

Two-dimensional overturning regimes, driven by either runoff or shelf exchange, have been the main focus in previous studies of circulation in KF and SF. However, the recent modelling study in Chapter 3 found that horizontally sheared, geostrophically balanced flows dominate the mean wintertime circulation in KF and facilitate exchange, with the inflowing (outflowing) currents residing against the right-hand (left-hand) boundary (looking into the fjord). Furthermore, the subinertial internal waves which drive intermediary circulation were coastally trapped waves (CTWs), which intensify towards the eastern sidewall while propagating up-fjord. The steep topography and high stratification dominated over rotational effects, and the waves could be approximated as nondispersive Kelvin waves propagating at the speed of a mode-1 internal wave. Such cross-fjord variability is only prominent in fjords wider than the internal Rossby radius of deformation, L_R, which summer campaigns have estimated to be around 8 km in southeast Greenland (Inall et al., 2014; Sutherland et al., 2014b). KF is approximately 6 km across, and L_R, which is linear func-

tion of the local stratification, may decrease under winter conditions. The potential for a three-dimensional flow field inside KF introduces complexity to the current understanding, and the implications for fjord-shelf heat exchange are not fully understood.

As well as inducing a dynamical response, barrier winds have been found to make enduring changes to the conditions in the fjord mouth with considerable implications for subsequent exchange. In Chapter 3 it was shown, using an idealised modelling study into barrier wind forcing of the KF/KT system under winter climatological conditions, that simulations exposed to wind events exhibited greatly enhanced vertical mixing in the fjord mouth due to subinertial internal wave activity. Transport in KT was also enhanced by barrier wind forcing, and the extent to which cyclonic circulation in KT penetrated the fjord mouth was increased. Together these factors acted to weaken the stratification in the fjord mouth and introduce a more shelf-like water column structure there, an artifact which remained after the dynamical response to wind forcing (i.e. internal wave activity) had dissipated. At a later time, dense bottom waters circulating in KT were able to breach the KF sill and cause a deep water renewal event in the fjord. In model runs where prevailing winds were held constant (without barrier wind events), the mouth, like the KF interior, remained strongly stratified due to the freshening influence of the glacier front, and was resilient to deep-layer exchange with KT.

In this study, we use an adapted version of the model presented in Chapter 3 to study the circulation and exchange in KF during December, January and February (DJF) of 2007-08. While Chapter 3 looked to isolate the effect of barrier wind events against a backdrop of winter climatological conditions through the use of a control run, here we look to place their influence in the context of a realistic reconstruction of winter 2007-08. We focus primarily on processes in the fjord mouth, with the aim of definitively answering the question "Is there potential for significant wintertime heat exchange between shelf and fjord?". The model is equipped with a parameterisation of the KG glacier front (a heat sink and freshwater source) which generates output variables for glacial melt rates (Cowton et al., 2015). We therefore look for correlations between melt rates and various potential drivers of circulation, particularly wind forcing on the shelf.

4.2 Methods

The model used was the MIT general circulation model (MITgcm, Marshall et al., 1997). Integration was performed by the UK National Supercomputing Service, ARCHER. The model grid and bathymetry was constructed exactly as described in Chapter 3, and so is not repeated here. Initial and boundary conditions were generated using output from the model presented in Magaldi and Haine (2015), which was used to simulate the wider Irminger Sea

region for one year beginning 1st June 2007. The availability of this high-resolution forcing data was our motivation for selecting that particular winter for hindcasting. Wind and air-sea heat flux data were obtained from ERA-Interim daily reanalysis products (Dee et al., 2011). Wind stress fields were calculated using the formula from Large and Pond (1981), which were then modified to reflect local sea ice cover, as described in Chapter 3, using temporally varying sea ice concentration data obtained from the National Snow and Ice Data Centre (NSIDC). The MITgcm iceplume package (Cowton et al., 2015) was employed to incorporate the dynamical and thermodynamical effects of ice-sea interaction at the KG terminus. The package facilitates prescribed subglacial runoff, calculates local melting as a function of the temperature of the adjacent grid cells, and analytically solves the plume equations from Jenkins (2011). The plume parameterisation eliminates the necessity to run the model in non-hydrostatic mode by distributing resultant water masses at the level of neutral buoyancy. We employed the κ-Profile parameterisation (KPP), introduced by Large et al. (1994), which calculates the vertical mixing coefficient as a function of the local gradient Richardson number in the ocean interior and as a function of the bulk Richardson number in the mixed layer.

As the model by Magaldi and Haine (2015) was not of sufficient resolution to include KF, the initial conditions within the fjord were horizontally extrapolated from the shelf. A 100-day spin-up period was then carried out, with some runoff ($100\mathrm{m}^3\,\mathrm{s}^{-1}$) prescribed at the KG grounding line during the initial 60 days in order to allow an overturning circulation to develop within the fjord. Wind and boundary forcing were held constant at December 1st values during this period. The model was then integrated forwards using dynamic forcing fields for 91 days, the duration of DJF 2007-08, with a timestep of 5 seconds.

Harden et al. (2011) define a barrier wind 'event' as wind blowing from the northeasterly quadrant, exceeding $20\mathrm{m\,s}^{-1}$, and being distinct in time from other such events by 24 h or more. According to this definition, nine barrier wind events occurred on the shelf outside KF in DJF 2007-08, and their occurrences are shown in Figure 4.1a alongside northeasterly component of wind speed. The corresponding wind stress, which is usually quadratic in wind speed but becomes cubic when the wind exceeds $11\mathrm{m\,s}^{-1}$ (Large and Pond, 1981), is show in Figure 4.1b. Barrier wind events occurred less frequently during DJF 2007-08 than is typical during DJF, with the number ranging from 7 to 20 during 1989-2008 (Harden et al., 2011). Events were generally clustered in time, with four events taking place in early December (hereafter cluster A), two around the start of January (cluster B), two towards the end of January (cluster C), and one in mid-February (cluster D). Two of the wind events, the first in December and first in January, coincided with prolonged periods of strong northeasterly wind stress, and were hence characteristically different to the shorter peaks seen at other times. Both air and sub-surface water temperatures

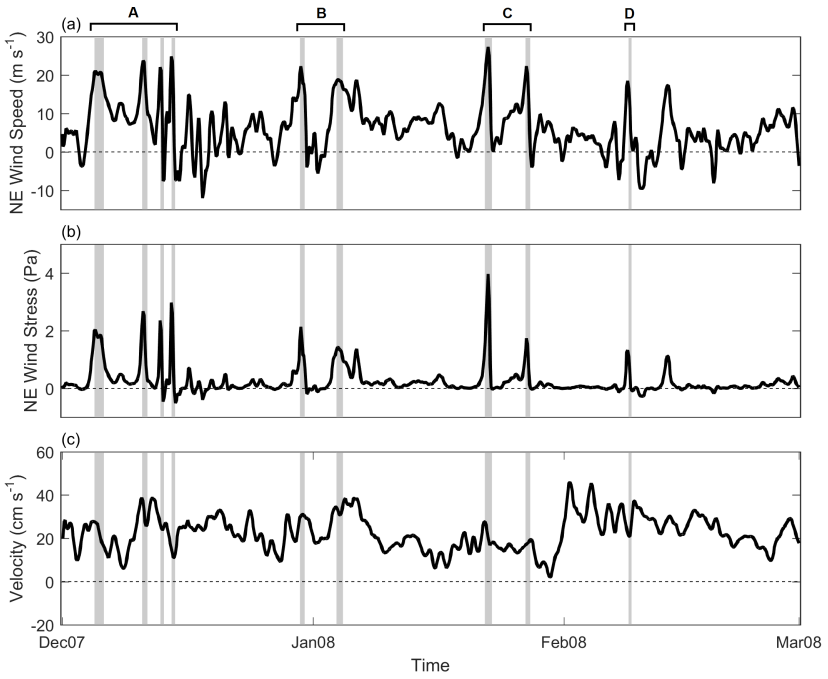

Figure 4.1: (a) Northeasterly component of wind speed (i.e. the component directed SW) over the deepest point in KT (centre of Section 6). (b) Northeasterly component of wind stress over the deepest point in KT. (c) Meridional velocity at the southern boundary taken from the core of the inflow into KT, defined as the region where the mean flow exceeded $20\text{cm}\,\text{s}^{-1}$. The grayed-out regions denote periods considered barrier wind events, with wind event clusters labelled at the top of the figure.

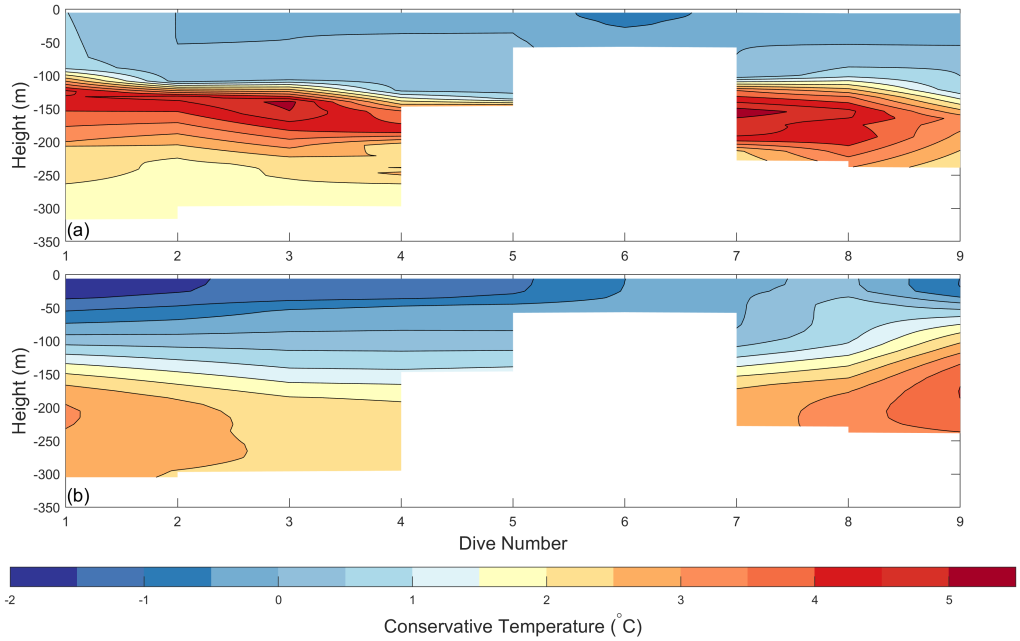

Figure 4.2: In situ temperature (a) along the path of an instrumented seal on 4-5th January 2005 and (b) from the model temperature field interpolated onto the same path, but for 4-5th January 2008.

were anomalously high in comparison with the 1981-2012 mean, though consistent with other years since 2000 (Khan et al., 2014). Meridional velocity into KT at the southern boundary is also an important external driver of dynamical variability, and is shown in Figure 4.1c. Barrier wind events regularly coincided with enhanced inflow into the model domain, likely due to the intensification of barotropic currents on the shelf by along-shore wind stress as described in Nilsen et al. (2016). Notable exceptions arise in late January and early February, however, when enhanced inflow did not coincide with wind events, indicating that other factors also influence inflow variability.

4.3 Results and Analysis

We first give some validation of model realism, by way of comparison with in situ measurements from an instrumented seal (Treasure et al., 2017), taken within the model domain during the 4-5th January 2005. The seal performed 9 dives near the southern boundary of the model domain, sometimes exceeding 300 m depth, giving temperature measurements along it's path. Figure 4.2 shows the resulting temperature field alongside the corresponding model temperature field for 4-5th January 2008, interpolated onto the seal's path. Overall, the model shows generally good agreement with the observations in terms

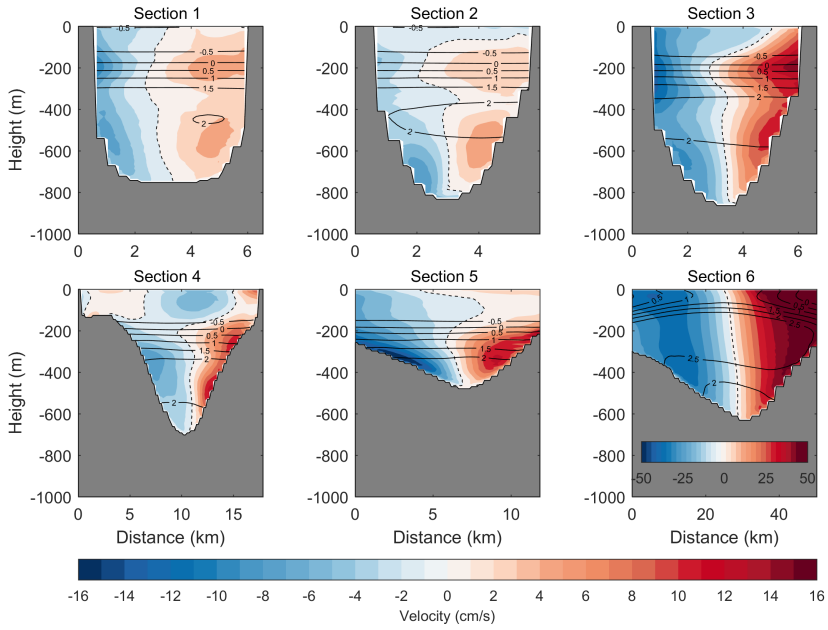

Figure 4.3: Mean flow normal to standard cross sections. Black contours denote conservative temperature. Note the different velocity scale for Section 6.

of stratification structure, thermocline height, and the temperature in the upper and lower layers, giving confidence that the model successfully captures the leading-order physics. The subsurface temperature maximum is greater in the observations, and the thermocline is slightly sharper, while the surface waters (top 50 m) are colder in the model. This may be due to interannual variability as opposed to model inaccuracy.

The mean flow through six cross-sections (Figure 3.1) of the combined KF/KT system is shown in Figure 4.3, with mean conservative temperature contours overlaid. Section locations are shown in Figure 3.1. In KT (Section 6) we see a strongly barotropic flow regime, with inflow (outflow) of around 40cm s^{-1} on the right (left) flank looking towards the fjord. In the fjord mouth (Sections 4 and 5) the mean flow is weaker and intensifies with depth, with current cores of around 15cm s^{-1} concentrated against side walls at around 400 m depth. Moving in-fjord the currents becomes weaker still, while retaining the pattern of inflow on the right and outflow on the left. Temperature contours reveal a strong thermocline (which coincides with the pycnocline, not shown) within KF at a mean depth of around 200 m. Absolute geostrophic velocities (not shown), calculated using the mean sea surface height (SSH) and density fields at each section, are in close agreement with the modelled fields, indicating that the circulation is typically in geostrophic balance to a close approximation.

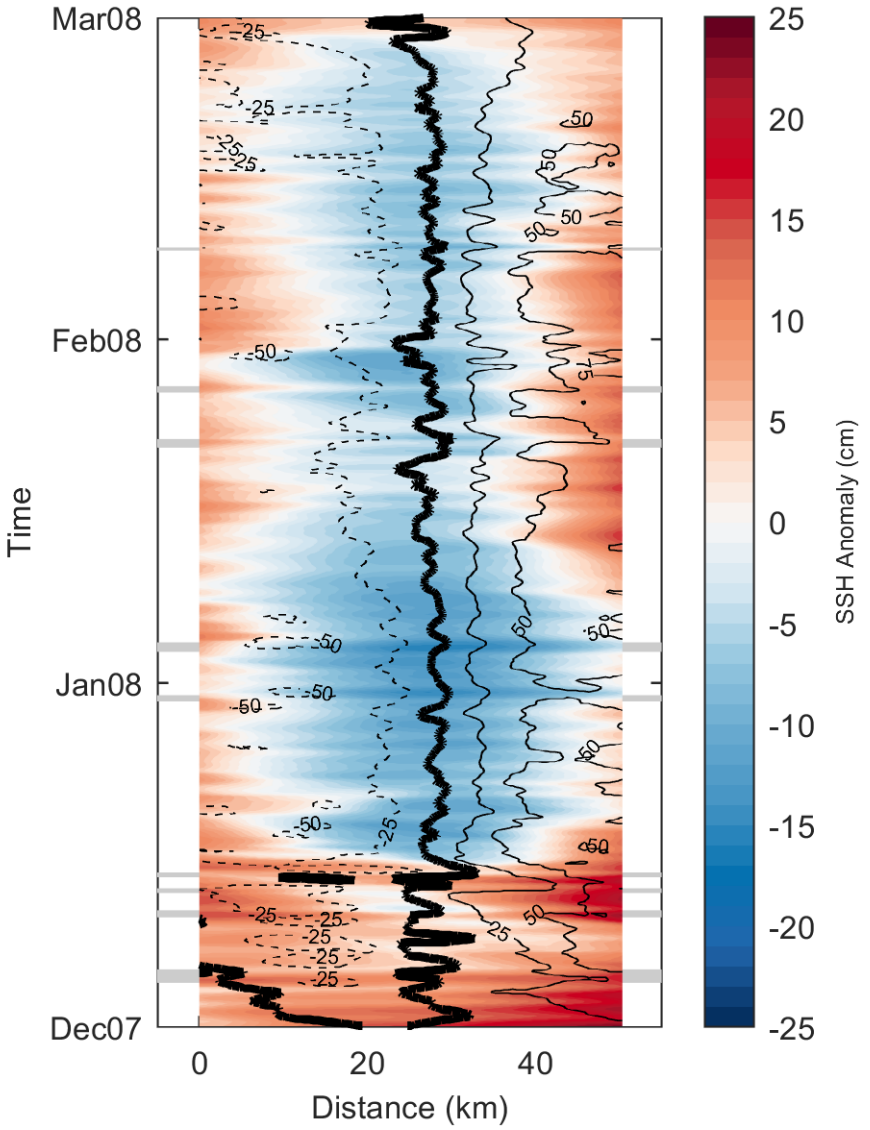

Figure 4.4: Hovmöller diagram showing the SSH anomaly on Section 6 over the course of the simulation. Solid (dashed) black lines denote positive (negative) DAC contours, while the bold black lines denotes zero DAC. The bars down either side denote barrier wind activity.

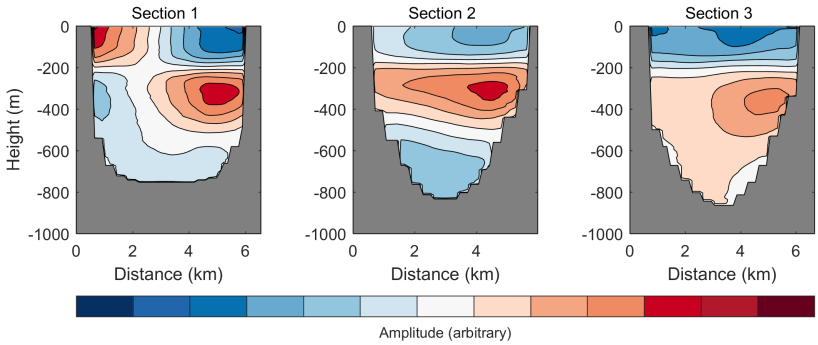

Figure 4.5: EOF 1 on Sections 1 and 3, and EOF 2 at Section 2, accounting for 30%, 29% and 46% of the variability on Sections 1-3 respectively.

Motivated by the barotropic nature of the flow in KT, we investigated the sea surface height (SSH) anomaly on Section 6, looking specifically for correspondence between wind forcing and shoreward transport. Figure 4.4 shows the time evolution of SSH alongside the depth-averaged current (DAC) normal to the section. The surface is generally depressed in the middle of the section and elevated at either side. Barrier winds regularly correspond to a deepening of the central depression, and appear to temporarily hinder the northward DAC on the eastern side while enhancing the the southward DACs in the western side.

From density profiles within the fjord, we calculated the linear, mode-one internal wave speed to be 1.1m s^{-1}. We then used empirical orthogonal function (EOF) analysis to isolate the statistically dominant modes of variability in the velocity field at each section of the KF interior (Sections 1, 2 and 3). Specifically, we note EOFs featuring a nodal contour corresponding to the pycnocline at 200 m. This pattern was seen in EOF 1 on Sections 1 and 3, accounting for 31% and 49% of the variance at their respective locations (Figure 4.5). On Section 2, this class of variability projected onto the second EOF which accounted for 30% of the total variance. In each of these fields, velocities above the pycnocline opposed those below, with strong vertical shear occurring at around 200 m depth. This pattern of vertical variability is most intense adjacent to the eastern sidewall of the fjord and weakens toward the fjord interior. On Sections 2 and 3 this trend continues to the western side of the fjord, while on Section 1 the pattern reverses west of the fjord center line and intensifies again towards the western sidewall. The first EOF on Section 2 (not shown) accounted for 37% of the variability and was similar in structure through more weakly sheared, with a nodal contour at around 350 m.

Figure 4.6 shows a time series of horizontal velocity, (u, v) where u is the across-fjord component and v is the along-fjord component, taken from the Section 2 inflowing current core, defined to be the location of the greatest positive speed in Figure 4.3. Velocities

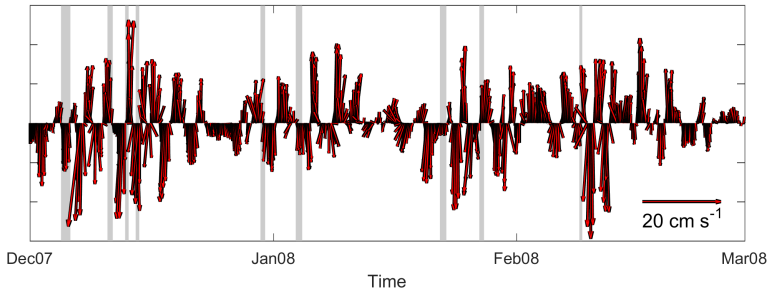

Figure 4.6: Horizontal velocity time series at the deep layer inflowing current core of Section 2. The y-axis represents along-fjord velocity and the x-axis shows across-fjord velocity. The gray bars denote barrier wind events on the shelf.

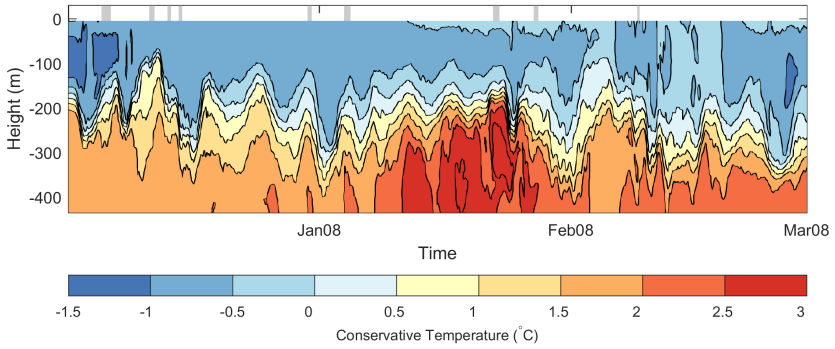

Figure 4.7: Temperature profile time series near the eastern end of Section 2. The gray bars at the surface denote barrier wind events on the shelf.

are largely directed along-fjord, regularly alternating in sign. Cross-fjord velocities are maximal during these transitions, but are smaller by an order of magnitude. The largest along-fjord velocities, along with the most frequent sign changes, generally occur in the days immediately following barrier wind event clusters on the shelf.

Figure 4.7 shows a time series of the model-generated temperature profile 500m from the eastern boundary of Section 2. Quasi-periodic oscillations in the height of the thermocline persist throughout the simulation, although the shape, amplitude and frequency of the waveforms is highly variable. Furthermore, the thickness of the thermocline (defined as $-0.5 < \Theta < 1.5°\text{C}$) changes during the simulation, increasing from an initial value of around 50 m to reach almost 200 m, with a subsequent decrease coincident with increasing lower-layer temperature.

Wavelet analysis was used to decompose the velocity variability in frequency space. Similar to Fourier analysis, this method has the added advantage that the amplitude at each basis frequency may vary temporally, allowing a spectral perspective on the model's response to either stochastic or externally forced variability on the shelf. We performed the analysis on

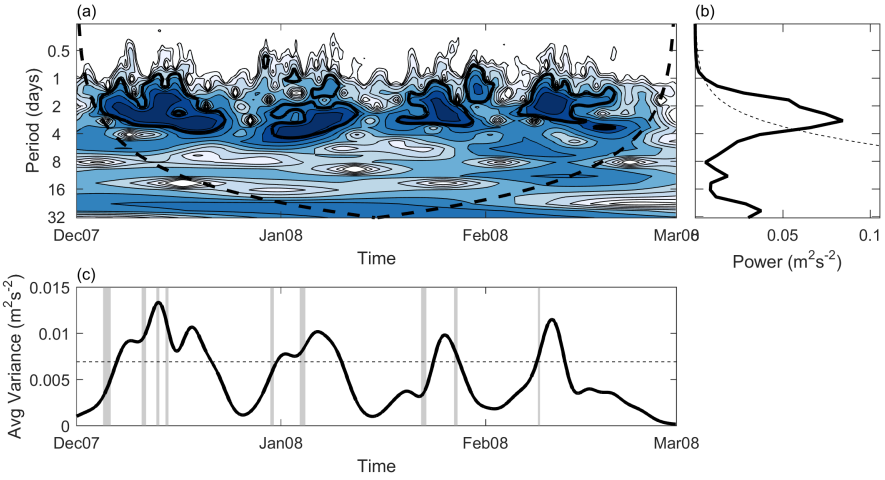

Figure 4.8: (a) The local wavelet power spectrum from velocity variability at the Section 2 inflowing current core. Thick black contours enclose regions of 95% confidence or greater while the region below the dashed line is the cone of influence, where we expect edge effects to become important; (b) the Fourier power spectrum, where the dashed line represents the 95% confidence level; (c) Frequency-averaged wavelet power, with the dashed line representing the 95% confidence level. The grayed-out regions denote periods considered barrier wind events.

the along-fjord component of the Section 2 inflowing current core (Figure 4.3), using a Morlet wavelet basis function (Figure 4.8; the different basis options are detailed in Torrence and Compo (1998) along with a comprehensive description of the procedure). The most significant harmonic variability occurs with period 2-4 days, and there is a strong coincidence between barrier wind activity and excitation of this period band. The frequency-averaged wavelet power exceeds the 95% confidence level on 4 occasions (Figure 4.8c), with each occasion corresponding to a barrier wind event cluster. Harmonic variability also occurs with period $\sim$ 25 days, which is broadly consistent with the interval between wind event clusters. However this period lies largely within the cone of influence (Figure 4.8a) and does not exceed the 95% confidence interval (Figure 4.8b).

Defining exchange as

$$Q = \frac{1}{2} \iint \mid v\,(x, z) \mid dxdz \tag{4.1}$$

where x and y are the respective across- and along-fjord coordinates, we calculated time series of the exchange through each cross-section, shown in Figure 4.9. In the fjord mouth (Sections 4 and 5) barrier wind events are commonly followed by spikes in exchange, particularly following the first wind event of each cluster. The exchange through KT (Section 6) appears more robust to variability in wind patterns over short time scales.

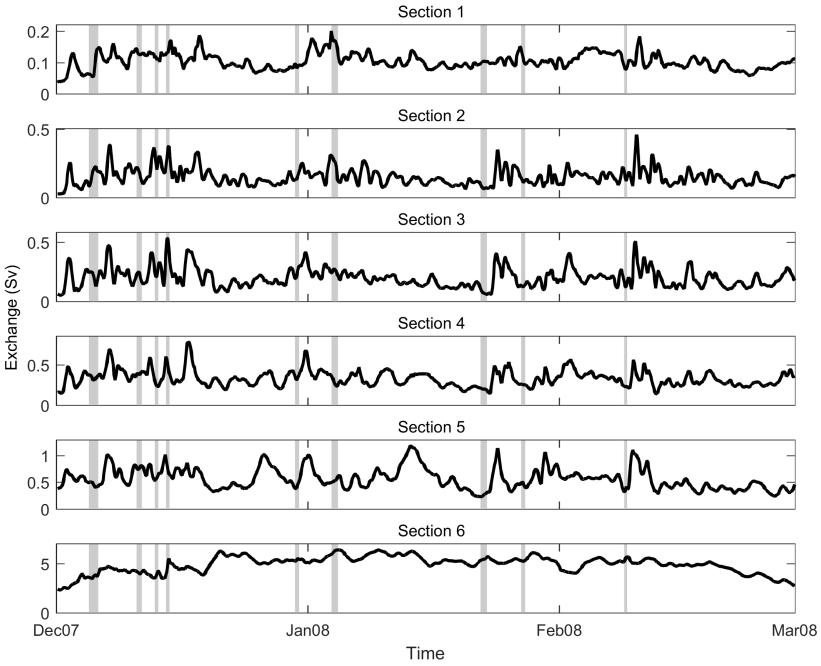

Figure 4.9: Volume exchange through each of the standard cross sections of the KF/KT system.

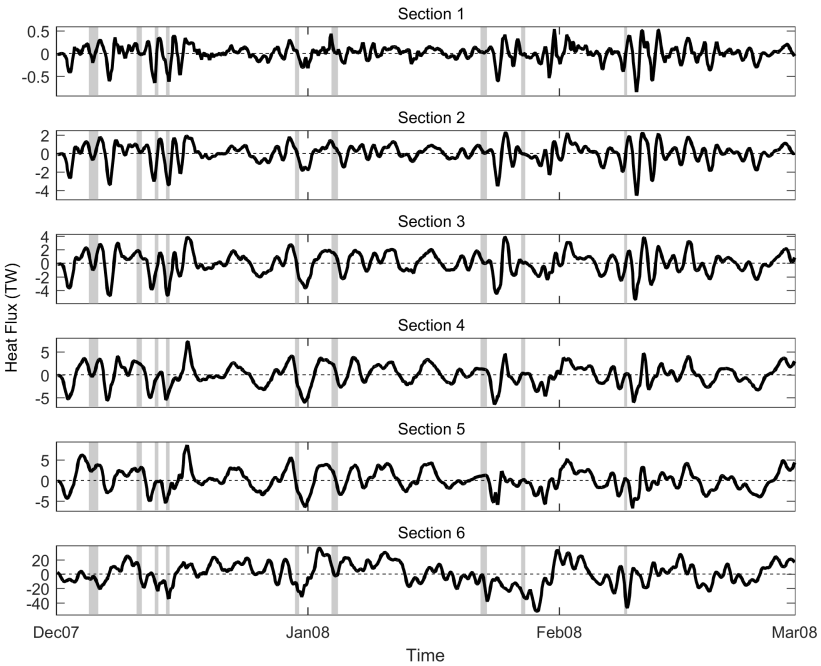

Figure 4.10: Heat flux through each of the standard cross sections of the KF/KT system.

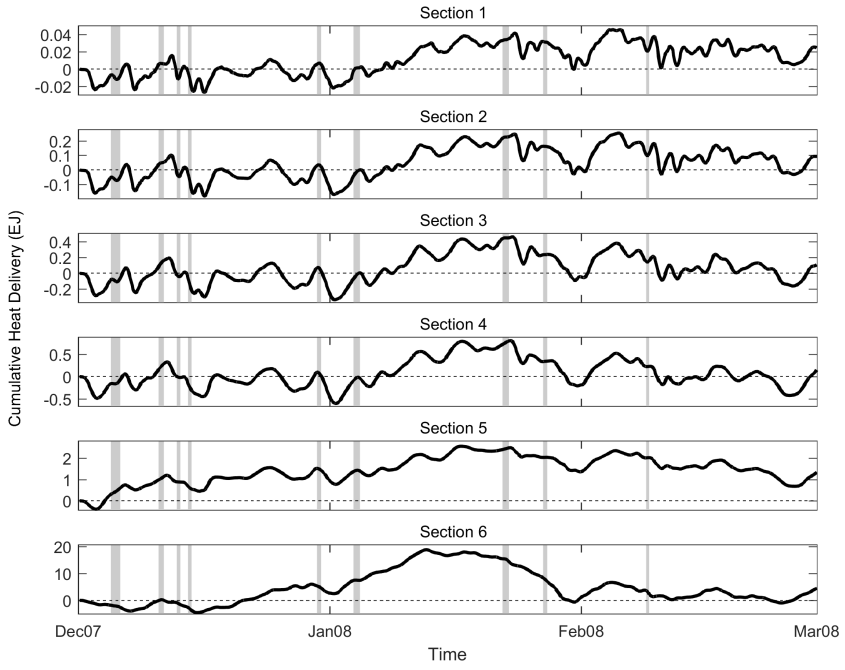

Figure 4.11: Time-integral of heat delivered through each of the standard cross sections of the KF/KT system.

Defining advective heat flux as

$$Q_\Theta = C_p \rho_0 \iint v\,(x,z)\,\Theta\,(x,z)\,dxdz \tag{4.2}$$

where C_p is the specific heat capacity of seawater and ρ_0 is reference density, we calculated time series of the heat flux through each cross-section, shown in Figure 4.10. The mean and maximum heat flux values through each section are shown in Table 4.1. Barrier wind activity generally results in an oscillating heat flux signal at all locations, with the amplitude decreasing by around a factor of 10 between the fjord mouth and the fjord head. The response to each wind event is inconsistent, differing in amplitude, frequency and number of cycles. For example, the response to cluster B is manifest as a relatively low-frequency oscillation, compared to the responses to clusters A, C and D. Figure 4.11 shows the cumulative time-integral of the heat flux plots shown in Figure 4.10.

Figure 4.12a shows time-mean melt pattern on the ice face at the northern boundary of KF. Melting is small in the upper layer and increases with depth, peaking at 350 m where the time-mean melt rate is $0.21\mathrm{m\,d^{-1}}$. Melting is also weaker at the lateral boundaries of the ice face, likely due to the dependency of melt on flow speed in the adjacent cells, so that strong melting is concentrated in the middle of the ice face. Here, the melt rate

Section no.	Mean	Max
1	0.003	0.540
2	0.012	2.275
3	0.014	3.894
4	0.019	7.294
5	0.171	8.580
6	0.572	36.000

Table 4.1: Mean and maximum heat flux (TW) towards KG through each section.

reaches a maximum of $1.0\mathrm{m\,d^{-1}}$. We generated a time series of face-averaged melting over the course of the simulation (Figure 4.12b). Variability in melting occurs on timescales of 2-4 days, corresponding to the dominant period of the internal wave field. We find a correlation coefficient of $r = 0.86$ between time series in face-averaged melt rate and adjacent flow speed, while $r = 0.30$ between melt rate and adjacent temperature. Hence, although parametrised melt rate is linear in both temperature and flow speed adjacent to the ice face (Jenkins, 2011), the large changes in flow speed at the head of the fjord make it the dominant control in the model.

4.4 Discussion

4.4.1 Cross-shelf Transport

The SSH and velocity fields on Section 6 show the mean flow to be highly barotropic, with a well established cyclonic flow pattern ($> 50\mathrm{cm\,s^{-1}}$) supplying shelf waters to the fjord mouth. Although the variability in along-KT transport appears relatively robust to wind activity, barrier wind events generally coincide with local maxima in Q (Figure 4.9) due to southward net transport. Wind events are found to initially drive offshore barotropic flow, temporarily weakening the inflow on the eastern side of KT while strengthening the outflow (Figure 4.4), which we take to be a first-order response to the barotropic pressure gradient caused by shoreward Ekman transport. The secondary positive response due to subsequent shoreward flow in the lower-layer is generally smaller. Barrier wind events hence coincide with local minima in Q_Θ in KT (Figure 4.10), provoking a decrease in northward net heat transport (Figure 4.11).

A clear exception to this follows cluster B, when the shoreward heat flux through Section 6 remains strongly positive throughout the first half of January (Figure 4.10). This period also corresponds to a small but sustained increase in cross-shelf exchange through Section 6 (Figure 4.9). The two wind events in cluster B are distinguishable by their long duration and are hence different in character to most other barrier wind events during the simulation,

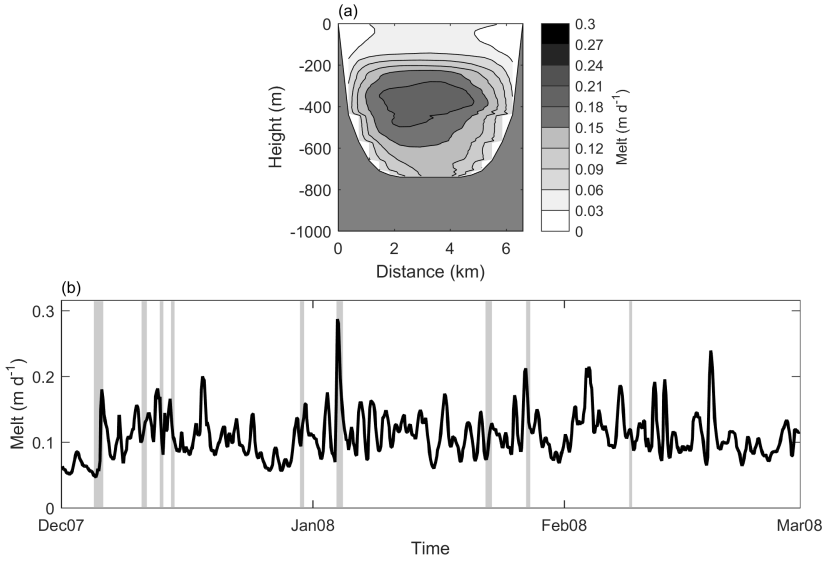

Figure 4.12: (a) Time-averaged melt rate simulated at the glacier terminus during DJF 2007-08. (b) Time-series of spatially averaged melting.

which were typically stronger, shorter gusts with a lifespan of 2-3 days. For example, the second wind event in cluster B occurred during the longest uninterrupted spell of northeasterly wind speeds in excess of $10\mathrm{m\,s^{-1}}$ during the record, which lasted 3.75 days. The wind events during cluster B were also weaker than many others during the simulation (Figure 4.1a and b), barely meeting the criteria of $20\mathrm{m\,s^{-1}}$ set by Harden et al. (2011). We investigated this further by decomposing the variability of the 10 m northeasterly wind component (Figure 4.1a) into frequency space, once again using wavelet analysis, which confirmed that cluster B coincided with the most significant low-frequency variability during the record (late December/early January, Figure 4.13).

Short, strong gusts of along-shore wind act to disrupt cross-shelf transport in KT by altering the barotropic pressure gradient on inertial or superinertial timescales. Conversely, low-frequency wind events provide sufficient time for the barotropic shelf circulation to adjust and retain geostrophic balance following the initial Ekman-driven offshore barotropic flow. As described by Nilsen et al. (2016) in west Spitsbergen, the warm trough current is then accelerated by the increased sea surface tilt over the shelf. Cluster B was hence followed by a sustained period of enhanced exchange and heat delivery.

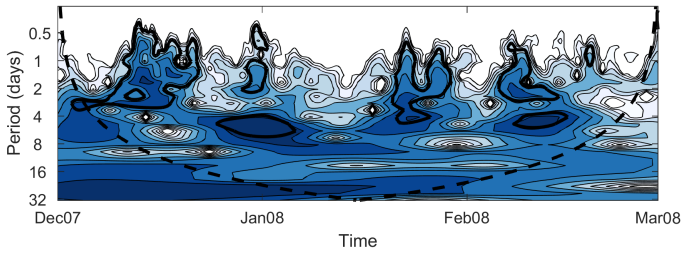

Figure 4.13: The local wavelet power spectrum from the NE component of 10m wind velocity over the deepest point in KT.

4.4.2 Circulation in the Fjord Interior

The horizontally sheared mean flow through all cross-fjord sections reaffirms the assertion, made in Chapter 3, that KF may be classified as a broad fjord and hence rotational effects are important. In this case the pycnocline was stronger and thinner than in Chapter 3, which used winter climatology data for initial conditions. That the same mean circulation pattern emerges here, under historical oceanographic conditions, indicates that it is indeed a feature of the region rather than an artifact of the relatively weak stratification inherited from the climatology data used in Chapter 3.

The EOF patterns in Figure 4.5 are symptomatic of CTW activity, due to the intensification of flow variability towards the eastern side. This corroborates the mechanism for exchange proposed in Chapter 3. We suggest that the opposing pattern found near the western bank of Section 1 is caused either by (1) the less energetic reflected wave, propagating outwards after being topographically steered around the head of the fjord, or (2) the incoming wave taking an effective mode-2 cross-fjord structure in this region. The wavelet analysis (Figure 4.8) showed the inflow variability is dominated by the 2-4 day period band, consistent with barrier wind duration, while the current time series (Figure 4.6) showed that, following barrier wind events, the velocity near the eastern side of the fjord broadly follows a highly prolate ellipse. Together, these results provide further evidence that information about shelf wind patterns propagates with the internal wave field from shelf to fjord via CTW activity, the dominant source of flow variability in KF during winter.

The broadly similar temporal patterns in the heat flux time series at each section (Figure 4.10) indicate good communication between fjord and shelf. Although changes in shelf temperature are quickly manifest in the fjord mouth and interior, the small time lags between sections suggest that information of lower layer inflow/outflow propagates up-fjord in the internal wave field as opposed to anomalous warm or cold patches advecting from KT to the head of KF. The time-mean temperature field shows a continuous along-fjord temperature gradient in the lower layer (Figure 4.3), consistent with the order-of-magnitude

decrease in the scale of heat flux variability between the fjord mouth (Sections 4 and 5) and the head of the fjord (Section 1). Along-fjord advection mediated by the internal wave field is therefore associated with high-frequency variability in the heat content of the water column at a given location.

In accordance with intermediary circulation as outlined by Straneo et al. (2010) for SF, barrier winds initially produced a negative heat flux in the fjord interior due to upper-layer inflow, which model animations reveal to be a redirected branch of the EGCC (Video 1, supplementary material). This is followed by a positive contribution from lower-layer inflow (Figure 4.10), and the expelled water in the upper layer rejoins the cold, coastal current. Due to the coastal boundary and steep topography in KF, the internal waves generated may be approximated as nondispersive Kelvin waves at a flat wall (Chapter 3, Støylen and Weber (2010); Inall et al. (2015)). Wave propagation is therefore focussed strictly along-fjord, driving a sustained oscillation in along-fjord heat flux. The CTWs which mediate the heat exchange dissipate slowly in comparison to the internal waves on the shelf (Figure 4.10).

The time-integrated heat flux increased uniformly through each section of the KF system in the first half of January, coincident with the increased cross-shelf heat transport in KT (Figure 4.11). This period was typified by a sustained, relatively low-frequency heat flux oscillation (Figure 4.10). From the wavelet analysis (Figure 4.8) we see that the preceding wind event cluster (cluster B) initiated significant low-frequency (>4 days) variability in the Section 2 inflow. This implies that low-frequency wind events correspond to low-frequency CTW activity in KF which is highly effective at delivering heat to the upper reaches of the fjord.

The reversible nature of intermediary circulation means for the process to generate non-zero time-integrated heat flux - while the fjord temperature remains stable - requires advection in the lower layer sufficient to draw inflowing water into contact with the heat sink at the KG terminus. We expect that longer-period internal waves would advect water in the warm layer a greater distance along the fjord during the inflow phase, increasing the volume of shelf water drawn into the fjord. Given the along-fjord temperature gradient in the lower layer, a greater extent of advection would increase the temperature to which the terminus is exposed and, ultimately, increasing the amount of heat withdrawn from the system. This is consistent with Figure 4.7, which shows well defined, large-amplitude waves in the thermocline during early January, corresponding to the low-frequency heat flux signal, increasing lower-layer heat content. Animations of model output (Video 1, supplementary material) reveal that the prolonged wind events in cluster B were particularly effective at depressing the pycnocline near the coast and inside the fjord. The subsequent internal waves were asymmetric in time, with the phase corresponding to lower layer inflow

dominating over the return phase, as seen in the deep layer inflow on Section 2 (Figure 4.6). Conversely, following the three other barrier wind clusters the time-integrated heat flux decreased uniformly throughout the fjord mouth and interior (Figure 4.11). Each of these periods corresponded to high-frequency heat exchange (Figure 4.10), however in each case the lower-layer outflow phase expelled more heat than was drawn in during the subsequent inflow phase, resulting in net heat loss (Figure 4.7). This result points to barrier wind duration, as opposed to strength, as the controlling parameter on the wintertime heat delivery towards the GrIS.

The model-generated mean heat flux values (Table 4.1) were generally consistent with Chapter 3, further constraining estimates of the oceanic contribution to melting at KG during the winter months. The maximal values of 2.2 TW in the mid-fjord and 0.5 TW at the fjord head are greatly in excess of observed values, all of which were taken in summer Inall et al. (2014); Sutherland et al. (2014b). The high temporal variability, caused by CTW activity, highlights the danger in taking synoptic sections of broad fjords as representative of the mean flow.

4.4.3 Melting at the Glacier Terminus

Cluster B coincided with the highest melt rates in the simulation (Figure 4.12). The high melt rates preceded the large increase in heat content within KF (Figure 4.11), indicating that they are triggered by increased flow speed (associated with CTW activity) in the adjacent cells as opposed to increased temperature. Given the close correlation between melt rate and adjacent flow speed in the model, another potentially important factor is the capacity for CTWs to induce energetic flow in the upper reaches of the fjord. The exchange flows triggered by barrier wind forcing were in general found to decay considerably between the mid-fjord and the fjord head, while the exchange flows triggered by cluster B remained highly significant at Section 1 (Figure 4.9). Theory has shown maximum particle speed to be linear in amplitude for long waves, and we therefore attribute the strong melting to the large CTW amplitudes during cluster B (Figure 4.7) as opposed to associated low-frequency signal which continued throughout the first half of January.

The modelled melt rates were two orders of magnitude smaller than the glacial flow speed at KG during 2007-08, which was around $25\mathrm{m\,d^{-1}}$ (Bevan et al., 2012). Our results therefore suggest that ocean-driven melting during the winter was not capable of sustaining the rapid flow speeds observed during this period. We suspect, however, that our model under-represents the oceanic contribution to KG frontal ablation. The iceplume package was utilised to provide a heat sink at the head of the fjord and add a level of realism to hydrography in far field. As this is primarily a study of shelf-driven exchange, the model lacks the sophistication to produce realistic glacier diagnostics. Due to the static ice face

geometry, the model cannot account for the triggering of calving events or instabilities in glacial flow due to ocean-driven melting at the terminus. The pattern of melting found on the ice face (Figure 4.12a) would drive undercutting and hence encourage calving events. Furthermore, the flat ice face likely does not affect the adjacent flow realistically, as tidewater glacier termini are typically cracked and uneven over small spatial scales. This may have caused the model to exaggerate the relative influence of adjacent flow speed over temperature.

4.5 Summary

A high-resolution numerical model of KF and the adjacent shelf region during winter 2007-08 shows good communication between fjord and shelf, with temperature changes on the shelf able to influence the fjord interior. AW is delivered from the shelf break towards the fjord by the geostrophically balanced cyclonic circulation in KT, which is driven by sea surface tilt. The mean circulation structure in KF is similar, though weaker and with a larger baroclinic contribution, and delivers heat to the glacier terminus due to mean cross-fjord temperature gradients. CTWs, instigated by barrier winds on the shelf, emerge as the dominant mode of variability within the fjord and drive greatly enhanced along-fjord volume transport and heat exchange. This mechanism has previously been observed in a broad, glaciated fjord in Svalbard and is likely to play a significant role in broad fjords in general.

The efficacy of CTWs in delivering heat towards the KG terminus, in a time-mean sense, is highly dependent on the temporal variability of barrier wind forcing. Typically barrier wind events are short and strong, ramping up quickly and exceeding the $20\,\mathrm{m\,s^{-1}}$ threshold for only $\sim$6 h. However, this class of wind forcing was not found to significantly increase fjord heat content. Long-duration northeasterly wind forcing was found to strengthen the barotropic circulation in KT, increasing AW transport towards the fjord mouth, while provoking low-frequency CTWs which are highly effective at drawing these waters up-fjord.

The results indicate that significant oceanic heat ($\sim$0.5 TW) is regularly delivered to the glacier terminus during winter. The process is driven purely by shelf exchange and, although there may be some freshwater runoff in the winter months, this is not a necessary condition.

While the model was able to provide diagnostics for melt rate at the KG terminus, yielding a mean melt rate of $0.21\,\mathrm{m\,d^{-1}}$ at the centre of the ice face, the simplified parametrisation was unable to describe ice-ocean interaction in detail. Coupled ice-ocean models, capturing glacier dynamics, calving and ice face texture, are needed to significantly further the current understanding of the rapid acceleration and retreat of Greenland's tidewater glaciers.

Chapter 5

Circulation and Exchange in a Broad Arctic Fjord Using Glider Based Observations

Adapted from *Fraser, N. J., Skogseth, R., Nilsen, N. and Inall, M. E. (2018), Polar Research.*

5.1 Introduction

High-latitude fjords are the link between the ocean and glaciers. They act as heat sinks for subtropical waters travelling poleward and, due to glacial runoff and melting, have a freshening influence on the polar oceans (Murray et al., 2010; Straneo and Heimbach, 2013). Circulation within these small, restricted regions has a unique control over the distribution of ocean heat to glaciers. Due to differences in geometry and location, all fjords behave differently so that heat and salt exchange is highly dependent on the circulation scheme within a given fjord. Ocean dynamics in Arctic fjords are generally controlled by freshwater input, tides, the atmosphere, the earth's rotation, shelf exchange and sea ice cover (Inall and Gillibrand, 2010; Cottier et al., 2010; Skogseth et al., 2004; Nilsen et al., 2008). Together, these forcings determine the extent of any vertical and horizontal circulation of water masses. The presence of seasonal ice cover means that the relative importance of the other forcings varies throughout the year, especially in the case of wind stress which is strongly suppressed in the winter. The buoyancy of the surface layer is affected by salt release during freezing in winter, resulting in convective overturning and mixing of the water column, while the opposite process occurs in summer when melting, runoff and iceberg calving bring fresh water into the fjord and increase the stratification

(Cottier et al., 2010). Under ice, vertical mixing is sustained by tides and freshwater runoff, both of which generate shear between layers in the water column, and momentum fluxes at the fjord boundaries. However, during ice-free periods, the upper layer circulation in a two-layered fjord is shown to be dominated by the wind (Skogseth et al., 2007). The steep-sided topography of fjords causes the wind direction to be mainly down- or up-fjord, either enhancing or impeding the estuarine outflow of the surface water, while acting to homogenise the upper layer through vertical mixing.

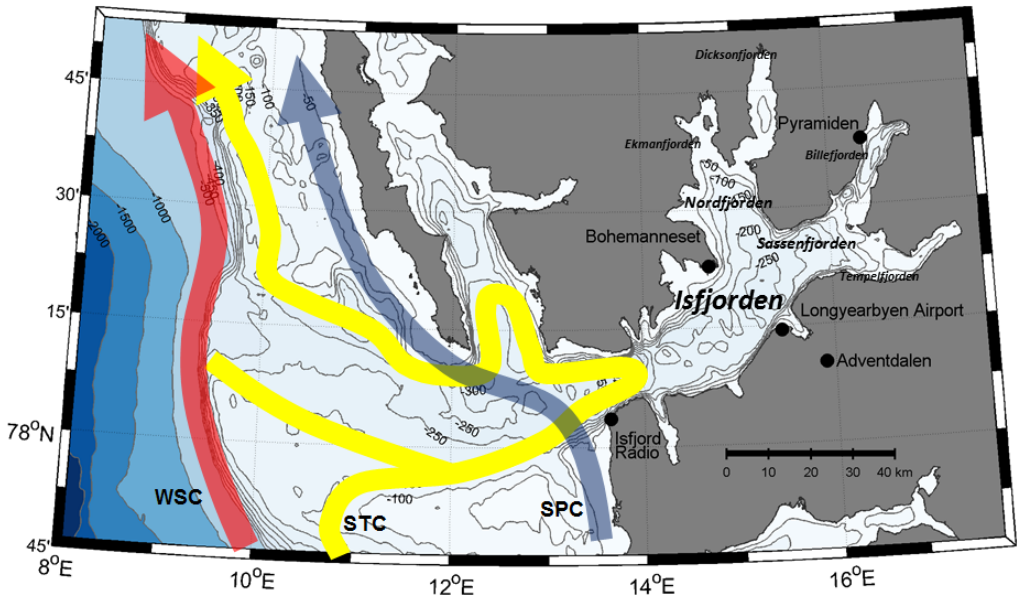

Figure 5.1: A map of Isfjorden and adjacent shelf region. All fjords are labelled in italics while black dots mark local weather stations. The West Spitsbergen Current (WSC) is shown by a red arrow, the Spitsbergen Polar Current (SPC) is shown in blue and the Spitsbergen Trough Current (STC) is shown in yellow.

Winter sea ice extent around Svalbard has decreased significantly in recent years, including the interior of Svalbard's fjords (Muckenhuber et al., 2016; Pavlov et al., 2013; Onarheim et al., 2014a). This has been linked to an increased transport of warm Atlantic Water (AW, $\Theta > 3°C$, $35.1 < S_A < 35.4$ g/kg) into the fjords caused by changes in the prevailing winds on the shelf (Cottier et al., 2007; Nilsen et al., 2008, 2016). As calving and melting of Svalbard's tidewater glaciers coincides with increased AW transport (Luckman et al., 2015), fjordic circulation is also key parameter in understanding sea level rise. Further observations of the currents within these fjords would allow a richer understanding of the dynamics of AW inflow.

Several current systems are present in the Svalbard region. A northward travelling slope

Water mass	Abbreviation	Θ (°C)	S_A (g/kg)	S_P (psu)
Atlantic water	AW	3.0 – 7.0	35.1 – 35.4	34.9 – 35.2
Transformed Atlantic water	TAW	1.0 – 3.0	34.9 – 35.1	34.7 – 34.9
Surface Water	SW	1.0 – 7.0	30.1 – 34.2	30.0 – 34.0
Intermediate water	IW	>1.0	34.2 – 34.9	34.0 – 34.7
Arctic Water	ArW	<1.0	34.5 – 35	34.3 – 34.8

Table 5.1: Definitions used for the classification of water masses during the study. Θ denotes conservative temperature. S_A denotes absolute salinity while S_P denotes practical salinity.

current, the West Spitsbergen Current (WSC), transports AW into the region along the shelf break (Figure 5.1). A geostrophically balanced branch of the WSC has been modelled meandering into the troughs on the West Spitsbergen Shelf (WSS), termed the Spitsbergen Trough Current (STC) (Nilsen et al., 2016). A coastal surface current, the Spitsbergen Polar Current (SPC), brings Arctic Water (ArW, $\Theta < 1$°C, $34.5 < S_A < 35$ g/kg) around the southern end Spitsbergen from Storfjorden and the Barents Sea. All water masses are defined in Table 5.1.

Isfjorden is the largest fjord on the west coast of Spitsbergen. It includes four side-fjord systems: Grønfjorden and Adventfjorden on the southern side, Sassenfjorden that leads to Tempelfjorden and Billefjorden, and Nordfjorden leading to Dicksonfjorden and Ekmanfjorden (Figure 5.1). Several tidewater glaciers terminate in the Isfjorden system (generally in the northern and eastern side-fjords) which have accelerated and thinned in recent decades in keeping with the wider trend across Svalbard (Nuth et al., 2010, 2013). Isfjorden does not have a shallow sill at its mouth and a 250m deep trough (Isfjordrenna) runs across the shelf from the mouth to the shelf break. It is therefore well connected to the WSS and slope area, allowing dense AW from the WSC access to the fjord. The mouth of Isfjorden is 10km wide (Nilsen et al., 2008), while inside the width increases to over 20km. Cottier et al. (2010) estimated the internal Rossby radius, L_R, to be approximately 3.6-6km for typical Svalbard fjords. Isfjorden can therefore be considered a broad fjord, and we expect rotational effects to be important.

Previous studies of the circulation in Isfjorden have focused on the trough and mouth area where the exchange of coastal water and fjord water occurs. Based on the results from the I1 current meter mooring (Figure 5.2) and CTD stations (conductivity, temperature and depth) in the mouth and shelf areas of Isfjorden, the STC and SPC have been found to circulate into the mouth region of Isfjorden. Analyses of year-round current measurements show a seasonality such that the STC is stronger in the winter and early spring than in summer and autumn, and recent modelling results link the extent of STC penetration into the fjord mouth to large-scale wind forcing (Nilsen et al., 2016). On the shelf, southerly

winds act to converge the surface layer in the SPC waters against the coast, raising sea level height and causing downwelling of the pycnocline. This deepens the SPC, which circulates across the Isfjorden entrance to form a barrier between shelf and fjord. Sea surface tilt over the shelf break is increased, accelerating the barotropic WSC and shifting it eastward, forcing the STC to follow shallower isobaths on the shelf and hence enhancing AW/TAW transport towards the fjord mouth (Nilsen et al., 2016). Under these conditions the deep layer AW and TAW have restricted access to the fjord due to geostrophic control, a mechanism whereby the barotropic currents on the shelf are prevented from circulating beyond the fjord mouth due to large horizontal density gradients between fjord and shelf (Klinck et al., 1981). The STC, effectively blocked-off from the fjord interior by the SPC, instead circulates around the fjord mouth before continuing northwards along isobaths on the shelf. This mechanism has been previously described both in Isfjorden (Nilsen et al., 2008, 2016) and other broad fjords in west Spitsbergen (Svendsen et al., 2002; Cottier et al., 2005). In contrast, northerly winds cause a divergence of the surface layer near the coast. This diminishes sea surface tilt, weakening the barotropic pressure field which drives the WSC, and drives an upwelling of the pycnocline, increasing heat content of the water column on the shelf (Nilsen et al., 2016). Off-shore Ekman transport acts to diminish the geostrophic control mechanism by flattening out the isopycnals between the SPC and the deeper STC circulating in the mouth, which opens the door to rapid deep layer exchange flows between fjord and shelf. Hence, through differing mechanisms, both northerly and southerly winds can increase heat flux towards Isfjorden from the shelf break. There is a relatively sparse literature on circulation and exchange in broad fjords (Ingvaldsen et al., 2001; Svendsen et al., 2002; Skogseth et al., 2005; Janzen et al., 2005; Johnson et al., 2011; Inall et al., 2014, 2015; Sundfjord et al., 2017; Carroll et al., 2017), and it is unclear how the circulation within Isfjorden, as a broad fjord, interacts with the exchange mechanism described above, which is applicable regardless of fjord width.

The objectives of this chapter are to (1) classify the dominant circulation within Isfjorden, (2) quantify the exchange of heat between fjord and shelf and (3) study the effect of changing large-scale atmospheric forcing on the circulation and hydrography of the Isfjorden interior, extending the current understanding beyond the shelf and mouth regions. To this end we deployed two Slocum gliders to Isfjorden in November 2014, which profiled the salinity and temperature of the water and also provided measurements of the depth-averaged currents (DAC) in the fjord. These data were combined to calculate the absolute geostrophic velocity fields in cross-fjord sections, giving an insight into the vertical current structure. The glider data was supplemented by atmospheric data from both local weather stations and an atmospheric model. While gliders have previously been used in a fjord mouth region (Bachmayer et al., 2007), the survey marked the first time that gliders have been operated within a fjordic system. Unlike the existing mooring data, gliders provide

velocity data with a spatial aspect, providing a new insight into the circulation patterns in Isfjorden.

Parameter	Sensor	Manufacturer	Accuracy
Conductivity	SBE-41 CTD	Sea-Bird	± 0.005g/kg
Temperature	SBE-41 CTD	Sea-Bird	± 0.002°C
Pressure	SBE-41 CTD	Sea-Bird	$\pm$2db
Oxygen	Optode 3835	Aanderaa	8μM or 5%
Turbidity	ECO-FLNTU	Wet Labs	0.01 NTU
Chlorophyll-a	ECO-FLNTU	Wet Labs	0.025μg l^{-1}

Table 5.2: Sensors used during the glider mission in Isfjorden and their accuracies.

5.2 Methods

5.2.1 The Slocum Glider

Gliders are autonomous, buoyancy-driven, underwater vehicles used to profile the physical and chemical properties of the water column. They were first detailed in Doug Webb's lab book in 1986 and publicized in 1989 by Henry Stommel (Stommel, 1989). A number of different gliders have been developed and used by various organizations, but the two gliders that were operated in Svalbard are Slocum gliders. A Slocum glider is a 1.8m long, torpedo-shaped, winged autonomous underwater vehicle (AUV). It has a forward speed of $20 - 30$cm s^{-1} and it propagates with a sawtooth-shaped gliding trajectory of up to 1000m depth, surfacing between dives. Forward propulsion is derived through a combination of buoyancy change and pitch-angle adjustment, and steering by means of a tail fin rudder. The navigation system uses an on-board GPS receiver coupled with an altimeter sensor and magnetic compass, and back-up positioning and communications are provided by an Argos transmitter. The two-way communications with the vehicle are maintained by RF modem or the global satellite phone service Iridium. All antennas are located within the tail fin, which is raised out of the water when the vehicle surfaces. As a power source the glider uses either alkaline or lithium batteries, but the energy consumption is highly dependent on the amount of sensors, the sampling frequency, the diving depth, the stratification and how often the glider surfaces. The duration of one mission may therefore vary from approximately 20 days up to 1 year. Gliders can be equipped with several sensors depending on the project in question. The default sensors are a depth sensor, conductivity and temperature. In addition, gliders can be used as a platform for current meters, turbulence instruments, and sensors to measure the optical properties of water. Depth-averaged current (DAC) measurements are provided for each dive. When a glider surfaces, it uses GPS to determine its position and can compare this to the position

at which it is expected to surface through the use of 'dead-reckoning' (based on an internal magnetic compass and velocity through the water). The difference between these positions can be attributed to horizontal advection, and thus used to calculate current velocities. The DAC is intrinsically depth-averaged as a consequence of the fact that the gliders only have accurate positional data when on the surface. This relies on the assumption that a glider moves at a constant vertical velocity and hence spends equal time at each depth level. Merckelbach et al. (2008) estimated that, due to possible poor calibration of the sensors and the glider's calculation method, the error in DAC data may be up to $2 - 3\text{cm}\,\text{s}^{-1}$.

Table 5.2 contains the full list of sensors that were used during the Isfjorden mission, the accuracies given here provided by the sensor manufacturers. The two gliders carried additional oxygen, fluorescence, chlorophyll-a and turbidity sensors. Glider CTDs and navigation systems were last calibrated in October/November 2011 and January 2012 respectively. More details about gliders and their operation is available in Schofield et al. (2007).

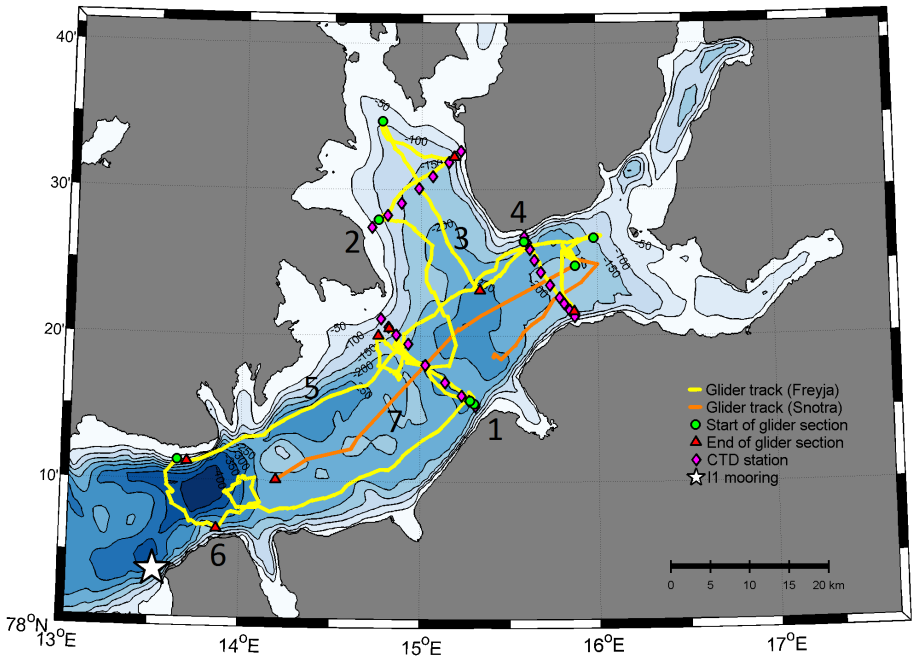

Figure 5.2: The paths of the two Slocum gliders operated in Isfjorden, Svalbard, in November 2014 are shown as yellow and orange lines. Green circles (red triangles) show the the start (end) of sections, with section number shown in black. Purple diamonds show CTD locations and the I1 mooring location is marked by a white star.

5.2.2 Mission Summary

A Slocum glider, "Freyja", was deployed on the 7th of November 2014 around the entrance to Adventfjorden, embarking on a comprehensive survey of the Isfjorden area over the following three weeks. Figure 5.2 shows the path taken by the gliders during the survey, while Table 5.3 details the location, start time and end time of each section. The glider took a transverse section of Isfjorden (Section 1) before entering Nordfjorden where it took two sections, one across-fjord (Section 2) and one along-fjord (Section 3). It then took a cross-section of Sassenfjorden (Section 4) before taking a section along the north side of Isfjorden (Section 5). For this section it was joined by "Snotra", a second Slocum glider, which was deployed on 13th of November 2014, also around the entrance to Adventfjorden, before heading towards the head of Isfjorden. Once there, Snotra took a section along the centre of Isfjorden, southward of that taken by Freyja (Section 7). The intention was to continue this trajectory out onto the WSS region, however Snotra detected a leak near the mouth of Isfjorden and had to be recovered early. Section 7 data contains a gap as a result of this malfunction. Finally, Freyja covered the mouth area of Isfjorden with a cross-section (Section 6) and then returned to retrace Section 1 (hereafter Section 1b). Freyja and Snotra were rated to a depth of 200m and 1000m respectively.

Section no.	Instrument	Location	Start Time	End Time	n
1	Freyja	Isfjorden mid-fjord	2014-11-07 19:30	2014-11-08 17:05	12
2	Freyja	Nordfjorden	2014-11-11 08:25	2014-11-12 05:41	16
3	Freyja	Nordfjorden	2014-11-12 21:45	2014-11-14 14:38	27
4	Freyja	Sassenfjorden	2014-11-15 09:05	2014-11-16 08:02	13
5	Freyja	Along Isfjorden	2014-11-18 19:50	2014-11-22 07:05	46
6	Freyja	Isfjorden mouth	2014-11-22 07:55	2014-11-23 00:50	10
7	Snotra	Along Isfjorden	2014-11-18 12:25	2014-11-21 17:35	27
1b	Freyja	Isfjorden mid-fjord	2014-11-26 13:30	2014-11-27 14:30	13
1 (CTD)	SBE19plus	Isfjorden mid-fjord	2014-11-20 09:51	2014-11-20 14:44	8
2 (CTD)	SBE19plus	Nordfjorden	2014-11-12 12:56	2014-11-12 16:48	7
4 (CTD)	SBE19plus	Sassenfjorden	2014-11-13 15:50	2014-11-13 20:50	10

Table 5.3: Overview of each section taken using either glider or CTD. Glider section start/end times are rounded to the nearest half hour. For glider sections n is the number of dives while for CTD sections n is the number of casts taken.

5.2.3 CTD Sections

The hydrography data from the Slocum gliders were complemented by ship-based CTD profiles taken using the Sea-Bird Electronics SBE19plus V2 CTD. Since ship-based CTD sections are generally carried out faster than glider transects, the CTD sections are less influenced by temporal changes and may hence be considered more synoptic. They were

therefore used as a basis of comparison to test the accuracy of the glider hydrography data and hence gauge the usefulness of gliders in a high-latitude fjord environment. The temporal disparity between glider and ship-based hydrography sections was in all cases less than 2 weeks, and in most cases 2-3 days. In order to give context to the time evolution of the hydrography within Isfjorden during the campaign, the November 2014 conditions at Section 1 were compared to CTD sections taken at the same location in both April and September that year. The SBE19plus was calibrated in March 2012. Section times and locations are given in Table 5.3, with the locations also marked in Figure 5.2.

5.2.4 Atmospheric Data

November 2014 data from five nearby weather stations were compiled in order to study the interaction between fjordic circulation and wind forcing. The stations were located at Isfjorden Radio, Bohemanesset, Longyearbyen Airport, Adventdalen and Pyramiden, shown in Figure 5.1, and gave 10m wind speed and direction data with a 6-hourly temporal resolution. Isfjord Radio, Longyearbyen Airport and Pyramiden are weather station data delivered from eKlima (met.no) while Bohemanneset and Adventdalen are UNIS weather stations. Output 10m wind fields from the 2.5km resolution AROME-Arctic model (Seity et al., 2011) were interpolated onto the mid-time and mid-position of each glider dive, so as to compare each DAC measurement to the local wind conditions. The model also was used to provide 2m air temperature data which were spatially averaged over the Isfjorden region, taken here as $78 - 78.5°$N, $13 - 17°$E, and linearly interpolated onto the same 6-hourly time-step as the weather station data.

5.2.5 Glider Data

The DAC values after each dive were assigned to the mid-point between the dive start and end position, essentially collapsing a V-shaped dive onto a single position. This was based around two assumptions: firstly, that horizontal variability is small and, secondly, that the glider followed an approximately linear course while underwater. The second assumption may not be valid when the glider was navigating a crooked path between sections, but should be reasonably accurate for when the glider was taking straight sections. Vertically sheared currents could also have caused the glider to follow a non-linear path, thus making this assumption less valid. Due to the fact that the glider uses a magnetic compass to navigate while underwater, the raw velocity data were referenced to magnetic north rather than geographic north. Magnetic declination is relatively large in Svalbard and, crucially, varies by around $2°$ throughout the region of study. The DAC vectors were therefore each converted into a geographical co-ordinate system using a localised transformation.

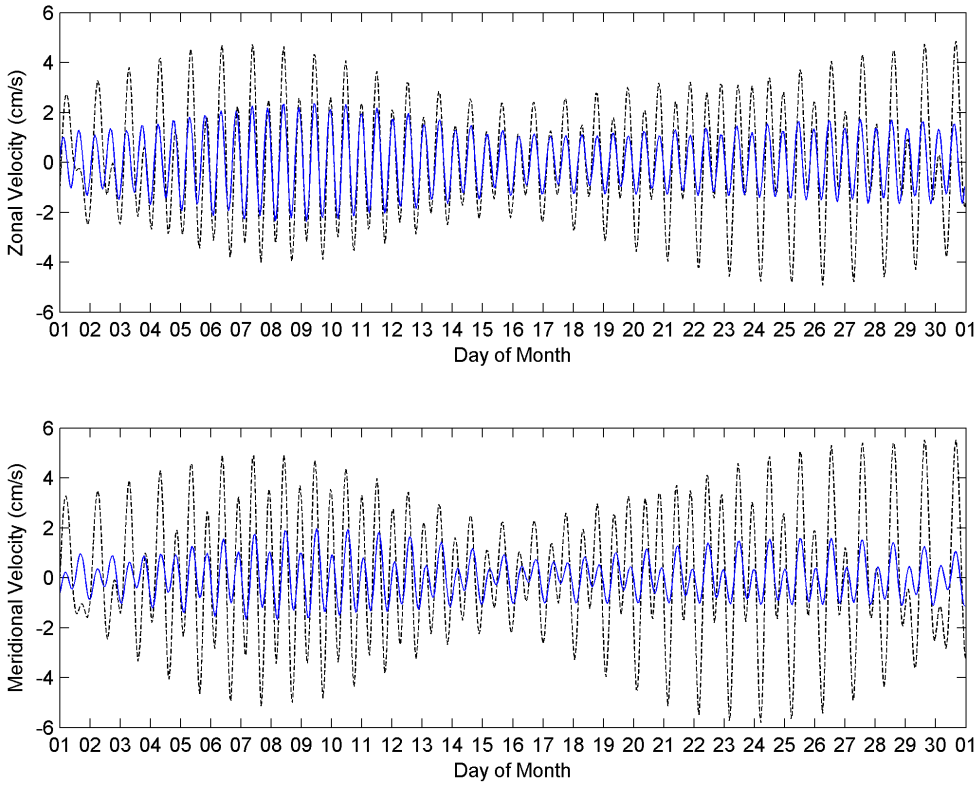

Figure 5.3: Comparison of AOTIM-5 output (blue) to tidal constituent data from ADCM data (dashed black) at the I1 mooring site, November 2014.

In order to later equate the DACs to calculated geostrophic velocities, tidal velocity data were obtained via the Arctic Ocean Tidal Inverse Model (AOTIM-5) (Padman, 2004). The model, which describes a barotropic ocean at 5km resolution, was used to acquire the tidal velocity components at the mid-point (and mid-time) of each dive (dive displacement was generally less than 1km and dive duration was less than 2 hours in all cases). These velocities were then subtracted from the observed depth-averaged velocities in order to eliminate barotropic tidal signal from the data. AOTIM-5 output was compared to barotropic tidal velocities from acoustic Doppler current meters (ADCM) at three different depths (50, 100, and 200m) on the I1 mooring near the mouth of Isfjorden (Figure 5.2), in order to test the accuracy of the tidal model in the region of study. Tidal analysis of the ADCM data was performed using the "t_tide" MATLAB package (Pawlowicz et al., 2002). Figure 5.3 shows that, while the two results are generally in phase, the model significantly and systematically underestimates tidal velocities at the mooring site for November 2014. This may be caused by an intensification of tidal currents near coastal boundaries which is not resolved

by the 5km model grid. We therefore anticipate residual tidal signal will contaminate the DAC measurement, with the effect likely to be smaller away from coastal boundaries. We proceed with the tidal subtraction method in order to reduce the tidal signal in the DAC data, though it may not eliminate it completely.

Uncertainties may also occur due to wind-driven dynamics when the glider is on the surface. When the glider first surfaces it has no knowledge of position and must wait for a GPS connection. Hence, the time taken for this connection to be established and the magnitude of the wind stress both contribute to a potential wind bias in the DACs. This time interval was generally around 1 minute and was in all cases less than 2 minutes.

Whenever the pressure reading fell below a given threshold, all hydrographic data were considered to be from the surface and therefore not deemed to be of interest. The threshold pressure was usually 0.2db, but was sometimes adjusted to ensure that all surfacings were registered. Glider CTD lag was corrected according to the methods described in Garau et al. (2011). Absolute salinity, conservative temperature and pressure data from each glider section were interpolated onto a 1km $\times$ 1m grid and smoothed at 3km $\times$ 3m resolution using Barnes' objective analysis method (Barnes, 1994). Some adjustment of the smoothing radii was carried out and we chose the largest smoothing radii which did not remove what we believed to be physical features.

The hydrography fields were used to generate absolute velocity fields. The thermal wind equations, rotated into a fjord-oriented basis (Equation 1), shows how vertical shear is a function of the horizontal density distribution.

$$-f\frac{\partial v}{\partial z} = \frac{g}{\rho_0}\frac{\partial \rho}{\partial x} \tag{5.1}$$

Here x indicates the across-fjord coordinate, z is the depth coordinate, v is the along-fjord velocity, f is the Coriolis parameter, ρ is the density and ρ_0 is the reference density. Integrating over depth yields the geostrophic velocity at each depth level relative to the sea surface velocity (for this calculation we used functions provided in the Gibbs Seawater Oceanographic Toolbox (McDougall, Trevor J. ; Barker, 2011)). Some adjustment parameter, v_{ref}, is then required in order to find the absolute velocities:

$$v\left(x,z\right) = v'\left(x,z\right) + v_{ref}\left(x\right) \tag{5.2}$$

where we have defined

$$v'\left(x,z\right) = -\frac{g}{f\rho_0}\int_z^0 \frac{\partial}{\partial x}\rho\left(x,z'\right)dz' \tag{5.3}$$

The v' fields were referenced using the DACs. The DAC vectors were interpolated onto the

same horizontal grid as the geostrophic velocity fields at the surface, and the component perpendicular to the given section, $v_{\perp}^{DAC}$, was used to generate an adjustment parameter, v_{ref}, at each grid location:

$$v_{ref}(x) = -\frac{1}{H}\int_{-H}^{0} v'(x,z)\,dz + v_{\perp}^{DAC}(x) \tag{5.4}$$

Here H is the maximum observed depth. The result is a depth-varying velocity field that is calibrated using observed data, giving an insight into the vertical velocity structure. This method includes the barotropic component of the geostrophic flow as the DACs are intrinsically barotropic, but we cannot eliminate ageostrophic terms such as wind stress, bottom drag and any residual tidal signal. We hereafter refer to these fields as absolute velocity.

5.3 Results

5.3.1 Atmospheric Forcing

Wind vectors for the month of November 2014 are shown in Figure 5.4, with the glider and CTD section durations shown along the same timescale. At Isfjord Radio (Figure 5.4a), situated on the west coast of Spitsbergen, the prevailing wind direction was from the north during the first half of November. However, after the 15th, this pattern was punctuated by a series of strong southerly winds with increasing regularity, such that from the 22nd onward the prevailing winds were southerlies. Two particularly strong shelf wind events occurred during the study, with strong northeasterlies at Isfjorden Radio between the 7th and 9th of November, and strong southerlies on the 22nd and 23rd, each with wind speeds of over $15\,\mathrm{m\,s^{-1}}$. Strong southerly wind events also occurred on the 15th and 27th, though these were of shorter duration. The wind events were captured by the other stations situated inland from the coast, with similarly high wind speeds but often in a different direction to those on the shelf due to topographic steering. Up- and down-fjord are not necessarily 180 degrees out from one another at the stations on headlands. For instance the winds at Longyearbyen Airport were predominately southerly with a shift from southeasterly (down-fjord) to southwesterly (up-fjord) starting on the 15th. During down-fjord winds, the winds at Longyearbyen Airport match those at Adventdalen, indicating that it is affected by wind blowing out of Adventfjorden. The up-fjord winds at the same locations are directed into Isfjorden. At Bohemanneset, the winds were predominately northerly (out of Nordfjorden) prior the 15th, with the southwesterlies (into Isfjorden) in the latter half of the month corresponded to strong southerlies on the shelf. 10m wind vectors from the end of each dive, plotted at corresponding glider surfacing times and

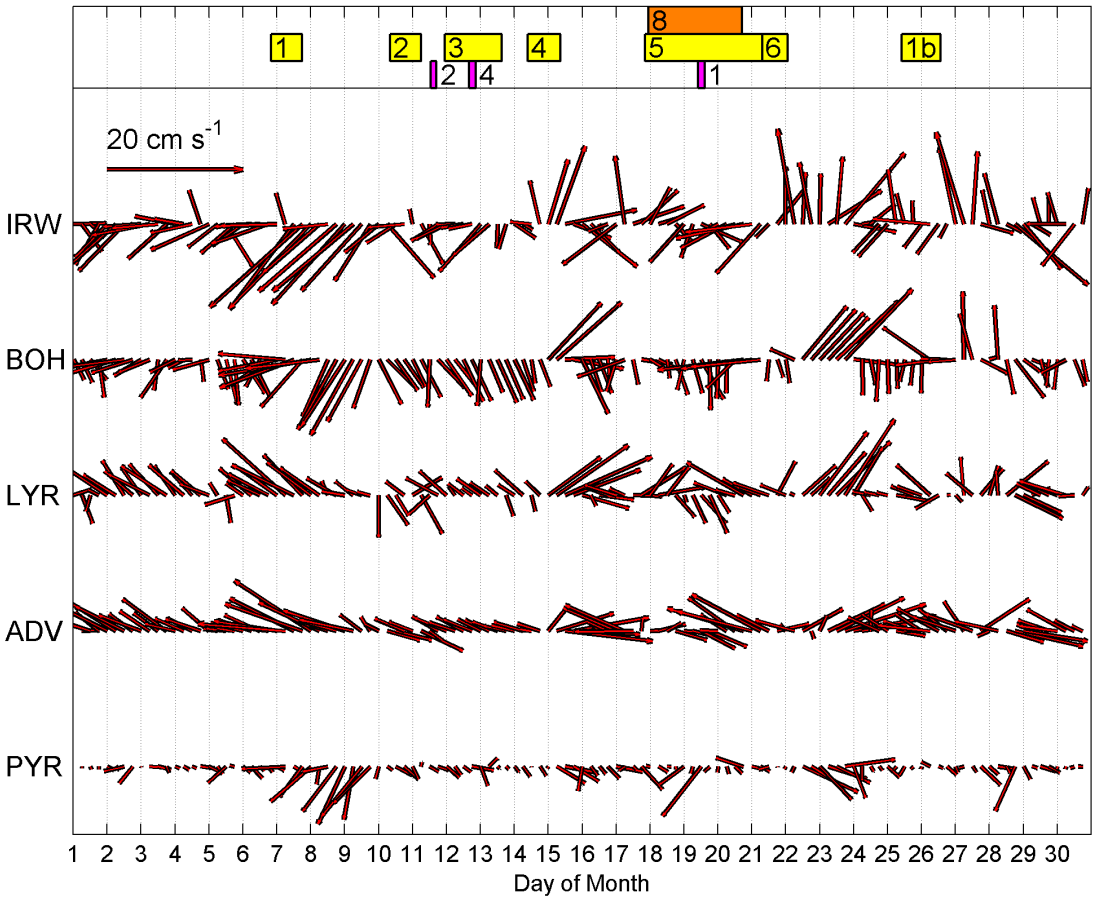

Figure 5.4: 6-hourly wind velocity time series at Isfjord Radio Station (IRW), Bohemanneset (BOH), Longyearbyen Airport (LYR), Adventdalen (ADV) and Pyramiden (PYR) for November 2014. The bar along the top of the figure shows the time periods during which sections were being taken, with yellow and orange denoting Freyja and Snotra, and purple denoting CTD.

positions, are shown in Figure 5.5.

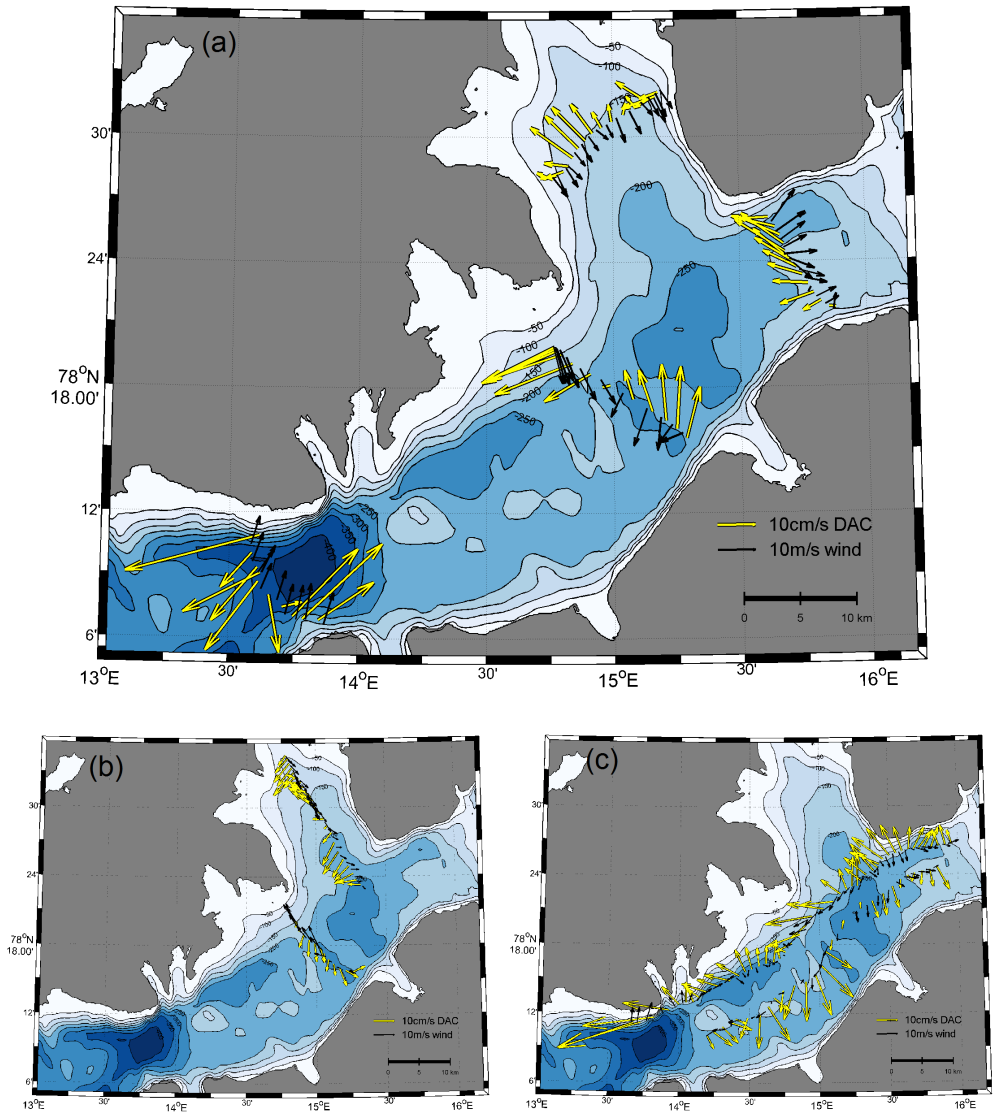

Figure 5.5: De-tided DACs, overlayed with corresponding 10m wind velocity from the the AROME-Arctic model, in (a) across-fjord sections in November 2014. Sections 3 and 1b (b) and along-fjord Sections 5 and 7 (c) are shown separately to avoid overlap. DACs vectors (cm/s) are shown in yellow while 10m wind vectors (m/s) are shown in black.

The mean of the modelled 2m temperature data (Figure 5.6) over Isfjorden before the 15th of November was $-12.6°C$, while after the 15th this increased to $-5.6°C$. Any temperatures greater than $-2°C$ corresponded to strong southerly shelf winds ($> 11 \mathrm{m\,s^{-1}}$).

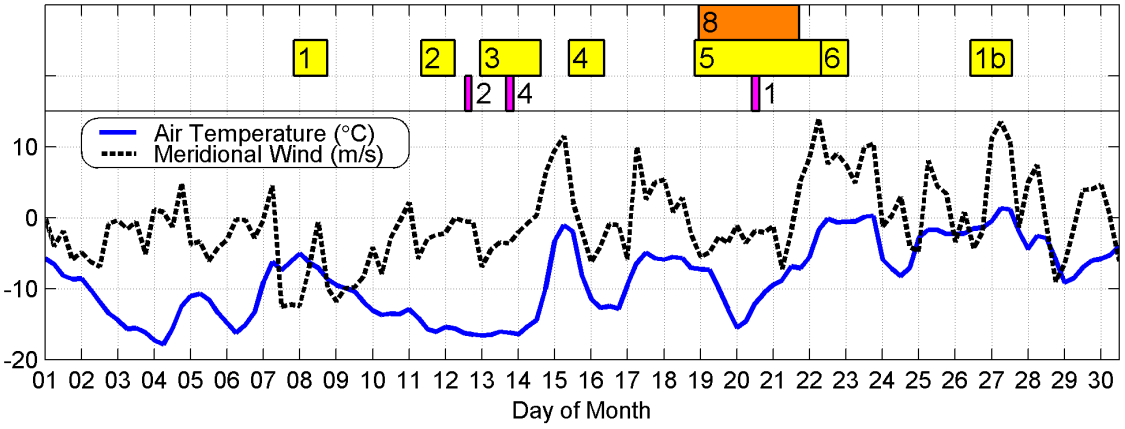

Figure 5.6: Air temperature at 2m height in the Isfjorden region from the AROME-Arctic model (blue) along with the meridional wind component from Isfjord Radio weather station (dashed black). The bar along the top of the figure shows the time periods during which sections were being taken, with yellow and orange denoting Freyja and Snotra, and purple denoting CTD.

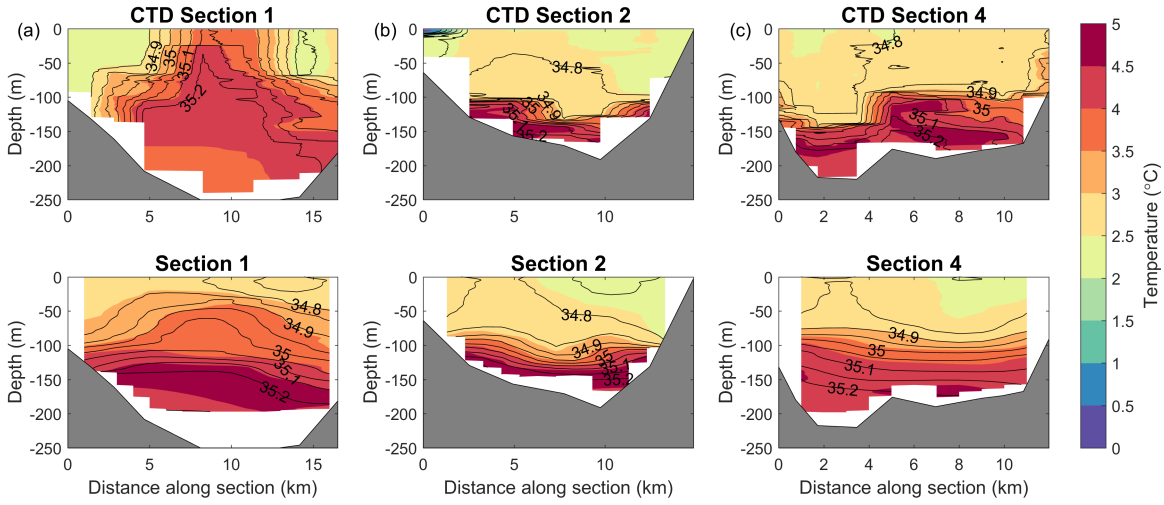

Figure 5.7: Conservative temperature (°C) and absolute salinity (g/kg) from CTD for cross-fjord Sections 1, 2 and 4, with the corresponding glider section shown beneath for comparison. Sections 1 and 4 are viewed looking east, Section 2 is viewed looking north. Colour contours denote conservative temperature while solid black lines denote isohalines.

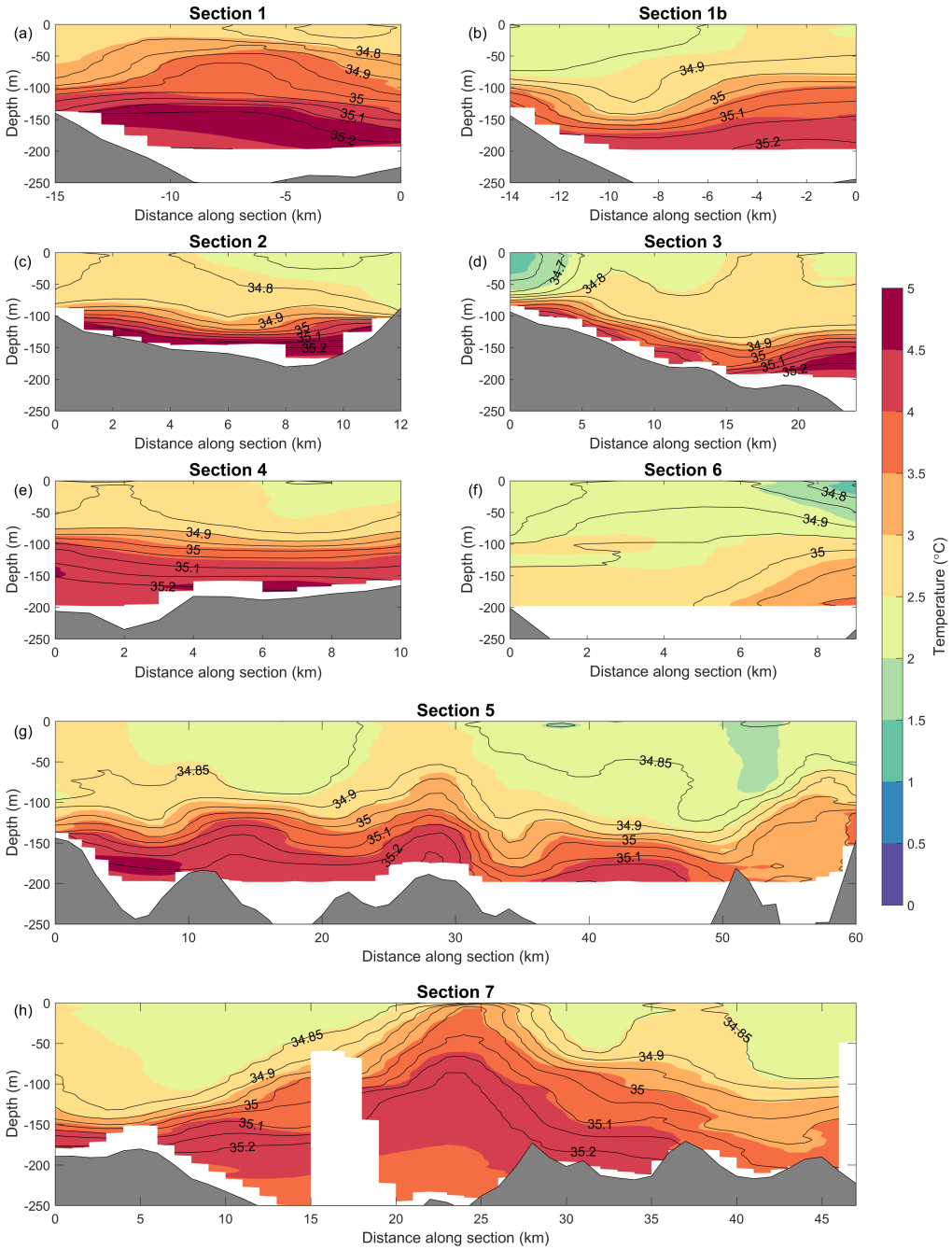

Figure 5.8: Conservative temperature (°C) and absolute salinity (g/kg) from all glider sections. All sections are viewed looking east, other than Section 2 which is viewed looking north and Sections 5 and 7 which is viewed looking south. The negative scale on the horizontal axis for Section 1 is due to the fact that, unlike the others, this section was taken from right to left as viewed in the figure. Colour contours denote conservative temperature while solid black lines denote isohalines. In (g), the fjord entrance is at 50km, with the fjord mouth beyond.

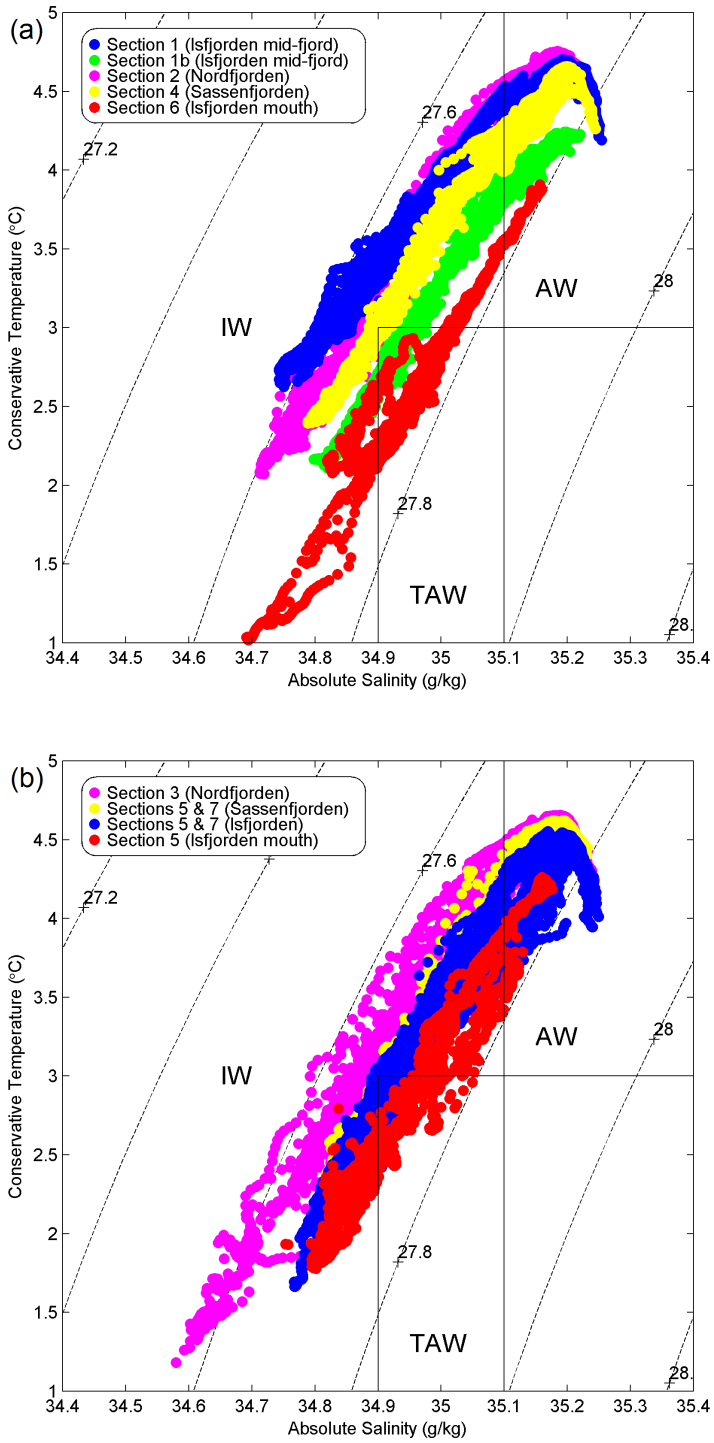

Figure 5.9: $\Theta - S_A$ diagram (a) cross-fjord sections of Isfjorden, Nordfjorden, Sassenfjorden and the Isfjorden mouth region and (b) along-fjord sections of Isfjorden and Nordfjorden. Data from the different sections are denoted by colour. Black boxes denotes AW, TAW and IW classifications.

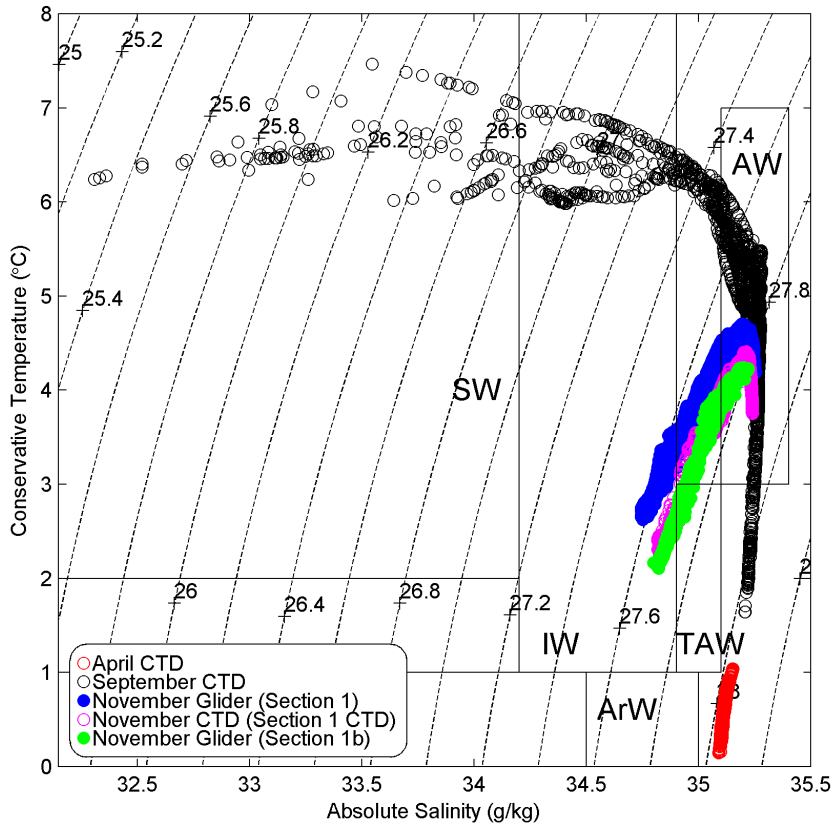

Figure 5.10: $\Theta - S_A$ diagram showing the evolution of central Isfjorden between April and November 2014, combining CTD and glider data.

5.3.2 Hydrography

Conservative temperature and absolute salinity for corresponding glider and CTD sections are compared in Figure 5.7, with all glider hydrography shown in Figure 5.8. While Sections 1, 2 and 4 were covered by both the CTD and the glider, they do not always coincide exactly, as ship-based CTD casts were taken around 1km closer to shore than the glider can safely operate, and they may exceed Freyja's maximum dive depth of 200m. The hydrographic structure is in good agreement between the ship-based CTD data and corresponding glider data (Figure 5.7), particularly at Section 2 where the two transects were taken one day apart. This gives confidence in glider CTD calibration and in the gliders' ability to measure the conditions over cross-fjord sections on a synoptic timescale. However, this may not hold when wind forcing is changing significantly during the time period the transects are occupied, such as in Sections 5 and 7 which were taken over several days (Figure 5.4).

The hydrography sections (Figure 5.8) indicate that, during the period of study, Isfjorden may be treated as a two layer, salinity-stratified system, with the pycnocline generally weaker at the mouth and stronger towards the head of Nordfjorden and Sassenfjorden. Much of the Isfjorden interior displayed a well mixed surface layer ($S_A \approx 34.8$ g/kg, $2 < \Theta < 3$°C) around 100m in depth, which falls under the category of Intermediate Water (IW, $\Theta > 1$°C, $34.2 < S_A < 34.9$ g/kg, (Svendsen et al., 2002)). Below this depth we see a deep layer consisting of both Transformed Atlantic Water (TAW, $1 < \Theta < 3$°C, $34.9 < S_A < 35.1$ g/kg), a water mass generated by the mixing of AW and ArW (Svendsen et al., 2002), and AW. The range of temperature and salinity values detected by Freyja and Snotra are displayed in $\Theta - S_A$ space in Figure 5.9. The lighter water masses within the fjord generally fall along a mixing line between IW and AW, with no Surface Water (SW, $1 < \Theta < 7$°C, $30.1 < S_A < 34.2$ g/kg) present, while AW is found in the deep layer. Temperature generally increases moving in-fjord from the mouth, with the coldest waters found in Section 6 and the warmest waters found at the entrance to Nordfjorden (Section 3). Based on the available hydrographic data, we estimated L_R to be 1.2km.

Sections 1, 5, 7 and CTD Section 1 all see the pycnocline tilt upwards in the Isfjorden mid-fjord region such that it almost reaches the surface, and taken together these sections describe a convex dome of warm and saline water residing there, centred around 5km northeast of the intersection of Sections 1 and 7 (Figure 5.2). Section 1b, taken 6 days later than CTD Section 1 at the same location, does not see this feature, the pycnocline having flattened out to a depth of around 100m. Sections 2 and 3 see pockets of AW, some of the warmest observed in the region, reside near the bottom of Nordfjorden centred above the 100m isobath on both sides and at the head of the fjord. Warm AW is also located at depth in Sassenfjorden, as seen in Sections 4 and 5. In Sections 5 and 6, the deep layer in the fjord mouth was found to be colder than that in the fjord interior, and the stratification weaker. The freshest, coldest waters were found above 100m at the north end of Nordfjorden (Section 3) and on the surface at the southern side of the Isfjorden mouth (Section 6).

The additional CTDs (Figure 5.10) show that cold, saline ArW occupied the Isfjorden mid-fjord in April. The September data show a straight mixing line between these April conditions and AW, which suggests that AW was introduced into the fjord during the summer. There is also evidence of surface freshening over the summer due to the presence of very light and warm SW in September that has mixed with AW creating a warm IW. By November the SW is no longer present, with the entire upper layer consisting of colder IW falling along a mixing line between AW and ArW.

Section no.	$\overline{\lvert v_{ref}(x)\rvert}$	$\max(\lvert v_{ref}(x)\rvert)$
1	6.8	15.5
2	6.1	13.6
3	6.5	10.3
4	6.0	8.0
6	13.5	26.7
1b	2.8	6.2

Table 5.4: Adjustment parameters used when referencing the absolute velocities using the DAC referencing method, $v_{ref}(x)$. The adjustment is different for each dive and therefore depends on the lateral position, x. Here the mean and maximum absolute values are given for each section. All values are given in cm s^{-1}.

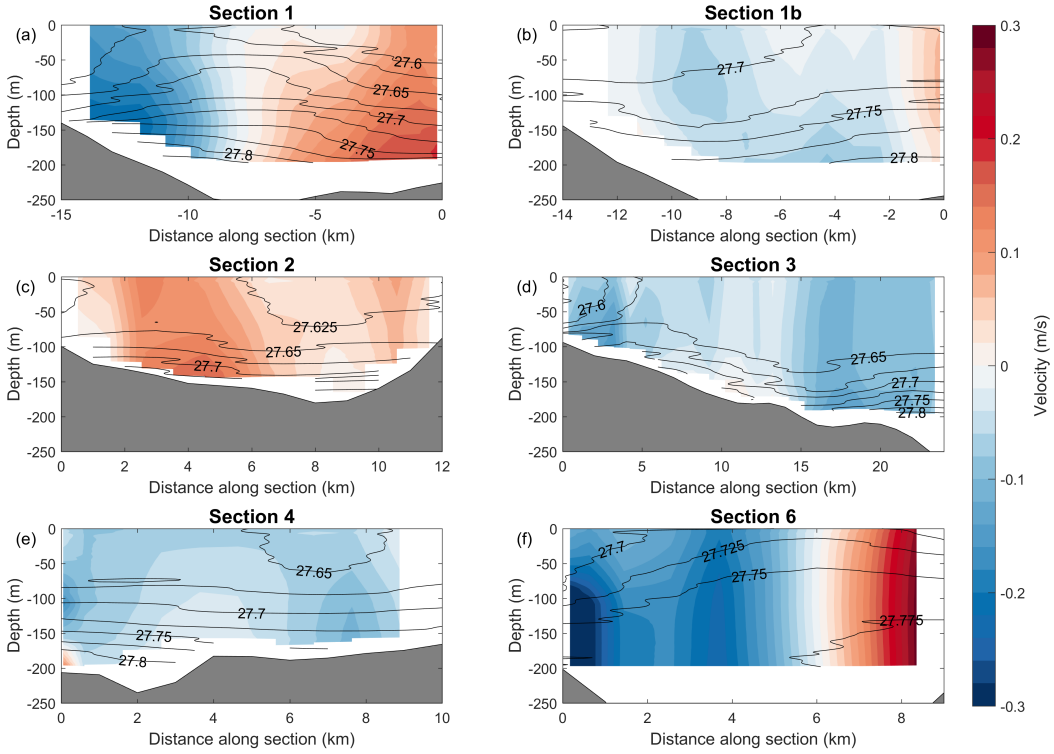

Figure 5.11: Absolute velocity fields, for cross-fjord Sections 1, 1b, 2, 4 and 6 and along-fjord Section 3. All sections are viewed looking east, other than Section 2 which is viewed looking north. Positive velocity here means a flow into the page. Solid black lines denote isopycnals of σ_θ.

5.3.3 Depth-Averaged Currents

The de-tided DACs for all cross-sections are shown in Figure 5.5. Speeds of up to 30cm s^{-1} were observed across the fjord mouth (Section 6). In the fjord interior the DACs were considerably weaker, with the maximum value of 22cm s^{-1} observed in Section 1. Tidal currents seldom exceeded 2.5cm s^{-1}, and so had a significant influence only in regions where the DACs were particularly weak. The DACs demonstrate across-fjord current variability in all cross-sections, though the velocity structure is highly variable between the sections. Section 1 and, in particular, Section 6 describe a strong inflow (outflow) near the southern (northern) shore of Isfjorden. Section 1b, which retraced Section 1 19 days later, did not exhibit this behaviour as strongly, displaying a generally southward flow, out of the fjord, with a small region of moderate inflow ($\sim$ 7cm s^{-1}) adjacent to the southern boundary. Section 4, across the entrance to Sassenfjorden, describes a generally westward flow of $\sim$ 10cm s^{-1} with some variability in the current direction. Westward currents are observed both across the entrance and around the head of Nordfjorden (Section 3), with northerly flow found on either side (Section 2). Section 5 describes an inflow on the right hand side of the Nordfjorden entrance, and generally shows an outflow along the northern bank of Isfjorden. Section 7 describes strong southerly flows along the centre-lines of both Sassenfjorden and Isfjorden, with some southeasterly currents to the southwest of the Isfjorden mid-fjord region.

5.3.4 Absolute Velocities

The absolute velocity and potential density for fjord cross-sections are shown in Figure 5.11. Although vertical shear was evident throughout the region, this was not always obvious in regions where the barotropic term from v_{ref} was dominant, such as in Sections 1 and 6. Section 1 sees fast inflows and outflows at all depths on the respective southern and northern sides, but also sees current speeds increasing with depth such that current cores are positioned at 200m. Section 6 has a similar horizontal structure but with stronger current speeds and a weaker baroclinic signal, with some vertical shear evident near the surface on the northern side. Sections 1b and 4 describe a net outflow of Isfjorden and Sassenfjorden respectively, with some cross fjord variability but no distinct velocity pattern. Section 2 shows a northward flowing current core at depth towards the western side of Nordfjorden, while Section 3 describes westward flow at depth towards the north end of Nordfjorden, and a westward flow across the mouth of Nordfjorden at all depths. The mean adjustment parameter, v_{ref}, for the entire study was 7.0cm s^{-1}, with a maximum value of 26.7cm s^{-1} found in the Section 6 outflow region. The mean and maximum values for v_{ref} in each section are included in Table 5.4.

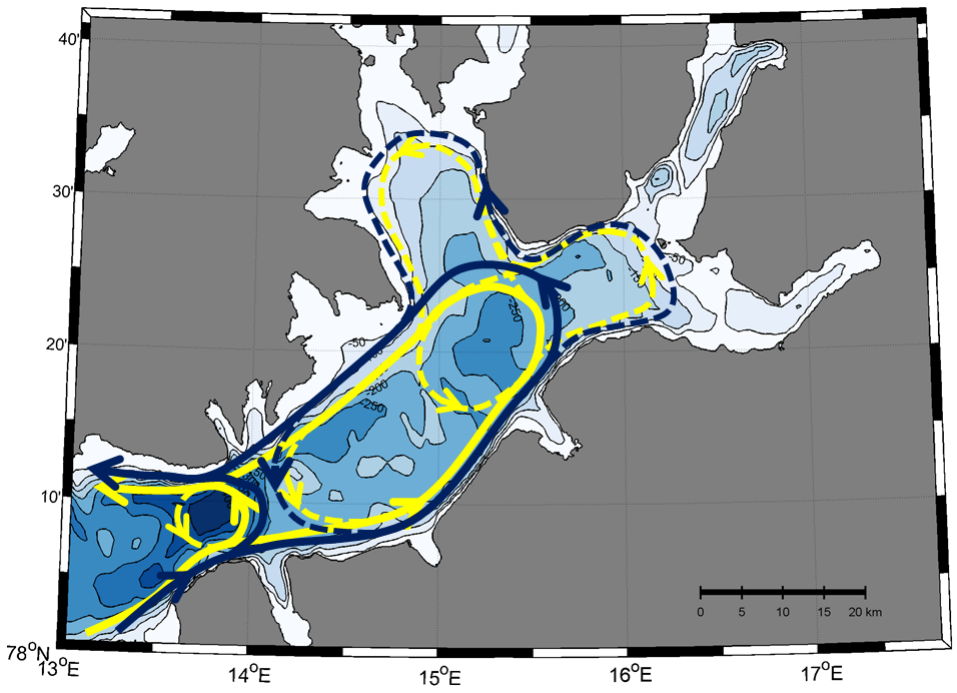

Figure 5.12: Schematic of the circulation and shelf exchange scheme in Isfjorden. The lower layer circulation is denoted by yellow arrows, the upper layer by blue. Dashed lines indicate proposed pathways which were not observed directly.

5.4 Discussion

5.4.1 Circulation Patterns in Isfjorden

The DACs from Sections 1 and 6 display cross-fjord geostrophic circulation in central Isfjorden and in the mouth-region, where the inflow takes place on the right-hand side and, correspondingly, outflow is observed on the left-hand side (looking into the fjord). This is consistent with the doming isopycnals in the mid-fjord region of Isfjorden which are symptomatic of a cyclonic eddy centered there. The DACs from the mid-fjord region in Sections 3 are also consistent with this cyclonic circulation structure. In the eastern and northern parts of Nordfjorden the DACs appear to follow a cyclonic flow pattern (Figure 5.5), as would be expected in the geostrophic case. These results are in general agreement with other studies that report three-dimensional circulation in broad fjords in Svalbard (Ingvaldsen et al., 2001; Skogseth et al., 2005; Svendsen et al., 2002; Sundfjord et al., 2017; Carroll et al., 2016) and Greenland (Johnson et al., 2011; Inall et al., 2014; Carroll et al., 2017). The DACs from the end points of Sections 1 and 6 flow approximately tangent to isobaths, indicating that the geostrophic flow is guided by topography. Currents following

contours deeper than ∼200m will circulate around central Isfjorden and have limited access to Nordfjorden and Sassenfjorden and, thus, to glacier termini. This is consistent with the eddy pattern seen in the Section 1, 3 and 7 DACs, and the doming feature seen in Section 1, 7 and CTD Section 1 hydrography. In Section 1b we see a southward flow in all but the southernmost DAC vectors. While qualitatively this fits the criterion of inflow (outflow) on the right (left), the strength of the inflow is much diminished in comparison to Section 1 and is not large enough to compensate for the outflow.

The absolute velocity field for Section 6 (Figure 5.11f) is dominated by the barotropic signal, since the z-independent v_{ref} was large. The dominance of the barotropic signal is likely due to the weak stratification here, hence we see velocities throughout the water column following the same isobaths, as is expected in a rotating barotropic fluid (Taylor, 1917). Section 1 (Figure 5.11a) sees a similar geostrophic circulation pattern reside in the fjord interior, inherited from the DACs, though the baroclinic term describes significant vertical shear and in general produces faster currents in the deeper layer than those at the surface. The fastest inflow in central Isfjorden, Section 1, is observed at around 200m, the maximum dive depth for Freyja.

The geostrophically balanced flow structure in the mouth and main body of Isfjorden (Sections 6 and 1), in not observed in the shallower side-fjords, Nordfjorden and Sassenfjorden (Sections 2 and 4). In the northwestern part of Nordfjorden the DACs measured in Sections 2 and 3 seem to converge as the westward flow at the head of the fjord meets a northward flow near the western shore. If the circulation in Nordfjorden were geostrophically balanced, we would instead expect southward flowing currents on the western shore of the fjord, contrary to those seen in Section 2. The Section 3 temperature and absolute velocity fields (Figures 5.8d and 5.11d) together describe a westward travelling AW current core following the 100m isobath. However, on the western side of Section 2 (Figure 5.11c), there is a northward flow of the entire water column, intensifying with depth, while on the eastern side we see northward flow which is strongest at the surface, both of which contradict this interpretation. The currents in Sassenfjorden, seen in Section 4, are largely directed out of the fjord without any counter flow, which suggests a net draining of the fjord. A small inflow can be seen in the southernmost DAC vector in Section 4, a similar structure to Section 1b, but it is not large enough to balance the outflow. The DACs in these regions may be more influenced by ageostrophic effects, giving a value for v_{ref} which is not representative of the barotropic geostrophic signal, therefore obscuring the mean velocity structure in Nordfjorden and Sassenfjorden. It is likely, however, that the barotropic currents observed in the main body of Isfjorden are steered by contours deeper than the side fjords, and hence have a limited influence on these regions.

We anticipated that the time spent by the glider on the surface before and after dives would

skew the DAC towards the surface velocity, which is heavily influenced by wind activity. Counter-intuitively, the opposite appears to be true, particularly in Sections 2 and 4 where the DAC vectors lie opposed to the 10m wind velocity vectors. Possible causes include residual tidal signal, supposing tides are stronger in Nordfjorden and Sassenfjorden than captured by the tidal model, and barotropic seiching motions. However, Section 4 was around 23 hours in duration, so tides cannot account for the sustained out-fjord velocities found there. The barotropic seiching period, given by Merian's formula $T = {}^{4L}/\sqrt{gH}$ (Von der Mühll, 1886), is on the order of 1 hour in Nordfjorden and Sassenfjorden, given a fjord length L of 25km and an average depth H of 150m, so again this does not explain the observed DAC structure. We speculate that the small inflows seen in the southernmost DACs of Sections 4 and 1b may represent intensified inflows residing above the steep, narrow slope, which were not fully captured by the glider due to their small spatial extent and proximity to the coast. A similar phenomenon may explain the seemingly unbalanced circulation in Section 2.

In cases where the DACs have no clear geostrophic influence we appeal to the hydrography, which is less variable over short timescales, to give a better indication of the background circulation pattern. Section 2 hydrography (Figure 5.8c) points towards a geostrophic current at depth, where we see a downward sloping of the isopycnals towards the boundaries and two AW cores, one on either side of the fjord bottom. This type of structure is not seen in the density distributions of either Sections 4 (Sassenfjorden) or 1b, each of which is consistent with a lateral overturning circulation.

5.4.2 Heat Distribution and Transport

From the $\Theta - S_A$ diagram (Figure 5.9), we see that temperature increases with distance into the fjord, with the warmest waters found in Nordfjorden and the coolest found at the fjord mouth, showing that AW is able to penetrate the upper reaches of the Isfjorden system. Relatively little AW was found in Section 6, however the water depth at the Isfjorden mouth exceeds 400m, so it is possible that AW was resident there at a greater depth than the 200m rated glider was able to observe. The differences between the water column in the fjord and in the mouth are highlighted at the western end of Section 5 (Figure 5.8g), where a vertical temperature front is present 50km along the section between the IW in the fjord interior and SPC origin water found in the mouth. The absence of these mouth-resident water masses throughout most of the fjord interior suggests that the front is caused by a branch of the SPC circulating across the fjord entrance. This is consistent with the cold inflow seen at the southern side of Section 6 (Figure 5.8f). A downwards slope towards the fjord is observed in the isohalines (which are a good proxy for the isopycnals, not shown) outside the fjord (beyond 50km in Figure 5.8g), restricting AW or TAW exchange in the lower layer

as explained in Nilsen et al. (2008). This coastal downwelling is due to the strong southerly winds recorded at Isfjord Radio at this time. The density front associated with the negative (eastwards) tilt of the pycnocline, together with increased northward barotropic flow due to the positive sea surface tilt, indicates a geostrophic control mechanism which acted to shut off the fjord from the shelf. Although geostrophic control was in place during the occupation of Section 5, the introduction of AW into the fjord system between April and September (Figure 5.10) implies that deep layer exchange flows are sometimes permitted.

The absolute velocity and hydrography fields from Section 6 were combined to give a positive heat flux of 0.13 TW, indicating that heat is delivered up-fjord by the geostrophically balanced shelf currents circulating in the mouth. This seems to contradict the cooling trend seen in the time evolution of the fjord over November (Figure 5.9a). However, due to the geostrophic control observed in Section 5 where the AW outside the fjord is cut off from that inside by coastal downwelling in the mouth, it cannot be assumed that this heat was delivered to the fjord interior. We may have witnessed an anomalously warm region of the STC on the southern side of Section 6, destined to simply recirculate in the fjord mouth before continuing northwards on the shelf. Also, as previously noted, the water depth at Section 6 is considerably deeper than the maximum glider dive depth, giving rise to large uncertainties in the calculated heat flux value. The result is valuable, however, for estimating the potential magnitude of heat delivery when geostrophic control is not in place. Results from synoptic sections of broad fjords in Greenland give a heat flux of the same order, with Inall et al. (2014) reporting 0.26 TW in Kangerdlugssuaq Fjord, Rignot et al. (2010) finding 0.16 TW in Tor Fjord and Johnson et al. (2011) finding a flux of 0.31 TW in Petermann Fjord. Sermilik Fjord is similarly sized though narrower than L_R at the mouth, and the circulation there is therefore restricted to a simple two-dimensional overturning structure. Synoptic measurement of the temperature and background circulation have given a heat flux of only 0.029 TW (Sutherland and Straneo, 2012) in Sermilik, although this value may be considerably higher if one assumes a non-zero net contribution over time from the first baroclinic mode (Sutherland et al., 2014b). The order of magnitude difference highlights the capacity for broad fjords, such as Isfjorden, to accommodate intense exchange flows which rapidly redistribute heat.

5.4.3 Atmospheric Controls

The strong northeasterly wind event at Isfjorden Radio, starting on the 7th of November (Figure 5.4), is indicative of a northerly shelf wind which is directed out-fjord through topographic steering. Strong winds are found at all weather stations during this event, and in each case they are locally oriented down-fjord. Likewise, when strong southerly shelf winds are detected at Isfjorden Radio, such as on the 22nd and 23rd, an up-fjord

wind is detected at all other stations. It is worth noting this correlation between the along-shelf wind direction and the direction of the wind stress acting locally on the fjord as we see evidence for local wind activity driving two-layer, cross-fjord circulation patterns via surface Ekman transport. The upwelling on the northern side of Sassenfjorden (Figure 5.8e) indicates a cross-fjord velocity component in the Ekman layer due to the strong up-fjord winds detected on the 15th (Figure 5.4). Similarly, the cross-fjord tilt in the pycnocline in Section 1b may be a residual effect of the moderate out-fjord wind on the 24th and 25th at Bohemanesset (Figure 5.4c). This type of response to the action of along-fjord winds is a feature specific to broad fjords. Due to localised topographic steering of winds, we may therefore indirectly associate lateral redistribution of heat and salt with large-scale weather changes.

The change in $\Theta - S_A$ properties at Section 1 between September and early November (Figure 5.10) indicates two scenarios; either that the IW inside the fjord was cooled and then mixed with AW, or that the fjord was subject to an influx of ArW (or ArW influenced IW). The prevailing northeasterlies at Isfjorden Radio during the beginning of November (including the particularly strong northeasterlies between the 7th and the 9th of November, during which Section 1 was taken) would have acted to lift the pycnocline in the fjord mouth. Given a good agreement between the density structure in the fjord mouth and that in the fjord, this would allow a geostrophically balanced, largely barotropic exchange flow to advect deep-layer AW from the shelf into the fjord interior. The $\Theta - S_A$ signature within Isfjorden in November closely matches that on the shelf (Figure 5.9a), therefore the transformation in water properties between the September CTD section and Section 1 (Figure 5.10) may be attributable, at least in part, to an intrusion of shelf-resident water at this time. This is reflected in the exchange flow seen in the Section 1 absolute velocity field (Figure 5.11a). Furthermore, because of the doming feature in the Section 1 hydrographic fields (Figure 5.8a), currents intensified with depth due to thermal wind shear so that the strongest exchange took place in the deep layer. Sections 2, 3 and 4, taken after the northerly wind event had ceased, show that the AW in the deep layer was also able to reach Nordfjorden and Sassenfjorden.

The temporal change in hydrography and velocity structure in central Isfjorden between Sections 1, CTD 1 and 1b may be linked to both atmospheric heat exchange and fjord/shelf exchange flows, both of which may be attributed to the shift in on-shelf weather patterns between mid and late November. Meridional wind direction is also closely linked to air temperature above Isfjorden (Figure 5.6) because southerly winds bring warm air into the region from the tropics while northerlies transport cold air from the Arctic. Section 1 was taken during the period when northerly winds were dominant, CTD Section 1 was taken during the transition in prevailing wind direction, while Section 1b was taken when the

prevailing winds were from the south. In CTD Section 1, the water temperature was lower than in Section 1 while the gradient in $\Theta - S_A$ space remained the same, consistent with heat loss to the atmosphere. Although meridional wind stress on the shelf was weak (Figure 5.6), the doming feature in central Isfjorden had become more pronounced, bringing AW into direct contact with the atmosphere, and indicating that a cyclonic eddy structure persisted there even after the strong northerly on-shelf winds had relaxed. We therefore suggest that, during this time, the deep-layer circulation in central Isfjorden was dynamically independent from the strongly barotropic circulation in the fjord mouth due to a reinstated geostrophic control mechanism (Figure 5.12), and that the cooling observed there was due to strong atmospheric heat loss enhanced by the doming structure. The air was colder (~ -10°C) than at any other time in the second half of November, further evidence of strong atmospheric heat loss. In Section 1b the deep layer had cooled further still while the central doming was no longer apparent, so that the deep layer was well insulated from the atmosphere. The air temperature was the warmest seen in November (~ 0°C), weakening the temperature gradient at the air-sea interface and therefore diminishing atmospheric heat loss. Geostrophic control was in place on the 22nd in the westernmost part of Section 5, and we presume that this remained true during Section 1b as strong southerlies prevailed on shelf throughout this time. The $\Theta - S_A$ diagram for November (Figure 5.10a) confirms this, with the constant gradient indicating a continuation of the cooling trend between the 7th and the 20th, with no evidence of further deep-layer exchange. However, the $\Theta - S_A$ structure in the mouth (Figure 5.10, Section 6) was similar, though denser, to that of the fjord interior, and the introduction of this mouth-resident water into the fjord interior would also lead to water masses consistent with those seen in Section 1b. We therefore acknowledge that while air-sea heat flux was weak due to increased air temperatures, we may have witnessed additional cooling through upper-layer exchange during the period of strong southerly winds in late November.

5.4.4 Evaluation of Glider Performance

The glider data was able to provide a description of the circulation within Isfjorden in greater detail than was previously available. The spatial resolution of the temperature and salinity data was generally higher than that from the ship-based CTD sections (Table 5.3). A crucial advantage is the ability to obtain current measurements with equally high spatial resolution, giving a spatial aspect to the circulation not offered by mooring-mounted current meters. The ability to combine DAC and potential density data to yield a two-dimensional, absolute velocity field allowed us to generate a richer picture of the circulation structure than offered by moorings.

Several key issues need to be considered when assessing the performance on the Slocum

gliders in this environment. A fundamental problem with any point measurement that is used to cover an area spatially, like a glider, is that between the measurements there is a time lag. If the glider progresses with a horizontal speed of 30cm s^{-1}, it will take around 10 hours to cover a 10 km long section, compared to around 2 hours for a CTD transect. Over 10 hours the wind and tidal currents will be subject to change, and so spatial and temporal variability are inseparable. This will likely affect the upper layer hydrography and DAC measurement in particular, as wind forcing may cause these to change over shorter time scales than the conditions at depth. This intrinsic uncertainty could explain the observed pile-up of water in northwest Nordfjorden. As these two convergent flows were measured at different times, it is probable that they are due to temporal fluctuations in the mean flow and do not together represent a steady state. Encouragingly, comparison of Sections 2 and 4 with their CTD section counterparts (Figure 5.7), each taken within 2 days of the relevant glider section, shows no drastic change in the deep layer hydrographic structure, suggesting that the glider hydrography data may be considered synoptic for shorter cross-fjord sections.

The gliders' DAC measurement relies on a dead-reckoning procedure which may be inaccurate in regions of high vertical or horizontal shear. Also, the DACs are unable to distinguish between geostrophic and ageostrophic velocity components, such as tides, boundary layer flows and barotropic seiching motions. Modelled tides were subtracted from the observed currents in an effort to counter the effect of high frequency tidal signal. However, the model resolution of 5 km may have failed to capture some of the finer tidal velocity structure in this restricted region with steep topography, leading to a residual ageostrophic tidal signal in the DAC data. The uncertainty in DAC measurement due to wind-driven surface drift, during the time interval between the glider surfacing and picking up position data via GPS, is not known. Although the positions used for the DAC calculation are based on GPS fixes generally taken immediately before diving and immediately after surfacing, the time taken to establish a GPS fix after surfacing is subject to variability. One potential means of overcoming this effect in future would be to use data from the gliders drift times between dives to estimate the effect of wind forcing on the subsequent dive. However, this would rely on a new set of assumptions over GPS lag times and the steadiness of wind forcing.

The glider coverage was not as extensive as that offered by ship-based CTD sections, which is easily seen by comparing Section 1, 2 and 4 to their corresponding CTD sections (Figure 5.7). Firstly, the fact Freyja was rated to only 200m meant that the deepest waters in the region could not be surveyed in Sections 1, 6 and 7. This is seen in Figures 5.8g and 5.8h, where the the 1000m glider Snotra was able to follow the bathymetry more closely Freyja. Comprehensive depth coverage of Section 6 would allow for a more accurate calculation of the heat flux through the fjord mouth. Secondly, the gliders were

not navigated as close to shore as the ship was, so that glider sections were in general shorter than the CTD sections. When studying regions with intensified coastal currents this issue is particularly problematic, as these currents may have small spatial extents but make large contributions towards volume transport. This type of issue may have arisen in Sections 1b and 4, where the inflow did not compensate the outflow, and the glider failed to cover the most southerly part of the sections. In each case, in the moderate inflow seen in the southernmost DAC vector we may have glimpsed the fringes of a localised slope current, having failed to navigate the glider through its core. Gliders are generally flown on-shelf or in the open ocean, so in this study extra caution was required by the pilot not to ground the glider in this confined area with steep topography. If glider missions are to become a conventional survey technique for fjords then it is likely that the spatial coverage they offer will increase as pilots and researchers gain experience and confidence in these environments. The feasibility for glider-based measurements is, at present, substantially reduced in fjord systems containing substantial sea ice/iceberg cover. Gliders are starting to be used in regions of non-zero sea ice concentration (Lee and Thompson, 2017) and near icebergs (Zhou et al., 2015), indicating that these obstacles can be overcome in a fjordic setting.

5.5 Summary

The glider mission in Svalbard provided a new insight into the circulation patterns in Isfjorden, as well as on the operation of gliders in the polar night and in shallow fjordic systems. No previous studies of the circulation inside fjords have been carried out using gliders, nor have gliders been operated at such high northern latitudes during the polar night. The complex topography of fjords, varying sharply in depth and relatively small in area compared to the continental shelf and the open ocean, presents a new frontier for glider technology, but, based on this experiment, gliders can be successfully operated in certain fjordic environments. The spatial resolution was excellent, providing both cross- and along-fjord sections of DAC, while providing CTD data which was subsequently used to calculate geostrophic currents and to study the hydrography. The horizontally sheared flow regimes observed in the DACs in central Isfjorden and at the mouth indicate that geostrophy has a major influence on the circulation in these areas. This type of circulation has the capacity to rapidly deliver heat to broad fjords, and here we calculated a positive heat flux of 0.13 TW at the mouth. However, the DACs in Sassenfjorden and Nordfjorden do not give such a clear picture. Although some across-fjord velocity structure was observed, as is expected in broad fjords such as these, there is less evidence for steady, geostrophically balanced flows. This lead us to believe that the barotropic, contour-following currents seen to dominate in Isfjorden may have a less profound influence in these shallower regions,

potentially influencing the pathways for AW toward glacial termini. Large-scale weather systems on the shelf have been seen to influence the water mass structure and circulation scheme within Isfjorden through both local and nonlocal effects. Northerly wind conditions on the shelf coincided with geostrophic exchange flows with the potential to rapidly alter the heat and salt content within the fjord, and generated a cyclonic circulation pattern in central Isfjorden. This cyclonic pattern continued after the northerlies subsided, bringing warm water from the deep layer into contact with the air so as to increase heat loss to the atmosphere. Subsequently, southerly winds were seen to tilt the density front between the SPC and the STC in the fjord mouth, restricting deep layer exchange. Since the shelf waters were denser than those in-fjord, SPC-water may have joined the surface circulation inside the fjord, restoring the insulating surface layer. During northerlies (southerlies) the wind stress on the fjord interior is topographically steered out of (into) the fjord, resulting cross-fjord velocities in the surface which redistribute heat and salt to produce lateral density gradients and alter the geostrophic balance within the fjord.

The DAC measurements were limited by the uncertainties associated with wind and tides, as well as the entanglement of spatial and temporal change. The gliders' spatial coverage of fjordic sections, in both the vertical and horizontal, can be improved upon in future though the use of a deeper diving instrument and bolder piloting. High resolution data for tidal velocity would have allowed for a more accurate representation of the barotropic geostrophic velocity field. As the first survey of its kind, the results shown here would benefit from comparison with future glider missions in the region. It would be instructive as to which of the features observed here are transient fluctuations, and which are symptomatic of the long-term mean circulation in the region. Furthermore, repeated monitoring such as this would help to identify any temporal trends in air-sea interaction, which is crucial for understanding the recent decrease in winter sea ice extent in Svalbard's fjords.

Chapter 6

Evaluation and Conclusions

6.1 Context and Significance

Due to the chaotic nature of geophysical fluid systems, the differences in location and geometry, and both seasonal and interannual variability, we will never achieve a comprehensive and general description of high-latitude fjord circulation and exchange. Recent efforts to constrain these systems, motivated by rapid changes to the cryosphere, have been relatively successful in quantifying the major dynamical drivers and understanding where and when they are likely to dominate.

Glacial acceleration and retreat has been particularly acute in SE Greenland. A recent surge in research activity here, including both modelling and observations, has designated buoyancy-driven and intermediary circulation, forced by freshwater input at depth and by coastal downwelling due to barrier winds, respectively, as the key processes governing exchange and, by extension, the oceanic impact on glacial stability. Several publications have reasoned that buoyancy-driven circulation is dominant in summer, when freshwater input is maximal, while intermediary circulation likely dominates the exchange in winter, when barrier wind events are most frequent. However, there has been a tendency for the literature to focus on summertime conditions due to the difficulty in obtaining wintertime observations from the interior of SE Greenland's major fjords, and a tendency for modelling studies to build upon observational results. Furthermore, previous fjord modelling studies in the region have placed open boundaries at the fjord mouth or entrance. While this is suitable for studying freshwater-driven convection at the ice-ocean boundary, it prohibits detailed study of the interaction between fjord and shelf. Together, these factors have acted to hinder progress in quantifying fjord-shelf heat exchange during the winter months. The chief objective of this thesis was to investigate the potential for wintertime exchange to deliver significant heat to the interior of major Greenlandic fjord systems. A

numerical model, comprising both fjord and shelf, was constructed and subject to a variety of forcings designed to replicate winter conditions. Firstly, an experimental configuration was employed in order to study the system under typical winder conditions. Next, the model was run with historical forcing fields in a longer simulation designed to recreate winter 2007-08. No previous modelling study of SE Greenland fjords has been designed with the specific intention of constraining winter heat exchange.

Svalbard fjords have experienced increasing heat content in the last two decades, attributed to a greater influx of Atlantic Water. This Atlantification of what was previously an Arctic environment has had profound implications for the local ecosystem and has greatly depleted local sea ice production. Many parallels may be drawn between the fjord systems on the west of Svalbard and the situation in SE Greenland, with the two regions sharing similar geometries and oceanographic settings. In both regions, along-shelf wind is a primary driver of exchange. Svalbard fjords are also relatively easy to access, making these regions well placed for conducting innovative fjord research, the results of which can be used to inform the wider topic of high-latitude fjord circulation and exchange. A secondary objective of this thesis was to explore new methods for making oceanographic measurements in fjords. In the first study of its kind, an underwater glider was deployed to Isfjorden in Svalbard, measuring the temperature, salinity and depth-averaged currents. The instrument provided velocity data with greater spatial coverage than was previously available, and was hence able to improve our understanding of the circulation patterns within the fjord. This, together with the hydrography data, was used to calculate heat advection, and provided a richer picture of how the circulation within a broad fjord can distribute heat throughout the interior.

6.2 Outcomes

Here, each of the main aims outlined in Chapter 1 is reiterated, followed by a summary of how they were addressed in this thesis:

- *Quantify the potential for fjord-shelf heat exchange in winter.*

Output from the model of KF indicates that the mean heat flux through the mid-fjord is of the order of 0.01 TW during the winter months. This is an order of magnitude smaller than previous estimates based on summertime observations. However, the modelled heat flux was highly variable, regularly exceeding the observed summertime values from the mid-fjord and reaching 0.5 TW near the head of the fjord. This provides the potential for significant wintertime heat flux events which, via discrete periods of enhanced melting, could trigger instabilities in glacier flow. The observed values are based on synoptic sections

that are not necessarily representative of the mean, and their scarcity introduces a large uncertainty into the mean summer value. Regardless, the results suggest that freshwater runoff is not necessary for up-fjord heat flux values to become significant. In Isfjorden, the glider section across the fjord entrance was used to calculate a heat flux value of 0.13 TW into the fjord during November 2014. While the section was a snapshot and lacked full depth coverage, leading to uncertainties, the value is useful as an order-of-magnitude estimate as there are no previous estimates in the published literature.

Along-shelf wind stress was found to be the dominant control on heat flux variability. In SE Greenland, the strong barrier winds which occur regularly throughout the winter were found to greatly enhance exchange between fjord and shelf. However, this did not necessarily correspond to increased heat delivery. While typical wind events lasted around 2-3 days, only prolonged events were found to be effective at driving warm water towards the GrIS. In accordance with previous results from Svalbard, this class of wind activity was found to strengthen the coastward barotropic transport of warm water in cross-shelf canyons. Long-duration wind events were also found to precede low-frequency intermediary circulation which was able to draw waters in the warm layer further into the fjord during each cycle. Over the course of the survey in Isfjorden, the prevailing on-shelf wind direction transitioned from northerly to southerly, establishing a geostrophic control mechanism at the fjord mouth and restricting exchange.

- *Assess the impact of the Earth's rotation on exchange in broad fjords.*

Previously, the extent to which the Earth's rotation influences the circulation in KF was unclear. While one summertime synoptic section showed cross-fjord current variability, other studies have argued that the local internal Rossby radius slightly exceeds the fjord width, rendering cross-fjord variability unimportant. The modelling studies presented in this thesis indicate that the Earth's rotation plays a critical role in the mean circulation within KF. The geostrophically balanced mean flow is characterised by inflow on the right-hand-side looking into the fjord, and outflow on the left, with the mean current speeds decreasing moving from the mouth to the head of the fjord. Due to cross-fjord gradients in the mean temperature field, this mean flow pattern acts to deliver heat towards the glacier terminus. In Isfjorden, which is over twice as broad as the local internal Rossby radius, synoptic glider sections indicate that the circulation was found to vary across the fjord similarly to KF. While this result is as expected based on theory, there were previously no published velocity measurements of the fjord interior. This allowed the exchange flows through the mid-fjord and fjord mouth to be quantified and, through the repeated glider section of the mid-fjord, provided information about the temporal variability. In the upper reaches of the Isfjorden system, this pattern of cross-fjord variability was not observed. It is not known whether this was due other physical processes becoming significant in this

region, error in the glider current measurements there, or the synoptic sections failing to represent the mean flow.

Rotation profoundly affected the nature of intermediary circulation in KF, which has previously been considered as a two-dimensional overturning process. Instead, information of the height of the pycnocline on the shelf propagated up-fjord as a CTW confined against the right-hand wall of the fjord. This interpretation of intermediary circulation is consistent with a previous observation of the cross-fjord velocity field, and has several implications for exchange. Under this regime the internal waves may be subinertial and, due to the asymmetry between the incoming and outgoing wave, do not have resonant period bands like the analogous seiching motions in narrow fjords. Furthermore, CTWs act to accelerate the flow on the right-hand-side of the fjord in the direction of wave propagation, likely due to via Stokes' drift, which enhanced the mean flow. There was no strong evidence for CTW activity in Isfjorden, where the flow was largely barotropic-dominated, however spatio-temporally dynamic platforms such as gliders are inappropriate for measuring this type of wave activity. Given the width of Isfjorden, and the prevalence of CTWs as a mechanism for exchange in the neighbouring Kongsfjorden, they are likely to be a feature of the dynamics there.

- *Investigate new means of observation in major fjord systems.*

The deployment of two Slocum gliders to Isfjorden marked the first time gliders have been used to study a fjord environment. The instrument gathered hydrographic and depth-averaged current data from throughout the region, which were combined to describe the absolute velocity field with a higher spatial resolution than was previously available. The survey also provided an estimate of the heat flux between the shelf and fjord entrance based on a synoptic section of the fjord mouth, and provided a rich picture of the circulation and exchange patterns in Isfjorden. As the first survey of its kind, some issues did arise. The choice of a 200 m rated glider meant coverage was limited in places where the region of study was deeper than the maximum depth rating. Coverage was also limited at some of the section ends, as the steep topographic boundaries inside fjords prompted the glider pilot allow a large margin for error. The strong, along-fjord winds, typical of the region, meant that some uncertainty was also introduced by drift while the glider was on the surface. These problems could all be significantly reduced or eliminated through planning and practice, and should be used to inform any similar projects in the future. The experiment was successful in showing that gliders can be navigated within a fjord and yield meaningful results.

6.3 Greenland-Svalbard Comparison

We here give a final comparison between the oceanographic behaviour of two regions studied in this thesis. In particular, it is worth revisiting the regimes which describe wintertime fjord-shelf interaction in SE Greenland and West Spitsbergen respectively.

In West Spitsbergen, positive (with coast to the right) shelf winds are found to restrict deep-layer exchange as downwelling strengthens and deepens the SPC. When the wind becomes negative, upwelling drives shoreward velocity in the deep-layer and hence brings warm water into the fjord. The situation in SE Greenland is similar, with barrier wind events occurring, over a timescale of around 2-3 days, during the winter. It is when the wind weakens, becoming less positive, that we see shoreward velocities in the warm layer below the pycnocline. The descriptions do differ in that positive shelf wind stress is, in SE Greenland, assumed to drive up-fjord velocities in the upper layer while, in West Spitsbergen, positive wind stress is associated with strengthening of barotropic coastal currents which flow across the fjord mouth, blocking exchange. A crucial parameter for differentiating between these two environments is the ratio of the sill depth to the mean height of the pycnocline. The fjord systems in West Spitsbergen are relatively shallow, so that barotropic coastal currents may follow coastal contours and isolate fjord from shelf. In SE Greenland, major fjords such as KF and SF are far deeper than the adjacent shelf region, so that a coastal current following depth contours will not by steered across the entrance and instead be directed into the fjord.

This contrast in underwater topography between KF compared to Isfjorden appears to affect the internal circulation structure. KF is deep and steep-sided along it's entire length, so that geostrophically balanced currents were unimpeded and able to influence the upper reaches of the fjord, close to the glacier terminus. Isfjorden is shallower than KF and becomes shallower still moving in-fjord. The geostrophically balanced currents here hence appeared highly sensitive to the changing bottom topography and hence had a limited influence on the shallower up-fjord regions. The circulation in Isfjorden hence had a larger ageostrophic component than that in KF.

6.4 Future Work

The most prominent obstacle to progress in Greenlandic fjord research is the lack of observations. While repeated measurements (using either autonomous platforms or traditional means) may not offer a new frontier for research, they are required in order to constrain heat and transport budgets, understand temporal variability over a wide spectrum of timescales (inertial to interannual), and to better initialise and validate hydrodynamic models.

The Isfjorden mission was successful in demonstrating that gliders (and other autonomous underwater platforms) can play a role in fjord observations in the future. Broad, largely ice-free fjords such as Isfjorden present only a first step. As glider technology and piloting grows more sophisticated, it may be able to alleviate some of the risks involved in gathering crucial data from regions such as SE Greenland, where ship-based wintertime observations are impracticable due to winter ice cover and icebergs. Navigation in narrower fjords may prove problematic, especially when maneuvering to take cross-fjord sections. However, in fjords narrower than the internal Rossby radius, the lack of cross-fjord variability means the along-fjord glider sections should be sufficient to capture the dominant features.

In Svalbard fjords, hydrographic stations are regularly occupied with good spatial and temporal coverage. Numerical modelling studies have been used in Kongsfjorden and, although runoff was confined to the surface, found that the balance between freshwater-driven and shelf-driven dynamics changes moving along the fjord. The modelling approach used in this thesis could be used to study Isfjorden and other Svalbard fjords, incorporating the parametrisation of subsurface discharge and melting. As well as shedding further light on the dynamical processes in Svalbard fjords, the relative abundance of data would make runs such as these a good opportunity to tune model parameters which could be widely adopted in an effort to standardise fjord modelling techniques. In particular, this could inform more accurate models of Greenlandic fjords. The next generation of models should aim for multi-year simulations including aspects such as tides, which were omitted in the simplified approach adopted here. This would lead to a more complete description of the hydrodynamics, however obstacles remain in accurately quantifying the oceanic contribution to glacial dynamics. Coupled ice-ocean models, able to capture calving and ocean-triggered instabilities in ice flow, are required in order to accurately simulate the observed shrinking of the GrIS.

Bibliography

Adcroft, A. J., Hill, C., Campin, J., Marshall, J., and Heimbach, P. (2004). Overview of the Formulation and Numerics of the MIT GCM. In *Proceedings of the ECMWF seminar series on Numerical Methods Recent developments in numerical methods for atmosphere and ocean modelling*, pages 139–149.

Allen, G. L. and Simpson, J. H. (2002). The Response of a Strongly Stratified Fjord to Energetic Tidal Forcing. *Estuarine, Coastal and Shelf Science*, 55(4):629–644.

Allen, J. S. (1975). Coastal trapped waves in a stratified ocean. *Journal of Physical Oceanography*, pages 300–325.

Andresen, C. S., Straneo, F., Ribergaard, M. H., Bjørk, A. A., Andersen, T. J., Kuijpers, A., Nørgaard-Pedersen, N., Kjær, K. H., Schjøth, F., Weckström, K., and Ahlstrøm, A. P. (2011). Rapid response of Helheim Glacier in Greenland to climate variability over the past century. *Nature Geoscience*, 5(1):37–41.

Arneborg, L., Erlandsson, C. P., Liljebladh, B., and Stigebrandt, A. (2004). The rate of inflow and mixing during deepwater renewal in a sill fjord. *Limnol. Oceanogr*, 49(3):768777.

Azetsu-Scott, K. and Tan, F. C. (1997). Oxygen isotope studies from Iceland to an East Greenland Fjord: Behaviour of glacial meltwater plume. *Marine Chemistry*, 56(3-4):239–251.

Bachmayer, R., Young, B. D., and Holland, D. (2007). Working Towards Ice Profiling Using Underwater Gliders: Operational Experience In Western Greenland. *Symposium on Unmanned Untethered Submersible Technology*.

Bacon, S. (2002). A freshwater jet on the east Greenland shelf. *Journal of Geophysical Research*, 107:3068.

Bacon, S., Marshall, A., Holliday, N. P., Aksenov, Y., and Dye, S. R. (2014). Seasonal variability of the East Greenland Coastal Current. *Journal of Geophysical Research: Oceans*, 119:1–18.

Bamber, J., Van Den Broeke, M., Ettema, J., Lenaerts, J., and Rignot, E. (2012). Recent large increases in freshwater fluxes from Greenland into the North Atlantic. *Geophysical Research Letters*, 39(19).

Barnes, S. L. (1994). Applications of the Barnes Objective Analysis Scheme. Part II: Improving Derivative Estimates. *Journal of Atmospheric and Oceanic Technology*, 11(6):1449–1458.

Berge, J., Heggland, K., Lønne, O. J., Cottier, F., Hop, H., Gabrielsen, G. W., Nøttestad, L., and Misund, O. A. (2015). First records of Atlantic mackerel (Scomber scombrus) from the Svalvard Archipelago, Norway, with possible explanations for the extension of its distribution. *Arctic*, 68(1):54–61.

Bevan, S. L., Luckman, A. J., and Murray, T. (2012). Glacier dynamics over the last quarter of a century at Helheim, Kangerdlugssuaq and 14 other major Greenland outlet glaciers. *Cryosphere*, 6(5):923–937.

Burton, J. C., Amundson, J. M., Abbot, D. S., Boghosian, A., Cathles, L. M., Correa-Legisos, S., Darnell, K. N., Guttenberg, N., Holland, D. M., and MacAyeal, D. R. (2012). Laboratory investigations of iceberg capsize dynamics, energy dissipation and tsunamigenesis. *Journal of Geophysical Research: Earth Surface*, 117(1):1–13.

Carroll, D., Sutherland, D. A., Hudson, B., Moon, T., Catania, G. A., Shroyer, E. L., Nash, J. D., Bartholomaus, T. C., Felikson, D., Stearns, L. A., Noël, B. P. Y., and van den Broeke, M. R. (2016). The impact of glacier geometry on meltwater plume structure and submarine melt in Greenland fjords. *Geophysical Research Letters*, 43(18):9739–9748.

Carroll, D., Sutherland, D. A., Shroyer, E. L., Nash, J. D., Catania, G. A., and Stearns, L. A. (2017). Subglacial discharge-driven renewal of tidewater glacier fjords. *Journal of Geophysical Research: Oceans*, 122(8):6611–6629.

Cenedese, C. and Adduce, C. (2010). A New Parameterization for Entrainment in Overflows. *Journal of Physical Oceanography*, 40(8):1835–1850.

Christoffersen, P., Mugford, R. I., Heywood, K. J., Joughin, I., Dowdeswell, J. A., Syvitski, J. P. M., Luckman, A., and Benham, T. J. (2011). Warming of waters in an East Greenland fjord prior to glacier retreat: Mechanisms and connection to large-scale atmospheric conditions. *Cryosphere*, 5(3):701–714.

Cottier, F. R., Nilsen, F., Enall, M. E., Gerland, S., Tverberg, V., and Svendsen, H. (2007). Wintertime warming of an Arctic shelf in response to large-scale atmospheric circulation. *Geophysical Research Letters*, 34(10):1–5.

Cottier, F. R., Nilsen, F., Skogseth, R., Tverberg, V., Skardhamar, J., and Svendsen, H. (2010). Arctic fjords: a review of the oceanographic environment and dominant physical processes. *Geological Society, London, Special Publications*, 344(1):35–50.

Cottier, F. R., Tverberg, V., Inall, M. E., Svendsen, H., Nilsen, F., and Griffiths, C. (2005). Water mass modification in an Arctic fjord through cross-shelf exchange: The seasonal hydrography of Kongsfjorden, Svalbard. *Journal of Geophysical Research: Oceans*, 110(12):1–18.

Cowton, T., Slater, D., Sole, A., Goldberg, D., and Nienow, P. (2015). Modeling the impact of glacial runoff on fjord circulation and submarine melt rate using a new subgrid-scale parameterization for glacial plumes. *Journal of Geophysical Research : Oceans*, 120(2):796–812.

Cowton, T., Sole, A., Nienow, P., Slater, D., Wilton, D., and Hanna, E. (2016). Controls on the transport of oceanic heat to Kangerdlugssuaq Glacier, East Greenland. *Journal of Glaciology*, 62(236):1167–1180.

Das, S. B., Joughin, I., Behn, M. D., Howat, I. M., King, M. A., Lizarralde, D., and Bhatia, M. P. (2008). Fracture Propagation to the Base of the Greenland Ice Sheet During Supraglacial Lake Drainage. *Science*, 320(5877):778–781.

Dee, D. P., Uppala, S. M., Simmons, A. J., Berrisford, P., Poli, P., Kobayashi, S., Andrae, U., Balmaseda, M. A., Balsamo, G., Bauer, P., Bechtold, P., Beljaars, A. C. M., van de Berg, L., Bidlot, J., Bormann, N., Delsol, C., Dragani, R., Fuentes, M., Geer, A. J., Haimberger, L., Healy, S. B., Hersbach, H., Hølm, E. V., Isaksen, L., Køllberg, P., Køhler, M., Matricardi, M., Mcnally, A. P., Monge-Sanz, B. M., Morcrette, J. J., Park, B. K., Peubey, C., de Rosnay, P., Tavolato, C., Thepaut, J. N., and Vitart, F. (2011). The ERA-Interim reanalysis: Configuration and performance of the data assimilation system. *Quarterly Journal of the Royal Meteorological Society*, 137(656):553–597.

Dowdeswell, J. A. (2004). Cruise Report - JR106b. RRS James Clark Ross. NERC Autosub Under Ice thematic programme, Kandgerdlugssuaq Fjord and Shelf, east Greenland. (September).

Enderlin, E. M. and Hamilton, G. S. (2014). Estimates of iceberg submarine melting from high-resolution digital elevation models: Application to Sermilik Fjord, East Greenland. *Journal of Glaciology*, 60(224):1111–1116.

Enderlin, E. M., Hamilton, G. S., Straneo, F., and Sutherland, D. A. (2016). Iceberg meltwater fluxes dominate the freshwater budget in Greenland's iceberg-congested glacial fjords. *Geophysical Research Letters*, 43(21):11,287–11,294.

Enderlin, E. M., Howat, I. M., Jeong, S., Noh, M.-J., van Angelen, J. H., and van den Broeke, M. R. (2014). An improved mass budget for the Greenland ice sheet. *Geophysical Research Letters*, 41(3):866–872.

Førland, E. J., Benestad, R., Hanssen-Bauer, I., Haugen, J. E., and Skaugen, T. E. (2011). Temperature and Precipitation Development at Svalbard 1900-2100. *Advances in Meteorology*, 2011:1–14.

Garau, B., Ruiz, S., Zhang, W. G., Pascual, A., Heslop, E., Kerfoot, J., and Tintoré, J. (2011). Thermal lag correction on slocum CTD glider data. *Journal of Atmospheric and Oceanic Technology*, 28(9):1065–1071.

Gelderloos, R., Haine, T. W. N., Koszalka, I. M., and Magaldi, M. G. (2017). Seasonal Variability in Warm-Water Inflow toward Kangerdlugssuaq Fjord. *Journal of Physical Oceanography*, 47(7):1685–1699.

Griffies, S. M. and Hallberg, R. W. (2000). Biharmonic Friction with a Smagorinsky-Like Viscosity for Use in Large-Scale Eddy-Permitting Ocean Models. *Monthly Weather Review*, 128(8):2935–2946.

Hanna, E., Cappelen, J., Fettweis, X., Huybrechts, P., Luckman, A., and Ribergaard, M. H. (2009). Hydrologic response of the Greenland ice sheet: The role of oceanographic warming. *Hydrological Processes*, 23(1):7–30.

Harden, B. E., Renfrew, I. A., and Petersen, G. N. (2011). A Climatology of wintertime barrier winds off southeast Greenland. *Journal of Climate*, 24(17):4701–4717.

Harden, B. E., Straneo, F., and Sutherland, D. A. (2014). Moored observations of synoptic and seasonal variability in the East Greenland Coastal Current. *Journal of Geophysical Research C: Oceans*, 119(12):8838–8857.

Holland, D. M., Thomas, R. H., de Young, B., Ribergaard, M. H., and Lyberth, B. (2008). Acceleration of Jakobshavn IsbræÂ triggered by warm subsurface ocean waters. *Nature Geoscience*, 1(10):659–664.

Howat, I. M., Joughin, I., and Scambos, T. A. (2007). Rapid Changes in Ice Discharge from Greenland Outlet Glaciers. *Science*, 315(5818):1559–1561.

Inall, M. E. and Gillibrand, P. A. (2010). The physics of mid-latitude fjords: a review. *Geological Society, London, Special Publications*, 344(1):17–33.

Inall, M. E., Murray, T., Cottier, F. R., Scharrer, K., Boyd, T., and Heywood, K. J. (2014). Oceanic heat delivery to the south-east Greenland ice sheet. *Journal of Geophysical Research*.

Inall, M. E., Nilsen, F., Cottier, F. R., and Daae, R. (2015). Shelf/fjord exchange driven by coastal-trapped waves in the Arctic. *Journal of Geophysical Research: Oceans*, 120(12):8283–8303.

Ingvaldsen, R., Reitan, M. B., Svendsen, H., and Asplin, L. (2001). The upper layer circulation of Kongsfjorden and Krossfjorden - a complex fjord system on the west coast of spitsbergen. *Memoirs of National Institute of Polar Research*, (Special Issue, 54):393–407.

Jackson, R. H., Straneo, F., and Sutherland, D. A. (2014). Externally forced fluctuations in ocean temperature at Greenland glaciers in non-summer months. *Nature Geoscience*, 7(June):1–6.

Janzen, C. D., Simpson, J. H., Inall, M. E., and Cottier, F. (2005). Across-sill circulation near a tidal mixing front in a broad fjord. *Continental Shelf Research*, 25(15):1805–1824.

Jenkins, A. (2011). Convection-driven melting near the grounding lines of ice shelves and tidewater glaciers. *Journal of Physical Oceanography*, 41(12):2279–2294.

Johnson, H. L., Münchow, A., Falkner, K. K., and Melling, H. (2011). Ocean circulation and properties in Petermann Fjord, Greenland. *Journal of Geophysical Research: Oceans*, 116(1).

Joughin, I., Howat, I. M., Fahnestock, M., Smith, B., Krabill, W., Alley, R. B., Stern, H., and Truffer, M. (2008). Continued evolution of Jakobshavn Isbrae following its rapid speedup. *Journal of Geophysical Research: Earth Surface*, 113(4):F04006.

Khan, S. A., Kjeldsen, K. K., Kjær, K. H., Bevan, S. L., Luckman, A., Bjørk, A. A., Korsgaard, N. J., Box, J. E., van den Broeke, M. R., van Dam, T. M., and Fitzner, A. (2014). Glacier dynamics at Helheim and Kangerdlugssuaq glaciers, southeast Greenland, since the Little Ice Age. *Cryosphere*, 8(4):1497–1507.

Klinck, J. M., O'Brien, J. J., and Svendsen, H. (1981). A Simple Model of Fjord and Coastal Circulation Interaction. *Journal of Physical Oceanography*, 11(12):1612–1626.

Knudsen, M. (1900). Ein hydrographischer Lehrsatz. *Mar. Meteorol.*, 28:316–320.

Koszalka, I. M., Haine, T. W. N., and Magaldi, M. G. (2013). Fates and Travel Times of Denmark Strait Overflow Water in the Irminger Basin. *Journal of Physical Oceanography*, 43(12):2611–2628.

Large, W. G., McWilliams, J. C., and Doney, S. C. (1994). Oceanic vertical mixing: A review and a model with a nonlocal boundary layer parameterization.

Large, W. G. and Pond, S. (1981). Open Ocean Momentum Flux Measurements in Moderate to Strong Winds. *Journal of Physical Oceanography*, 11(3):324–336.

Lee, C. M. and Thompson, J. (2017). An autonomous approach to observing the seasonal ice zone in the western Arctic. *Oceanography*, pages 56–68.

Leith, C. E. (1996). Stochastic models of chaotic systems. *Physica D: Nonlinear Phenomena*, 98:481–491.

Luckman, A., Benn, D. I., Cottier, F., Bevan, S., Nilsen, F., and Inall, M. (2015). Calving rates at tidewater glaciers vary strongly with ocean temperature. *Nature Communications*, 6(October):8566.

MacCready, P. and Geyer, W. R. (2010). Advances in Estuarine Physics. *Annual Review of Marine Science*, 2(1):35–58.

Magaldi, M. G. and Haine, T. W. N. (2015). Hydrostatic and non-hydrostatic simulations of dense waters cascading off a shelf: The East Greenland case. *Deep-Sea Research Part I: Oceanographic Research Papers*, 96:89–104.

Magaldi, M. G., Haine, T. W. N., and Pickart, R. S. (2011). On the Nature and Variability of the East Greenland Spill Jet: A Case Study in Summer 2003*. *Journal of Physical Oceanography*, 41(12):2307–2327.

Marshall, J., Adcroft, A., Hill, C., Perelman, L., and Heisey, C. (1997). A finite-volume, incompressible Navier Stokes model for studies of the ocean on parallel computers. *Journal of Geophysical Research: Oceans*, 102(C3):5753–5766.

Martin, T., Steele, M., and Zhang, J. (2014). Seasonality and long-term trend of Arctic Ocean surface stress in a model. *Journal of Geophysical Research : Oceans*, (1):1723–1738.

McDougall, Trevor J. ; Barker, P. (2011). Getting started with TEOS-10 and the Gibbs Seawater (GSW) Oceanographic Toolbox. *Scor/Iapso Wg127*, page 28.

Merckelbach, L. M., Briggs, R. D., Smeed, D. A., and Griffiths, G. (2008). Current measurements from autonomous underwater gliders. In *Proceedings of the IEEE Working Conference on Current Measurement Technology*, pages 61–67.

Moon, T., Sutherland, D. A., Carroll, D., Felikson, D., Kehrl, L., and Straneo, F. (2017). Subsurface iceberg melt key to Greenland fjord freshwater budget. *Nature Geoscience*.

Morlighem, M., Williams, C. N., Rignot, E., An, L., Bamber, J. L., Catania, G., Dowdeswell, J. A., Dorschel, B., Fenty, I., Hogan, K., Howat, I., Hubbard, A., Jakobsson, M., Jordan, T. M., Kjeldsen, K. K., Millan, R., Mayer, L., Mouginot, J., Palmer, S., Rysgaard, S., Seroussi, H., Slabon, P., Straneo, F., Weinrebe, W., Wood, M., and Zinglersen, B. (2017). BedMachine v3: Complete bed topography and ocean bathymetry mapping of Greenland from multi-beam echo sounding combined with mass conservation.

Mortensen, J., Bendtsen, J., Motyka, R. J., Lennert, K., Truffer, M., Fahnestock, M., and Rysgaard, S. (2013). On the seasonal freshwater stratification in the proximity of fast-flowing tidewater outlet glaciers in a sub-Arctic sill fjord. *Journal of Geophysical Research: Oceans*, 118(3):1382–1395.

Mortensen, J., Lennert, K., Bendtsen, J., and Rysgaard, S. (2011). Heat sources for glacial melt in a sub-Arctic fjord (Godthåbsfjord) in contact with the Greenland Ice Sheet. *Journal of Geophysical Research: Oceans*, 116(1):1–13.

Motyka, R. J., Dryer, W. P., Amundson, J., Truffer, M., and Fahnestock, M. (2013). Rapid submarine melting driven by subglacial discharge, LeConte Glacier, Alaska. *Geophysical Research Letters*, 40(19):5153–5158.

Motyka, R. J., Hunter, L., Echelmeyer, K. A., and Connor, C. (2003). Submarine melting at the terminus of a temperate tidewater glacier, LeConte Glacier, Alaska, U.S.A. *Annals of Glaciology*, 36:57–65.

Muckenhuber, S., Nilsen, F., Korosov, A., and Sandven, S. (2016). Sea ice cover in Isfjorden and Hornsund, Svalbard (2000 - 2014) from remote sensing data. *The Cryosphere*, 10(1):149–158.

Murray, T., Scharrer, K., James, T. D., Dye, S. R., Hanna, E., Booth, A. D., Selmes, N., Luckman, A., Hughes, A. L. C., Cook, S., and Huybrechts, P. (2010). Ocean regulation hypothesis for glacier dynamics in southeast Greenland and implications for ice sheet mass changes. *Journal of Geophysical Research: Earth Surface*, 115(3).

Nick, F. M., Vieli, A., Howat, I. M., and Joughin, I. (2009). Large-scale changes in Greenland outlet glacier dynamics triggered at the terminus. *Nature Geoscience*, 2(2):110–114.

Nilsen, F., Cottier, F. R., Skogseth, R., and Mattsson, S. (2008). Fjord-shelf exchanges controlled by ice and brine production: The interannual variation of Atlantic Water in Isfjorden, Svalbard. *Continental Shelf Research*, 28(14):1838–1853.

Nilsen, F., Skogseth, R., Vaardal-Lunde, J., and Inall, M. E. (2016). A Simple Shelf Circulation Model: Intrusion of Atlantic Water on the West Spitsbergen Shelf. *Journal of Physical Oceanography*, 46(4):1209–1230.

Nuth, C., Kohler, J., König, M., Von Deschwanden, A., Hagen, J. O., Kääb, A., Moholdt, G., and Pettersson, R. (2013). Decadal changes from a multi-temporal glacier inventory of Svalbard. *Cryosphere*, 7(5):1603–1621.

Nuth, C., Moholdt, G., Kohler, J., Hagen, J. O., and Kääb, A. (2010). Svalbard glacier elevation changes and contribution to sea level rise. *Journal of Geophysical Research: Earth Surface*, 115(1).

O'Leary, M. and Christoffersen, P. (2013). Calving on tidewater glaciers amplified by submarine frontal melting. *Cryosphere*, 7(1):119–128.

Onarheim, I. H., Smedsrud, L. H., Ingvaldsen, R., and Nilsen, F. (2014a). Loss of sea ice during winter north of Svalbard. *Tellus, Series A: Dynamic Meteorology and Oceanography*, 66(1):1–9.

Onarheim, I. H., Smedsrud, L. H., Ingvaldsen, R. B., and Nilsen, F. (2014b). Loss of sea ice during winter north of Svalbard. *Tellus, Series A: Dynamic Meteorology and Oceanography*, 66(1):1–9.

Padman, L. (2004). A barotropic inverse tidal model for the Arctic Ocean. *Geophysical Research Letters*, 31(2):2–5.

Parsmar, R. and Stigebrandt, A. (1997). Observed Damping of Barotropic Seiches through Baroclinic Wave Drag in the Gullmar Fjord. *Journal of Physical Oceanography*, 27(6):849–857.

Pavlov, A. K., Tverberg, V., Ivanov, B. V., Nilsen, F., Falk-Petersen, S., and Granskog, M. A. (2013). Warming of Atlantic water in two west Spitsbergen fjords over the last century (1912-2009). *Polar Research*, 32.

Pawlowicz, R., Beardsley, B., and Lentz, S. (2002). Classical tidal harmonic analysis including werror estimates in MATLAB using T-TIDE. *Computers and Geosciences*, 28(8):929–937.

Rabinovich, A. B., Shevchenko, G. W., and Thomson, R. E. (2007). Sea ice and current response to the wind: A vector regressional analysis approach. *Journal of Atmospheric and Oceanic Technology*, 24(6):1086–1101.

Rignot, E. and Kanagaratnam, P. (2006). Changes in the Velocity Structure of the Greenland Ice Sheet. *Science*, 311(February):986–990.

Rignot, E., Koppes, M., and Velicogna, I. (2010). Rapid submarine melting of the calving faces of West Greenland glaciers. *Nature Geoscience*, 3(3):187–191.

Salcedo-Castro, J., Bourgault, D., and DeYoung, B. (2011). Circulation induced by subglacial discharge in glacial fjords: Results from idealized numerical simulations. *Continental Shelf Research*, 31(13):1396–1406.

Schellenberger, T., Dunse, T., Kääb, A., Kohler, J., and Reijmer, C. H. (2015). Surface speed and frontal ablation of Kronebreen and Kongsbreen, NW Svalbard, from SAR offset tracking. *Cryosphere*, 9(6):2339–2355.

Schofield, O., Kohut, J., Aragon, D., Creed, L., Graver, J., Haldeman, C., Kerfoot, J., Roarty, H., Jones, C., Webb, D., and Glenn, S. (2007). Slocum Gliders: Robust and ready. *Journal of Field Robotics*, 24(6):473–485.

Sciascia, R., Straneo, F., Cenedese, C., and Heimbach, P. (2013). Seasonal variability of submarine melt rate and circulation on an East Greenland fjord. *Journal of Geophysical Research*, 118:1–49.

Seale, A., Christoffersen, P., Mugford, R. I., and O'Leary, M. (2011). Ocean forcing of the Greenland Ice Sheet: Calving fronts and patterns of retreat identified by automatic satellite monitoring of eastern outlet glaciers. *Journal of Geophysical Research: Earth Surface*, 116(3):F03013.

Seity, Y., Brousseau, P., Malardel, S., Hello, G., Bénard, P., Bouttier, F., Lac, C., and Masson, V. (2011). The AROME-France convective-scale operational model. *Monthly Weather Review*, 139(3):976–991.

Shepherd, A., Ivins, E. R., A, G., Barletta, V. R., Bentley, M. J., Bettadpur, S., Briggs, K. H., Bromwich, D. H., Forsberg, R., Galin, N., Horwath, M., Jacobs, S., Joughin, I., King, M. A., Lenaerts, J. T. M., Li, J., Ligtenberg, S. R. M., Luckman, A., Luthcke, S. B., McMillan, M., Meister, R., Milne, G., Mouginot, J., Muir, A., Nicolas, J. P., Paden, J., Payne, A. J., Pritchard, H., Rignot, E., Rott, H., Sorensen, L. S., Scambos, T. A., Scheuchl, B., Schrama, E. J. O., Smith, B., Sundal, A. V., van Angelen, J. H., van de Berg, W. J., van den Broeke, M. R., Vaughan, D. G., Velicogna, I., Wahr, J., Whitehouse, P. L., Wingham, D. J., Yi, D., Young, D., and Zwally, H. J. (2012). A Reconciled Estimate of Ice-Sheet Mass Balance. *Science*, 338(6111):1183–1189.

Skogseth, R., Haugan, P. M., and Haarpaintner, J. (2004). Ice and brine production in Storfjorden from four winters of satellite and in situ observations and modeling. *Journal of Geophysical Research C: Oceans*, 109(10).

Skogseth, R., Haugan, P. M., and Jakobsson, M. (2005). Watermass transformations in Storfjorden. *Continental Shelf Research*, 25(5-6):667–695.

Skogseth, R., Sandvik, A. D., and Asplin, L. (2007). Wind and tidal forcing on the mesoscale circulation in Storfjorden, Svalbard. *Continental Shelf Research*, 27(2):208–227.

Sole, A., Payne, A. J., Nienow, P., Christoffersen, P., Cottier, F. R., and Inall, M. E. (2012). Increased glacier runoff enhances the penetration of warm Atlantic water into a large Greenland fjord. *The Cryosphere Discussions*, 6(6):4861–4896.

Spall, M. A., Jackson, R. H., and Straneo, F. (2017). Katabatic Wind-Driven Exchange in Fjords.

Steele, M., Morley, R., and Ermold, W. (2001). PHC: A global ocean hydrography with a high-quality Arctic Ocean. *Journal of Climate*, 14(9):2079–2087.

Stokes, G. G. (1847). On the theory of oscillatory waves. *Transactions of the Cambridge Philosophical Society*, (8):441–455.

Stommel, H. (1989). The slocum mission. *Oceanography*, 2(1):22–25.

Stommel, H. and Farmer, H. G. (1953). Control of salinity in an estuary by a transition. *Journal of Marine Research*, 13:13–20.

Støylen, E. and Weber, J. E. H. (2010). Mass transport induced by internal Kelvin waves beneath shore-fast ice. *Journal of Geophysical Research*, 115(C3):C03022.

Straneo, F., Curry, R. G., Sutherland, D. A., Hamilton, G. S., Cenedese, C., Våge, K., and Stearns, L. A. (2011). Impact of fjord dynamics and glacial runoff on the circulation near Helheim Glacier. *Nature Geoscience*, 4(5):322–327.

Straneo, F., Hamilton, G. S., Sutherland, D. A., Stearns, L. A., Davidson, F., Hammill, M. O., Stenson, G. B., and Rosing-Asvid, A. (2010). Rapid circulation of warm subtropical waters in a major glacial fjord in East Greenland. *Nature Geoscience*, 3(3):182–186.

Straneo, F. and Heimbach, P. (2013). North Atlantic warming and the retreat of Greenland's outlet glaciers. *Nature*, 504(7478):36–43.

Sundfjord, A., Albretsen, J., Kasajimi, Y., Skogseth, R., Kohler, J., Nuth, C., Skardhamar, J., Cottier, F., Nilsen, F., Asplin, L., Gerland, S., and Torsvik, T. (2017). Effects of glacier runoff and wind on surface layer dynamics and Atlantic Water exchange in Kongsfjorden, Svalbard; a model study. *Estuarine, Coastal and Shelf Science*, 187:260–272.

Sutherland, D. A. and Pickart, R. S. (2008). The East Greenland Coastal Current: Structure, variability, and forcing. *Progress in Oceanography*, 78(1):58–77.

Sutherland, D. A., Roth, G. E., Hamilton, G., Mernild, S. H., Stearns, L. A., and Straneo, F. (2014a). Quantifying flow regimes in a Greenland glacial fjord using iceberg drifters. *Geophysical Research Letters*, 41(23):8411–8420.

Sutherland, D. A. and Straneo, F. (2012). Estimating ocean heat transports and submarine melt rates in sermilik fjord, greenland, using lowered acoustic doppler current profiler (LADCP) velocity profiles. *Annals of Glaciology*, 53(60):50–58.

Sutherland, D. A., Straneo, F., and Pickart, R. S. (2014b). Characteristics and dynamics of two major Greenland glacial fjords. *Journal of Geophysical Research: Oceans*, 119(6):3767–3791.

Svendsen, H., Beszczynska-Møller, A., Hagen, J. O., Lefauconnier, B., Tverberg, V., Gerland, S., Ørbæk, J. B., Bischof, K., Papucci, C., Zajaczkowski, M., Azzolini, R., Bruland, O., Wiencke, C., Winther, J., and Dallmann, W. (2002). The physical environment of Kongsfjorden-Krossfjorden, an Arctic fjord system in Svalbard. *Polar Research*, 21(1):133–166.

Taylor, G. I. (1917). Motion of solids in fluids when the flow is not irrotational. *Proceedings of the Royal Society A*, 93(648).

Torrence, C. and Compo, G. P. (1998). A Practical Guide to Wavelet Analysis. *Bulletin of the American Meteorological Society*, 79(1):61–78.

Treasure, A., Roquet, F., Ansorge, I., Bester, M., Boehme, L., Bornemann, H., Charrassin, J.-B., Chevallier, D., Costa, D., Fedak, M., Guinet, C., Hammill, M., Harcourt, R., Hindell, M., Kovacs, K., Lea, M.-A., Lovell, P., Lowther, A., Lydersen, C., McIntyre, T., McMahon, C., Muelbert, M., Nicholls, K., Picard, B., Reverdin, G., Trites, A., Williams, G., and de Bruyn, P. N. (2017). Marine Mammals Exploring the Oceans Pole to Pole: A Review of the MEOP Consortium. *Oceanography*, 30(2):132–138.

Tverberg, V., Nøst, O. A., Lydersen, C., and Kovacs, K. M. (2014). Winter sea ice melting in the Atlantic Water subduction area, Svalbard Norway. *Journal of Geophysical Research: Oceans*, 119(9):5945–5967.

Von der Mühll, K. (1886). Ueber die Bewegung tropfbarer Flüssigkeiten in Gefässen - Nach Johann Rudolf Merian. *Mathematische Annalen*, 27(4):575–600.

Wadhams, P. (2000). *Ice in the ocean*. CRC Press.

Weber, J. E. H. and Ghaffari, P. (2014). Mass transport in internal coastal Kelvin waves. *European Journal of Mechanics, B/Fluids*, 47:151–157.

Willis, K. J., Cottier, F. R., and Kwaśniewski, S. (2008). Impact of warm water advection on the winter zooplankton community in an Arctic fjord. *Polar Biology*, 31(4):475–481.

Wood and Stephen (2009). Autonomous Underwater Gliders. In *Underwater Vehicles*, pages 301–321. InTech.

Wunsch, C. (1973). On the mean drift in large lakes. *Limnology and Oceanography*, 18(5):793–794.

Xu, Y., Rignot, E., Menemenlis, D., and Koppes, M. (2012). Numerical experiments on subaqueous melting of greenland tidewater glaciers in response to ocean warming and enhanced subglacial discharge. *Annals of Glaciology*, 53(60):229–234.

Zhou, M., Bachmayer, R., and De Young, B. (2015). Working towards seafloor and underwater iceberg mapping with a Slocum glider. In *2014 IEEE/OES Autonomous Underwater Vehicles, AUV 2014*.